NTNU – Trondheim
Norwegian University of
Science and Technology

Experimental Study on the Hydrodynamic Forces acting on Objects in a Moonpool

Leiv Aspelund

Marine Technology
Submission date: June 2013
Supervisor: Bjørnar Pettersen, IMT
Co-supervisor: Tor-Bjørn Idsøe Næss, Subsea 7 Stavanger
Jan Visscher, Marintek

Norwegian University of Science and Technology
Department of Marine Technology

Master thesis

EXPERIMENTAL STUDY ON THE HYDRODYNAMIC FORCES ACTING ON OBJECTS IN A MOONPOOL

Leiv Aspelund

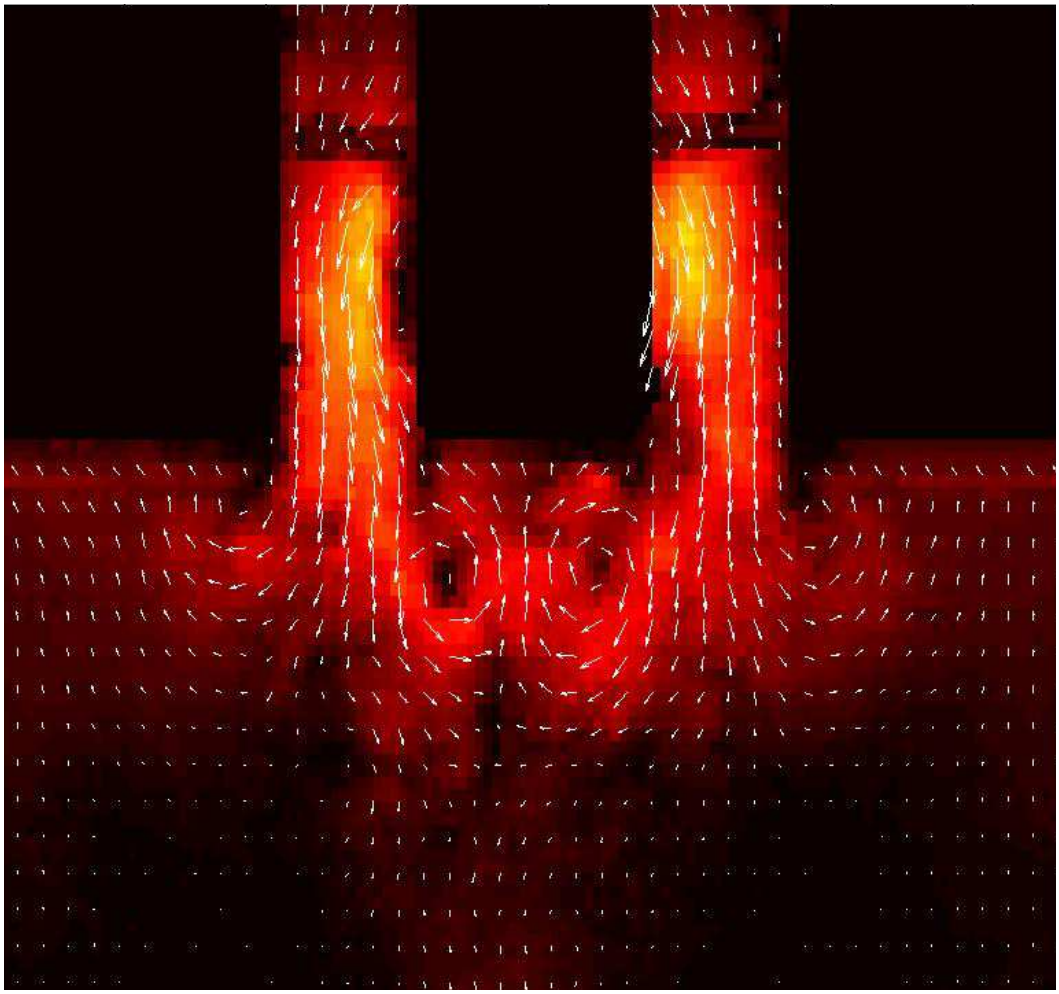

Advisors:
Bjørnar Pettersen, NTNU
Jan Visscher, MARINTEK
Tor-Bjørn Idsøe Næss, Subsea 7

2013
Norwegian University of Science and Technology (NTNU)
Department of Marine Technology

Picture on front page: Velocity field of fluid in and around the moonpool of *Seven Viking*, with a square object inside the moonpool

Abstract

This master thesis describes and discusses an experimental study on the hydrodynamic forces acting on objects in a moonpool, carried out at MARINTEK in 2013. The experiments were done using a simplified 2-dimensional moonpool model with two different configurations; one base case with a sharp inlet and no perforated walls inside the moonpool, and one configuration attempting to model the moonpool of the vessel *Seven Viking*, which has a rounded inlet and perforated walls. Both moonpools were tested without objects, while the *Seven Viking*-model was also tested with two objects inside the moonpool, both of the same geometry (square cross sections) but of different sizes.

In the past, a considerable amount of research has been devoted to the wave elevation in an empty moonpool, a problem which has proven difficult to describe with sufficient accuracy unless the most complicated numerical methods are applied. However, very little is known regarding the hydrodynamic forces acting on objects in moonpools. Simplified methods, recommended by DNV (Det Norske Veritas), for determining these forces exist (DNV 2011). These methods are based on the following assumptions:

- The presence of an object does not alter the fluid motions in the moonpool to a significant degree.
- The forces on the object can be determined using Morison's equation with correction factors based on the level of blockage, as for an object in a tube or channel.

The main motivation for carrying out the current model tests was to compare the measured forces with the forces predicted by such a simplified method, and thereby attempting to determine the validity of the method and its assumptions.

The experiments revealed that introducing objects in a moonpool changes the wave elevation dramatically, even for quite small objects. The overall wave elevation amplitude is strongly reduced and the resonance period is altered. Therefore it is no surprise that the simplified calculation methods fail to predict not only the magnitude of the hydrodynamic forces on the objects, but also the trends.

If, on the other hand, the true fluid motions (found from the experiments when the object is inside the moonpool) are used as the basis of the force calculations, the predicted forces turn out to be quite close to the measured forces. This shows that, at least in this particular case, the assumption about the validity of Morison's equation may be justified to some extent. This scheme is however not very useful in real life, as the fluid motions when an object is inside the moonpool are generally not known unless model tests have been performed beforehand, in which case the forces are likely to be measured directly anyway.

Throughout the current model tests, the technique of PIV, particle image velocimetry, has been used for visualizing the flow field inside and in the vicinity of the moonpools. The results have shown how the formation of vortices are considerably less triggered by the rounded inlet of the *Seven Viking*-moonpool compared to the base case with the sharp inlet. This is also reflected in the transfer functions of the wave elevation in the moonpools where it can be seen that the *Seven Viking-moonpool* has less non-linear damping than the base case. The PIV results also show that there seems to be only a small amount of flow through the perforated walls of the *Seven Viking*-moonpool.

Sammendrag (Norwegian translation of abstract)

Denne master-oppgaven beskriver og diskuterer en eksperimentell studie av de hydrodynamiske kreftene som virker på objekter i en moonpool. Eksperimentene ble gjort på MARINTEK i 2013. En forenklet 2-dimensjonal moonpool-modell med to forskjellige geometrier ble benyttet; en grunnmodell med skarpt hjørne i innløpet og uten perforerte sidevegger og en modell av moonpoolen til skipet *Seven Viking* som har avrundet innløp og perforerte vegger. Begge modellene ble testet uten objekter, mens *Seven Viking*-modellen ble testet også med to objekter i moonpoolen. Begge objektene hadde samme kvadratiske tverrsnitt men var av forskjellig størrelse.

Tidligere har mye forskning blitt gjort for å finne bølgehevningen i en tom moonpool, noe som har vist seg å være vanskelig å få til med tilstrekkelig grad av nøyaktighet med mindre de mest avanserte numeriske metodene benyttes. På den andre siden har krefter på objekter i en moonpool blitt studert lite. Det finnes forenklede metoder som anbefales av DNV, Det Norske Veritas, (DNV 2011) for å finne disse kreftene. Metodene er basert på følgende antagelser:

- Tilstedeværelsen av et objekt i moonpoolen forandrer ikke vannets bevegelses-karakteristikk i betydelig grad.
- Krefter på objektet kan finnes ved hjelp av Morison's ligning med korreksjonsfaktorer basert på objektets blokkeringsforhold, som for et objekt i et rør eller i en kanal.

Den viktigste grunnen for å utføre modelltestene var å sammenligne de målte kreftene i forsøkene med kreftene beregnet med en slik forenklet metode for å finne ut om metoden og antagelsene den er basert på er gyldig.

Eksperimentene viste tydelig at selv et relativt lite objekt i en moonpool dramatisk forandrer vannets bevegelseskarakteristikk. Den totale bølgehevningsamplituden blir kraftig redusert og resonansperioden endres. Derfor er det ikke overraskende at den forenklede beregningsmetoden ikke er i stand til å beregne hverken størrelsen på eller trendene til de hydrodynamiske kreftene.

Hvis derimot den faktiske væskebevegelsen (funnet i forsøkene med objekt i moonpoolen) brukes som basis for kraftberegningene blir de resulterende beregnede kreftene ganske like de målte kreftene. Dette indikerer at antagelsen om at Morison's ligning kan benyttes kan være gyldig, i hvert fall i dette spesifikke tilfellet. Derimot er ikke dette resultatet så nyttig i virkeligheten, for væskebevegelsene i en moonpool med et objekt er vanligvis ikke kjent på forhånd, med mindre modelltester har blitt gjort. Og i så fall vil man vanligvis ha målt kreftene direkte uansett.

PIV, particle image velocimetry, har blitt benyttet i forsøkene beskrevet i denne oppgaven for å visualisere strømningen i og rundt moonpoolen. De resulterende strømningsfeltene har vist at det dannes betydelig mindre virvler ved utløpet til *Seven Viking*-moonpoolen sammenlignet med grunnmodellen med de skarpe hjørnene. Dette reflekteres også i transfer-funksjonene for bølgehevingen, som viser at *Seven Viking* har lavere grad av ikke-lineær dempning. PIV-resultatene viser også at det er ganske lite fluidstrøm gjennom de perforerte veggene i moonpoolen.

Table of contents

Preface

This master thesis is the product of my work during my tenth and final semester at NTNU, The Norwegian University of Science and Technology, Department of Marine Technology, in the spring of 2013.

The overall topic of the thesis, hydrodynamics in moonpools, was selected during my internship in the Naval Discipline of Subsea 7 Stavanger in the summer of 2012. The topic was suggested by Tor-Bjørn Idsøe Næss because he believed it would be both academically challenging for me as well as being beneficial for Subsea 7.

After devoting a project thesis to a background and literature study of the topic in the fall of 2012, I got an overview of what would be interesting to study in greater detail. From the start I was very motivated to make use of the partnership between NTNU and MARINTEK and grab the opportunity to do model tests while I had the chance. I learned that a basic 2D moonpool model already existed which previously had been used by Trygve Kristiansen amongst others. After a lecture held by Jan Visscher about PIV ("particle image velocimetry") I conceived the idea of applying this technique on the moonpool model. Jan was very positive to this as it gave him a chance to test PIV on a new application, and so was Trygve because of his interest in the flow fields inside and in the vicinity of moonpools.

The final piece of the puzzle fell neatly into place when Statoil agreed to finance Tor-Bjørn Idsøe Næss and Subsea 7's proposed series of more comprehensive model tests on the moonpool of the Subsea 7-operated vessel *Seven Viking* (of Ulstein design), the main motivation of which was to study the effect and behaviour of objects inside the moonpool. These experiments were planned and carried out by Kjetil Berget at MARINTEK, who also saw the potential of comparing the results from his tests with the simpler 2-dimensional set-up I planned to use. Because of this, the majority of my experiments have been done with a configuration made to resemble the moonpool of *Seven Viking*. Statoil generously agreed to finance the necessary fabrications also for my experiments, and Ulstein kindly gave me permission to let me use their moonpool design.

Doing model tests at MARINTEK has been a good experience for me, in which I have gotten an insight into experimental hydrodynamics I probably never would have gotten otherwise. I think I will benefit greatly from this experience also later in my academic career, even though it is likely I will not be this directly involved in model testing again.

I am very pleased with the results I have obtained from the experiments and I consider my findings to shed – at least a flicker – of new light on the topic of my thesis. Additionally, I think the use of PIV revealed several interesting phenomena, despite the fact that probably only a fraction of the potential of the technique was put to use.

I have received a lot of help and feedback from many people during my work. First of all I would like to thank Professor Bjørnar Pettersen, my advisor at NTNU, for displaying a sincere interest in my education and for being helpful in arranging the model tests at MARINTEK.

At all stages of my work I have been impressed, and almost overwhelmed, at the level of support I have gotten from everybody I have been in contact with at MARINTEK. Jan Visscher has spent much of his time helping me with the PIV set-up and analyses. Alexander Sandnes also played an important role in setting up the PIV system. Torgeir Wahl and

especially Terje Rosten (who are both NTNU-employees) were immensely helpful in setting up the lab and arranging the instrumentation. Kjetil Berget has given me a lot of feedback on my results and good advice in the planning phase. He has also included me in and given me access to his parallel moonpool experiments. Trygve Kristiansen has been very supportive in all stages of my work and has been an important consultant.

Last but not least I wish to express my gratitude towards Tor-Bjørn Idsøe Næss and Petter Moen of the Naval Discipline of Subsea 7 Stavanger. They have both been unconditionally supportive of my work and have shown genuine concern for my learning outcome of the thesis. Tor-Bjørn has put a huge effort into the topic of moonpools himself and has therefore been a vital consultant for me, and finally he was also the main initiator of the aforementioned MARINTEK model tests carried out by Kjetil Berget.

Leiv Aspelund

Trondheim, June 7th 2013

Nomenclature

CFD	Computational fluid dynamics
DNV	Det Norske Veritas
NTNU	Norwegian University of Science and Technology
PIV	Particle image velocimetry
RAO	Response amplitude operator

1. Introduction

Subsea development is an area in the oil and gas industry which has seen a lot of growth over the last years. The number of subsea operations has increased and so has the complexity of the operations. Larger structures are being installed, and it is desirable to be able to work in more severe environmental conditions.

Most subsea operations involve deploying structures, umbilicals, diving bells or remotely operated vehicles (ROV's) from a vessel into the sea. This can be done by lifting the item in question over the ship side, but in many cases it is more beneficial to use a moonpool. A moonpool can be thought of as a bottomless well in the ship hull. Most subsea construction and installation vessels today are equipped with moonpool(s). Figure 2 shows a picture of the Subsea 7-operated vessel *Skandi Seven* with its main moonpool visible on deck.

Figure 2 - *Skandi Seven* with moonpool (DOF)

Moonpools are especially well suited for IMR (inspection, maintenance and repair) operations as these usually do not involve deployment of very large structures, but they are on the other hand often carried out for longer periods of time and in more severe sea states.

The generally assumed advantages of deployment through a moonpool include (DNV 2011):

- The horizontal fluid motions in the moonpool are small.
- The moonpool is often located close to the vessel's roll and pitch centre, and therefore the ship motions are smaller than at the side.
- Moonpools often have special deployment systems which may eliminate the need for lifting with a crane.
- In arctic conditions the moonpool offers some shelter for drifting ice.

Although the horizontal fluid motion in general is very small inside moonpools, the vertical fluid motion is another story. It may sound reasonable to assume that also the vertical motions are reduced compared to the motions at the ship side, but given the right (or wrong) circumstances it can actually be quite the opposite.

The vertical fluid motion inside a moonpool has proven hard to predict. Additionally, very little research on the vertical hydrodynamic forces acting on objects in a moonpool has been done. DNV, Det Norske Veritas, offers guidelines for the practical analysis of a wide range of marine operations including operations through moonpools (DNV 2011). The validity of some of the assumptions made for the moonpool analyses are however somewhat uncertain, as will be discussed and pointed out in this thesis.

Scope of experimental research for thesis

The main motivation for carrying out the experimental research described in this thesis was to shed new light on the problem of determining forces on objects inside a moonpool. The formal thesis description can be found in Appendix C.

The experiments were mainly meant for studying trends, i.e. to investigate how the variation of different parameters affected the resulting motions and forces. A simplified 2-dimensional moonpool set-up was studied. Two different moonpool geometries were used; one basic model with a sharp inlet and no perforated walls and one made to resemble the moonpool of the Subsea 7-operated vessel *Seven Viking*, which has a rounded inlet and perforated walls.

The basic moonpool was included primarily as a validation case for comparison with previous model tests done by Kristiansen et al. (Kristiansen et al. 2011). The *Seven Viking*-moonpool was chosen because more advanced 3-dimensional experiments were carried out simultaneously at MARINTEK on the same moonpool design, which resulted in a nice opportunity to compare the results from the 2D and 3D set-ups.

A flyer of the vessel *Seven Viking*, of Ulstein design, can be found in Appendix B. It is a new vessel completed in 2012, specifically designed for carrying out IMR operations in harsh conditions, in which the moonpool will be used extensively. Therefore, comprehensive model testing of its moonpool was considered to be necessary, and Statoil, who will be the main costumer, agreed to finance not only the 3-dimensional experiments but also the simplified 2-dimensional model tests described in this thesis.

Both 2-dimensional moonpool models, the base case and the *Seven Viking*-model, were tested without objects for a range of periods and excitation amplitudes. Also, the *Seven Viking* moonpool was tested with two different objects inside. Both objects had square cross sections, but were of different sizes.

The methodology outlined in DNV's guidelines for analysis of moonpool operations (DNV 2011) was applied on the same conditions as in the model tests. Comparison of the forces calculated with this method with the measured forces in the experiments was an essential part of the thesis, the point of which was to assess whether such a basic calculation method is able to predict forces with sufficient accuracy.

Another major point of interest was to apply PIV, particle image velocimetry, on the moonpool model to visualize the flow. PIV is a non-intrusive technique in which small

seeding particles are dissolved into the fluid, illuminated by a laser and photographed at short time intervals. Using algorithms based on correlation between succeeding time steps, it is possible to track the particle movements and thus to determine the velocity fields of the fluid. This was assumed to be an interesting part of the experiments regardless of the outcome, because the flow inside a moonpool had never before been visualized in this way and consequently the experiments became an opportunity to use PIV on a new application.

Furthermore, it was hoped that the PIV method could reveal important flow phenomena such as the predicted vortex shedding at the moonpool inlet. Another point was to try to determine whether there is any significant flow through the perforated moonpool walls or not, as this part of the moonpool is usually incorporated in the design mainly because of tradition and there has not been any unambiguous results proving their value in the damping of the fluid motion. Finally, by studying the surface elevation of a moonpool, one gets the impression that the fluid motion is quite homogeneous, i.e. the fluid moves symmetrically in the vertical direction only and in a tidy manner. PIV was used for determining the validity of this assumption.

Structure of thesis

Section 2 describes key background theory and research done on moonpools. The basic flow characteristics are discussed along with both simple and more complex methods of determining the fluid motions. Some previous experiments related to objects inside moonpools are discussed. After this, DNV's guidelines for analysis of moonpool-operations, the validity of which this thesis aims to test, are presented. Finally, a short summary of some of the important short-comings in the current knowledge of moonpools is given.

The rest of the thesis is mainly devoted to the current 2-dimensional model tests. First, in section 3, a presentation of the experimental set-up is given, describing the model itself, the instrumentation and the PIV set-up. This is followed by section 4, which describes the analysis methods that have been applied on the measured data and the PIV images.

In section 5, all results from the current model tests are presented and discussed. The section starts with the basic validation moonpool before moving on to the moonpool of *Seven Viking* with and without objects inside. Some PIV-figures are included here, but due to the large amount of plots produced, most of them have been put in an appendix and are only referred to in the results section. The results are discussed as they are presented. Because of the many points of interest in the experiments, it seemed appropriate to structure the report in this way.

There will always be uncertainties related to model tests. The most important issues are discussed in section 6.

Section 7 compares the results from the current experiments with the other 3-dimensional model tests done for *Seven Viking* and its moonpool, while section 8 compares the calculations based on the guidelines provided by DNV with the actual test results.

Finally, in section 9, a summarizing conclusion is given which highlights the most important findings, discusses their significances and briefly proposes further work.

2. Background theory and previous work

This section gives an overview of relevant background theory. The first chapter concerns fundamental flow mechanisms. After this follows a simplified scheme for describing the overall fluid motions in the moonpool, which is helpful for getting a basic understanding of the problem. More advanced methods have also been applied on the topic; some of these are presented as well. Historically, far less effort has been put into research of objects inside moonpool, but some studies have been performed and are presented here. At the end of the section, the practical guidelines for analysis of moonpool operations provided by DNV are presented. Finally, a short summary of the shortcomings in the knowledge of moonpools is included.

Fundamental flow characteristics

Piston and sloshing modes

A moonpool is usually modelled as a trapped body of water with motions described by a combination of piston and sloshing modes. The piston mode is a type of motion where the water can be seen as a "plug" which oscillates in the vertical direction. There is only one piston mode. A sloshing mode is a situation where there is a standing wave inside the moonpool. This implies both horizontal and vertical fluid motions.

Molin studied the modes of moonpools using linearized potential theory where the goal was to establish simple expressions for the natural frequencies associated with each mode (Molin 2001).

Potential theory is based on the following three assumptions (White 2008):

- Incompressible fluid
- Irrotational fluid
- Non-viscous fluid

Here, the fluid in question is water and therefore the first assumption is reasonable because water, for most practical purposes, can be regarded as incompressible. However, the two other assumptions can in some cases lead to results which differ significantly from reality. For the moonpool-elevation case especially the assumption about irrotationality is problematic, as will be discussed later.

In a fluid domain which fulfils the requirements of potential theory a function φ called the velocity potential can be found. In two dimensions this function is defined so that

$$u = \frac{d\varphi}{dx}$$
$$w = \frac{d\varphi}{dz} \qquad (1)$$

where u is the velocity in the x-direction (horizontal) and w is the velocity in the z-direction (vertical). The pressure p can then be found anywhere in the fluid with Bernoulli's equation (White 2008):

$$p + \rho g z + \rho \frac{d\varphi}{dt} + \frac{1}{2}\rho |\nabla\varphi|^2 = \text{constant} \qquad (2)$$

where ρ is the fluid density and g is the gravitational constant.

In Molin's research, infinitely deep water was assumed, and the vessel itself was fixed. The horizontal dimensions of the vessel were assumed to be considerably larger than the horizontal dimensions of the moonpool.

First a 2D moonpool with breadth b and draught h was studied. This corresponds to an imaginary moonpool with finite breadth and infinite length. It was found that as long as the moonpool was not very shallow (compared to the breadth) the modes could be regarded as uncoupled.

For the 2D results, the piston mode is called the 0-mode, while the sloshing modes are called mode 1, 2, 3 etc.

In reality, the piston motion in a moonpool induces waves that travel away from the vessel. In order to dissipate these waves (and their energy) in the numerical model, two potential sinks were positioned some distance H from the centre of the moonpool. The resulting equation for the natural frequency of the piston mode is given as (Molin 2001):

$$\omega_0^2 = \frac{g}{h + \left(\frac{b}{\pi}\right)\left(\frac{3}{2} + \ln\left(\frac{H}{2b}\right)\right)} \tag{3}$$

where g is the gravitational constant. To evaluate this it is necessary to make a choice for H which intuitively must be larger than b. Molin compared his formula with experimental tests and found that taking H/b=4.5 gave good results. Inserting this into the formula results in:

$$\omega_0^2 = \frac{g}{h + \left(\frac{b}{\pi}\right)\left(\frac{3}{2} + \ln\left(\frac{9}{4}\right)\right)} = \frac{g}{h + \kappa_{2D} \cdot b} \approx \frac{g}{h + 0.736b} \tag{4}$$

$$\kappa_{2D} \approx 0.736$$

The sloshing modes do not, at least according to the idealized potential theory, emit energy from the moonpool and no sinks need to be introduced. The natural frequencies for the first three sloshing modes are given by (Molin 2001):

$$\begin{aligned} \omega_1^2 &= g\frac{\pi}{b}\coth\left(\frac{\pi h}{b} + 1.030\right) \\ \omega_2^2 &= 2g\frac{\pi}{b}\coth\left(\frac{2\pi h}{b} + 1.488\right) \\ \omega_3^2 &= 3g\frac{\pi}{b}\coth\left(\frac{3\pi h}{b} + 1.666\right) \end{aligned} \tag{5}$$

The three first sloshing modes will result in standing waves inside the moonpool with surface shapes approximately as indicated on the sketch in Figure 3.

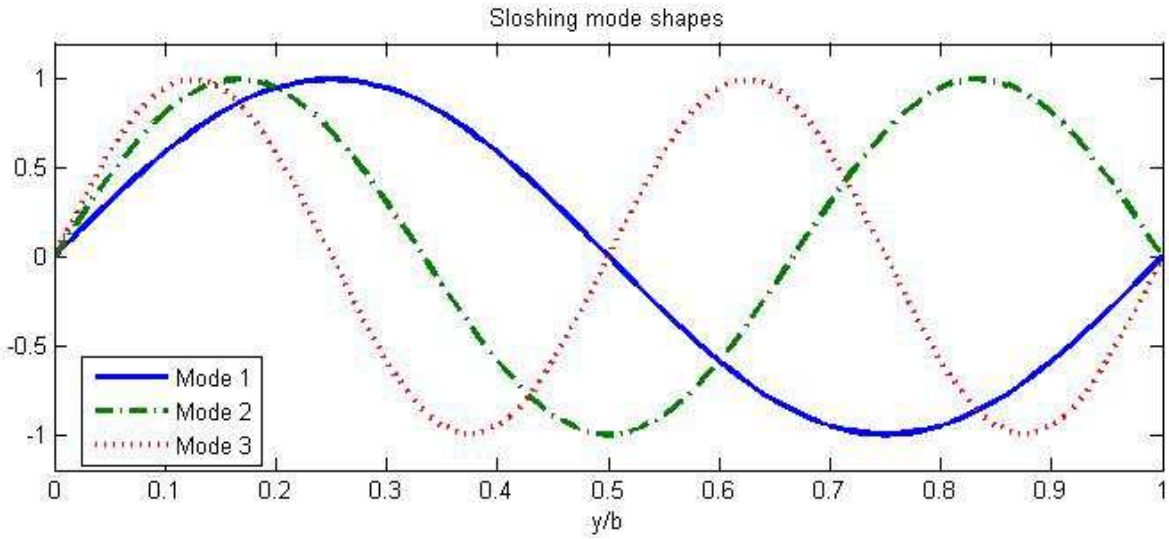

Figure 3 - Idealized surface shapes of sloshing modes

By taking

$$T_i = \frac{2\pi}{\omega_i} \tag{6}$$

the natural periods of the piston mode and the three first sloshing modes can be investigated closer. Examining the natural periods is important in order to determine which modes are likely to be found in a moonpool. By looking at a scatter diagram, e.g. for the North Sea (Faltinsen 1990), one can see that sea states with peak periods of 4 seconds or lower are rarely observed, and if they are observed, they have very low total energy (low significant wave height). Therefore, a system with natural period of 4 seconds or lower will not be excited to a significant extent by normal sea states.

In order to investigate the effect of varying horizontal extension, the natural periods are plotted for a moonpool with a draught of 5m and breadth ranging from 3m to 25m in Figure 4.

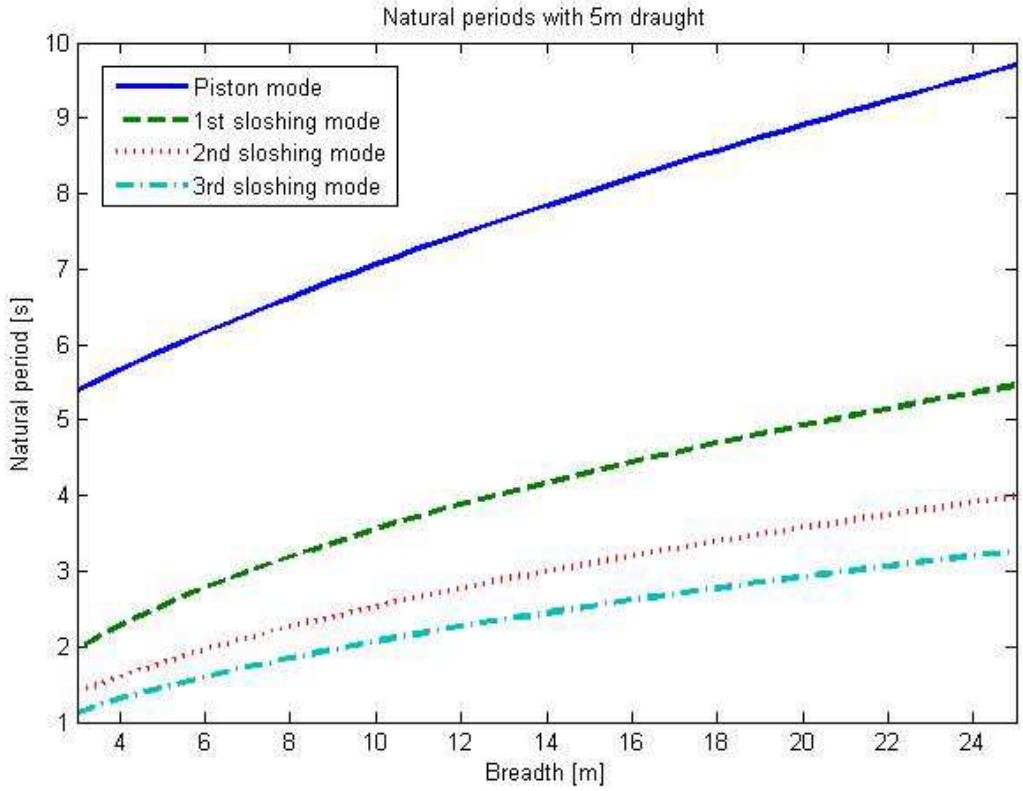

Figure 4 - Natural periods at constant draught

If the draught is varied instead, the result will be as Figure 5. Here the breadth is set to 7m.

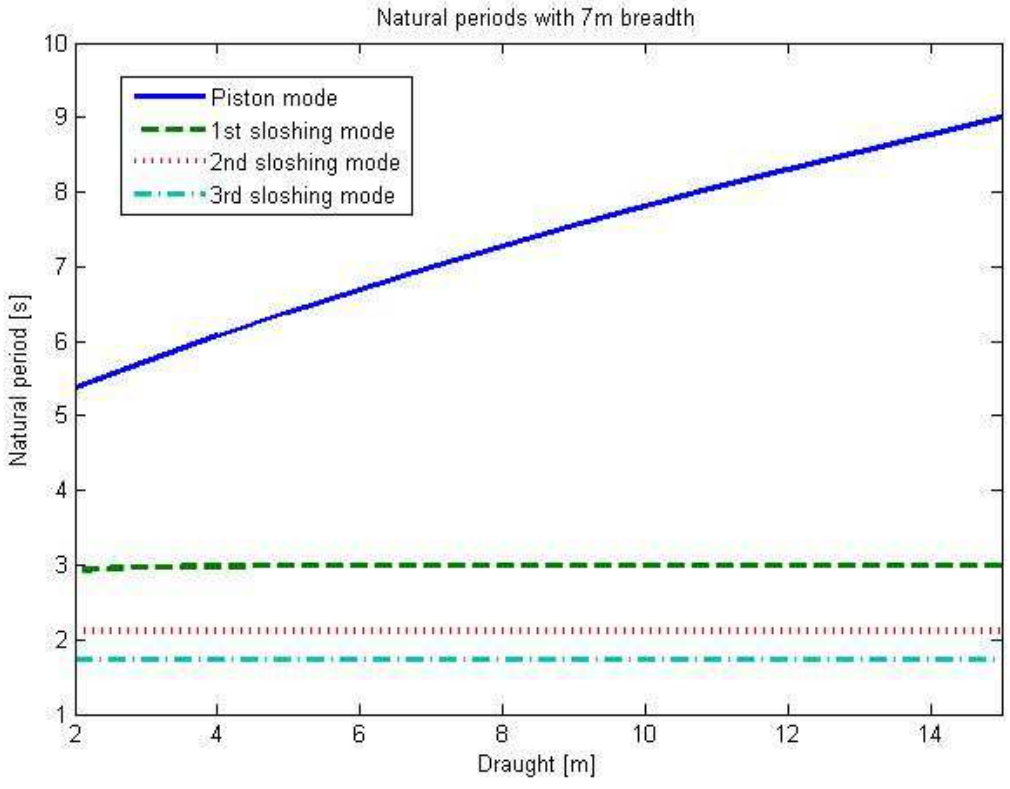

Figure 5 - Natural periods at constant breadth

The behaviour of the natural periods of the sloshing modes is very interesting. The natural periods are almost exclusively dependent on the horizontal extension of the moonpool. Molin's motivation for his study was to examine very large moonpools. A barge with a moonpool with a horizontal extent of 80m x 20m is mentioned and if Figure 4 is extrapolated it can be seen that the natural periods of the sloshing modes may have natural periods higher than 4 seconds. However, the horizontal extent of moonpools found on normal offshore installation vessels is typically between 5 and 12m, which implies that all the sloshing modes will have natural periods below 4 seconds. This means that for ships with conventional moonpools only the piston mode is of practical importance.

Unlike the sloshing modes, the piston mode is dependent on both the draught and the breadth of the moonpool.

So far a 2D moonpool with infinite length has been considered, but Molin went further and developed an expression for the resonance frequency of the piston mode for a 3D moonpool as well. The moonpool has draught h, breadth b and finite length l. The equation is (Molin 2001):

$$\omega_0^2 = \frac{g}{h + b \cdot f_3(b,l)} \tag{7}$$

where f_3 is a function of the relationship between b and l. This equation is identical to the equation for the 2D frequency, except that the value κ has been replaced by the function f_3 which is given as (Molin 2001):

$$f_3 = \frac{1}{\pi}\left(\sinh^{-1}\left(\frac{l}{b}\right) + \frac{l}{b}\sinh^{-1}\left(\frac{b}{l}\right) + \frac{1}{3}\left(\frac{b}{l} + \frac{l^2}{b^2}\right) - \frac{1}{3}\left(1 + \frac{l^2}{b^2}\right)\sqrt{1 + \frac{b^2}{l^2}} \right) \tag{8}$$

This equation is quite complex. It is plotted in Figure 6 for l/b ranging from 0.2 to 5.

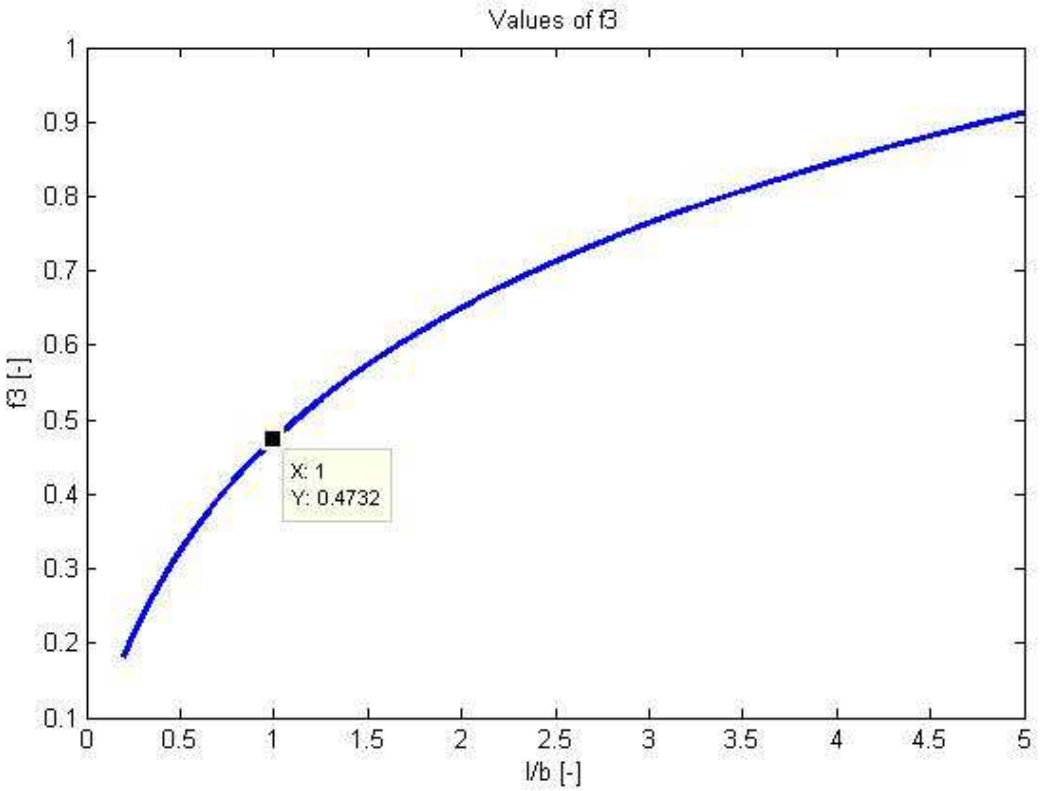

Figure 6 - Values of f3

The value of f_3 where l/b=1 (square-shaped moonpool) is highlighted and will from now on be called

$$\kappa_{3D,square} \approx 0.473 \tag{9}$$

From the graph, it may look like the 2D-value, κ_{2D}=0.736, could correspond to a 3D case with a length/breadth ratio of around 2.7 but it would in fact not be correct to compare these results directly. The reason is, according to Molin, that the 2D case is somewhat artificially simulated as "there can be no piston mode in two dimensions unless some tricks are applied to simulate the outer free surface".

For comparison between the 2D "infinite length" results and the 3D results with l=b, the plot in Figure 7 shows the corresponding natural periods for ratios between draught and breadth ranging from 0.4 to 2.5. The natural period is made dimensionless by multiplying with the square root of (g/h), i.e. the y-axis is given as

$$T\sqrt{\frac{g}{h}} \tag{10}$$

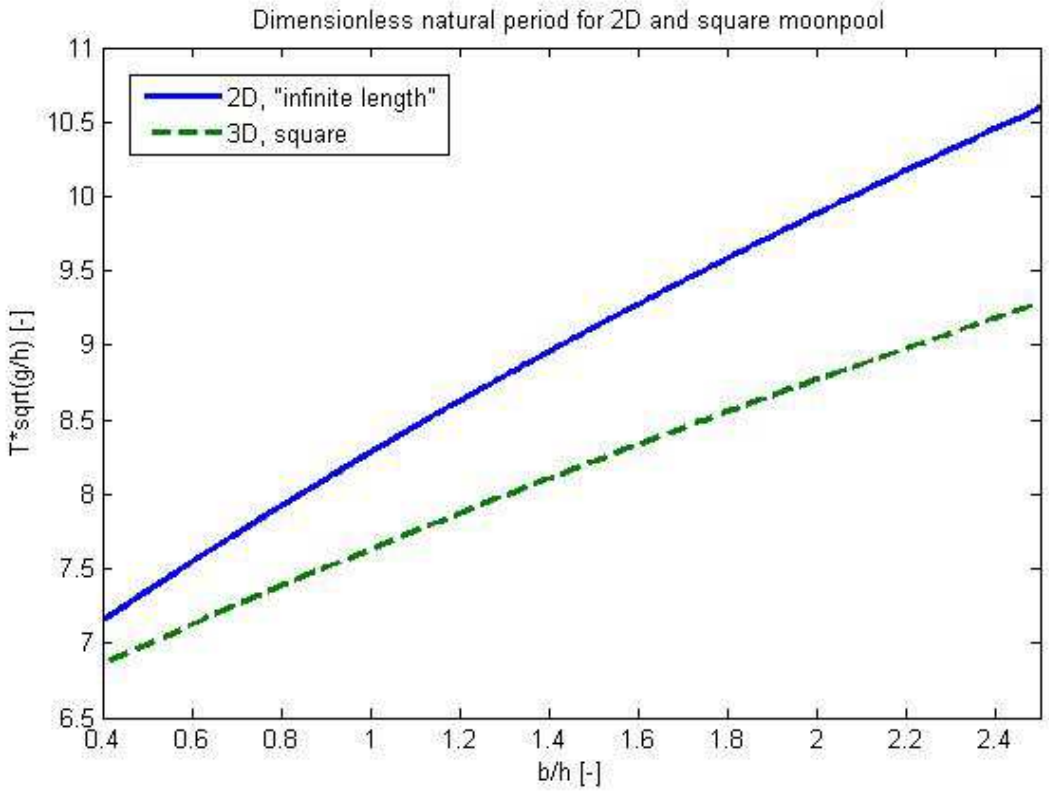

Figure 7 - Natural period of piston mode

The general trend is that the 3D square moonpool has a lower natural period than the corresponding 2D moonpool. However, the difference is not very large; between 5% and 15% for the interval seen here.

As mentioned in the beginning of this chapter, Molin used potential theory to solve the problem. Potential theory represents an idealized world which in some cases may differ significantly from reality. So how accurate are the equations for the natural periods presented here?

Molin himself compared his results with equivalent set-ups modelled in a commercial potential theory panel program. He found satisfactory agreement for the natural periods. One should of course remember that the commercial potential theory programs also have their shortcomings when it comes to moonpool simulations, but these shortcomings are found mainly to be related to the amplitude of the wave elevation at resonance and not in the prediction of the natural period (Kristiansen et al. 2011).

Therefore, following this argument, it seems natural to conclude that the formulae derived here is very helpful for the prediction of natural periods of moonpools. However, these equations are only valid for moonpools with a constant cross section. For more complex geometries some modifications are necessary.

Flow separation and vortex shedding at inlet

With the approach of Molin, the modes of the motions inside a moonpool can be determined and the implication for conventional offshore construction vessels is that the piston mode is dominating. This means that the water inside the moonpool can be regarded as a water plug oscillating in the vertical direction. Additionally, the resonance period can be found quite accurately.

However, it turns out that the amplitude of the motion will generally be over predicted using normal potential theory, especially near resonance. This clearly suggests that there are important damping-effects present in the flow inside the moonpool which, due to the restrictions imposed by potential theory, are not captured. The only source of damping that potential theory is able to predict is the energy loss from radiated waves.

By empirically adding quadratic damping to the equation of motion for the water plug, it is possible to get results which are quite close to those obtained from model tests (Aalbers 1984). But doing this does not increase the understanding of the flow conditions inside the moonpool, other than providing a hint that it is a non-linear effect.

Kristiansen et al. did a study to shed new light on the source of this non-linear effect (Kristiansen et al. 2008). The results indicated that vortex shedding and flow separation at the inlet of the moonpool is the source of the non-linear damping. A 2D numerical wavetank based on non-linear potential theory was used as a basis. On its own, this scheme is not able to capture effects of flow separation and vortex formation. Therefore an inviscid vortex tracking method was included in the model.

The analysed numerical wave tank can be seen in Figure 8. Symmetry is assumed at the vertical line in the middle of the moonpool, so that this wavetank only represents half of the full domain.

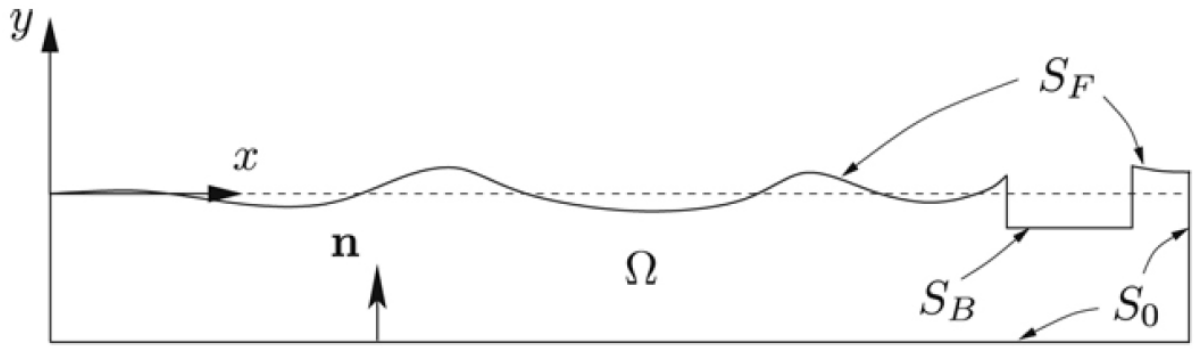

Figure 8 - Numerical wave tank (Kristiansen et al. 2008)

Ω is the fluid domain, S_F is the free surface, S_B is the fluid boundary at the body and S_0 is the fluid boundary at the tank walls and at the line of symmetry.

For the general fluid domain, potential theory (as described earlier in this section) is assumed, i.e. there exists a velocity potential φ which satisfies:

$$\nabla^2\varphi = 0 \quad \text{in } \Omega \tag{11}$$

and where the fluid velocities, u and v, are defined as:

$$u = \frac{\partial \varphi}{\partial x}, \quad v = \frac{\partial \varphi}{\partial y} \tag{12}$$

If unmodified potential theory is used to describe the flow around a sharp corner, the result will be a singularity at the corner point where the velocities will approach infinity. This is of course not representative of a real flow which will separate at the corner. Vorticity, represented by a free shear layer, is shed into the fluid domain. In Kristiansen et al.'s model, the separated free shear layer is assumed to be thin, so that the vorticity can be represented by a strip. Figure 9 illustrates how the shear layer is shed from the sharp corner.

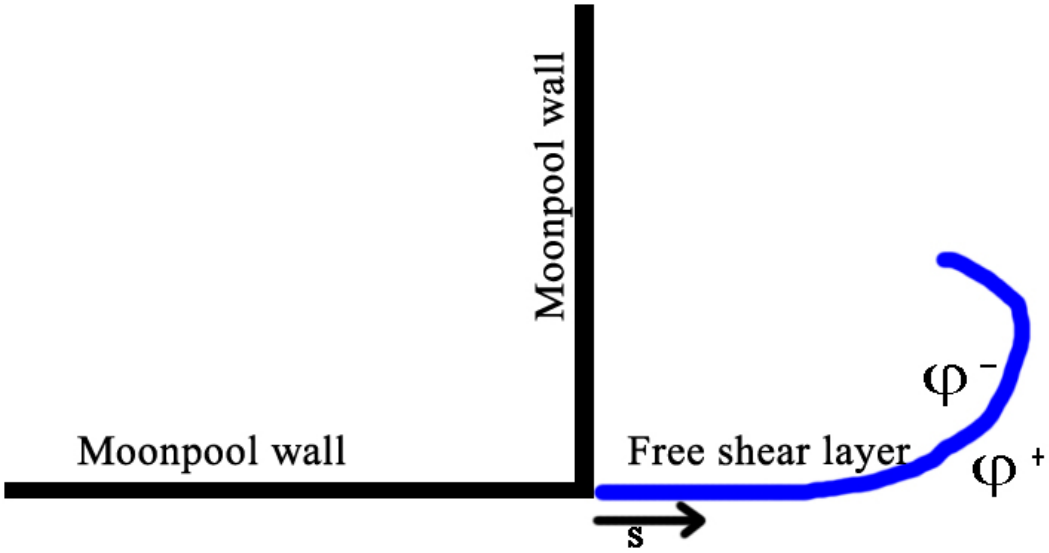

Figure 9 - Shear layer separation

The s-axis represents a local 1D coordinate system which follows the free shear layer all the time. At the corner of the moonpool, s=0.

Bernoulli's equation is used as the basis of the vortex tracking method. It is given as:

$$p + \rho \frac{\partial \varphi}{\partial t} + \frac{1}{2}\rho |\nabla \varphi|^2 + \rho g y = c \tag{13}$$

where p is the pressure, ρ is the fluid density, g is the gravitational constant and c is an arbitrary constant. As specified on Figure 9, there is a jump in the velocity potential across the free shear layer. On one side the potential is denoted φ^+, on the other it is φ^-. However, according to Prandtl's boundary layer equations there is no pressure drop across a thin shear layer (White 2008). Inserting into Bernoulli's equation results in:

$$\frac{\partial \varphi^+}{\partial t} - \frac{\partial \varphi^-}{\partial t} + \frac{1}{2}\left|\nabla \varphi^+\right|^2 - \frac{1}{2}\left|\nabla \varphi^-\right|^2 = 0 \tag{14}$$

The difference between the potentials is defined as the circulation intensity:

$$\Gamma = \varphi^{+} - \varphi^{-} \tag{15}$$

and a velocity vector $\mathbf{U_c}$ is defined as:

$$\mathbf{U}_C = \frac{1}{2}\left[\frac{\partial \varphi^{+}}{\partial x} + \frac{\partial \varphi^{-}}{\partial x}, \frac{\partial \varphi^{+}}{\partial y} + \frac{\partial \varphi^{-}}{\partial y}\right] \tag{16}$$

This results in

$$\frac{\partial \Gamma}{\partial t} + \mathbf{U_C} \cdot \nabla \Gamma = 0 \tag{17}$$

This is an advection equation, implying that Γ does not change when following at path defined by $\mathbf{U_c}$. By integrating $\mathbf{U_c}$ in time, the developing geometry, $\mathbf{x_s}$, of the free shear layer can be found.

At the corner, s=0, from where the separation occurs, the Kutta condition is imposed. This requires the potential to vary smoothly at the corner, instead of producing a singularity as will happen with unmodified potential theory. To achieve this, the potential on the body at s=0 is set to the same value as Γ at this point,

$$\Gamma(0) = \Gamma_0 \tag{18}$$

How Γ changes at the separation point is also found from Bernoulli's equation:

$$\frac{\partial \Gamma}{\partial t} = \pm \frac{1}{2} {U_S}^2 \tag{19}$$

where U_s is the fluid velocity just outside the boundary layer at the corner on the side where the shedding occurs.

The theory presented above was implemented into the numerical wavetank. In theory, the scheme should be able to track the free shear layers for any time interval. However, it turned out that the vorticities soon became too complicated to keep track of, hence some manipulation had to be done.

When the flow past the corner is harmonic, two vortex pairs will be shed every half cycle. The pairs will consist of two vortices which have the same absolute strength, but with opposite directions. It is assumed that these will influence each other in a way that makes them travel away from the corner and into the fluid domain. The shedding process, as well as the manipulation of the numerical scheme can be described by the aid of Figure 10.

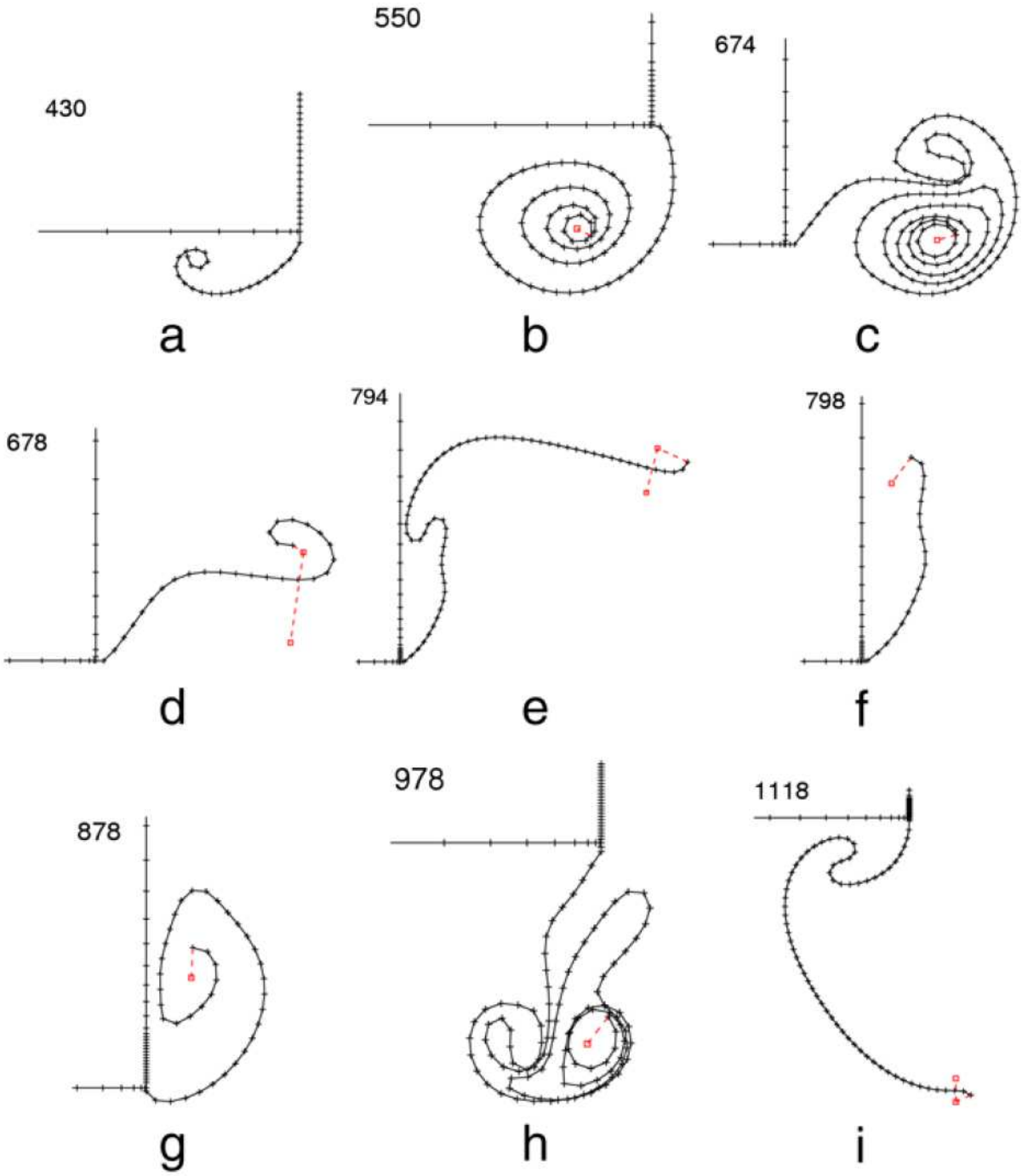

Figure 10 - Illustartion of vortex shedding process over one cycle (Kristiansen et al. 2008)

With reference to the small letters in the figure:

a) The ambient flow is going out of the moonpool. A free shear layer is shed from the corner, and it is beginning to curl up.
b) The vortex sheet has made a spiral.
c) The ambient flow is turning. Because of interaction with the wall, another vortex sheet spiral has started to form; the vorticity is going in the other direction compared to the first vortex.
d) The two original vortex sheet spirals have been replaced by two discrete vortices positioned where the vortex spirals had their centre.

e) The ambient flow has now started going into the moonpool. A new vortex sheet spiral is starting to form as in step a, except that it is now inside the moonpool.
f) The two "old" discrete vortices are identified as a vortex pair where the two vortices are equally strong but with different signs. They are assumed to travel away from the body, and they are therefore deleted.
g) The new vortex sheet spiral inside the moonpool continues to form as the ambient flow into the moonpool slows down and is about to turn.
h) Because of interaction with the wall, a second vortex sheet spiral (again with the opposite direction) is starting to form. The ambient flow has started going out of the moonpool.
i) One cycle is completed. The two vortex sheet spirals have been gathered into two discrete vortices and a new vortex sheet spiral is starting to form just as in step a. The two discrete vortices are about to be deleted.

With this treatment of the shed vortices, the numerical scheme became stable. The question now was how well it predicted the moonpool wave elevation. To determine this, calculated surface elevation amplitudes were compared with experimental tests with a corresponding set-up. A variety of different conditions and geometries were tested. Included here is one example, presented in Figure 11.

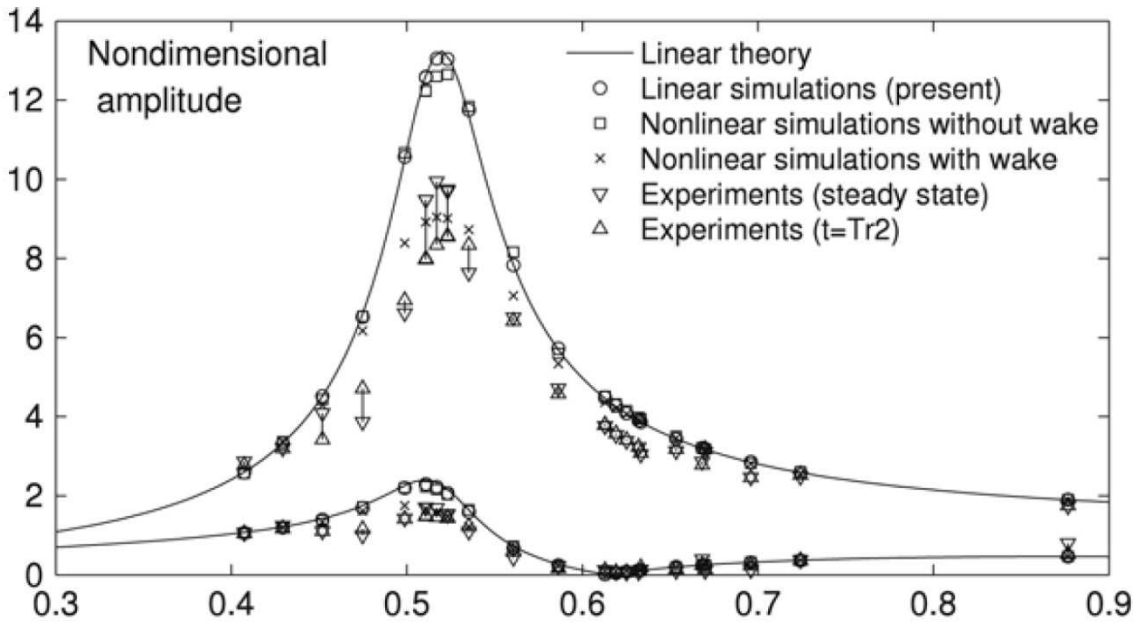

Figure 11 - Non-dimensional amplitude of response (Kristiansen et al. 2008)

The figure shows the non-dimensional wave elevations inside the moonpool (line and points on top) and "far away" at a point outside the moonpool. Results are included from unmodified linear potential theory (which doesn't include vortex shedding), nonlinear simulations without wake (which include non-linear free surface but not vortex shedding), nonlinear simulations with wake (includes vortex shedding) and experimental results.

The experimental results are represented by two values. The reason for this is that the wave beaches in the tank were rather ineffective (or poorly tuned) so that the reflected waves are assumed to be of some importance. Therefore, one value termed "t=Tr2" was extracted before the reflected waves reached back to the moonpool and another termed "steady state" was

extracted from a longer time series when the elevation had reached a steady state. The bar drawn between these two values is meant to indicate uncertainties in the experiments and should not be interpreted as a statistical confidence interval.

There are two points to be made from Figure 11:

- All numerical methods predict a correct resonance frequency and correct amplitude of the motions at frequencies far away from resonance.
- Only the scheme which includes vortex shedding predicts accurate amplitude close to resonance frequency.

Based on Kristiansen et al.'s work, it is natural to conclude that the effect which contributes to the non-linear damping is indeed flow separation and vortex shedding at the inlet of the moonpool.

Consequently, the inlet of a moonpool should be constructed in a way that maximizes the vortex shedding. If the inlet has rounded edges, there will only be modest vortex shedding effects. If on the other hand the inlet has a sharp corner, the vortex-induced damping will be considerable. This is the inlet type Kristiansen et al. studied.

Adding appendages (plates) at the inlet, as in Figure 12, results in an even better design with respect to wave elevation.

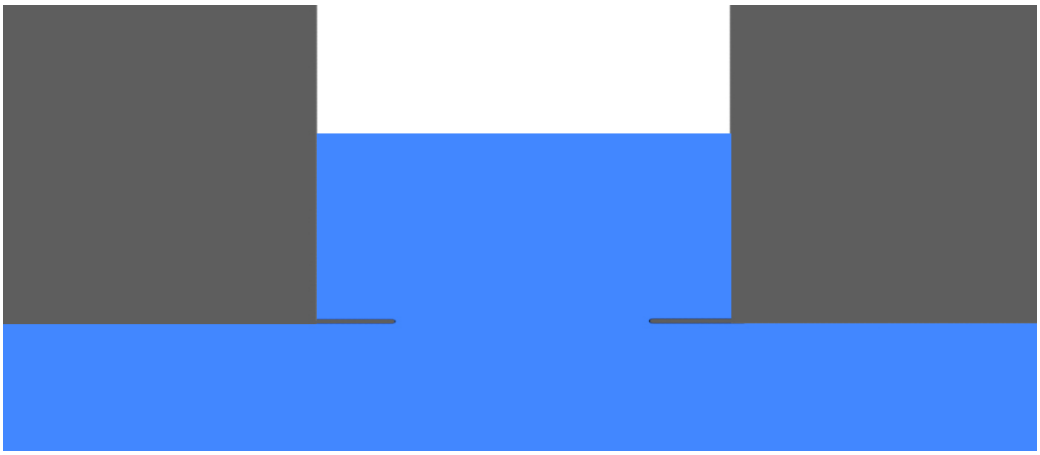

Figure 12 - Moonpool with damping plates at inlet

According to Graham (Graham 1980) the forces (i.e. the damping) caused by vortex shedding is larger for a sharp plate than for a square. Therefore an appendage as seen on the figure will be better than a straight inlet. This has also been shown in model tests, e.g. by Torres et al. (Torres et al. 2008) and Kristiansen et al. (Kristiansen et al. 2011). The drawback of appendage plates, from a practical point of view, is that they reduce the effective area of the moonpool.

Many moonpools also have perforated walls inside them as indicated on Figure 13. Whether this increases the damping of the piston mode or not is a disputed question.

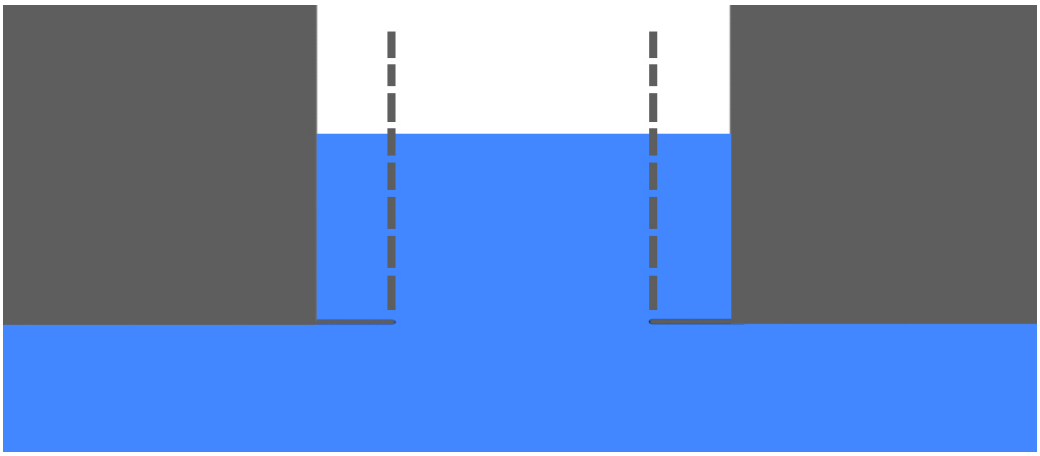

Figure 13 - Moonpool with damping plates and perforated walls

Derivation of simplified mass/spring model

Physical systems with periodic motions are often described using a simplified mass/spring model. Here, the derivation of such equations for a moonpool's piston mode is presented. Two different approaches by Aalbers (Aalbers 1984) and Madsen (Madsen 1980) are included.

The equations derived in this section are valid for moonpools with constant cross sectional area A. T is the mean fluid level in the moonpool, i.e. the distance from the bottom of the moonpool to the mean free surface. $\zeta(t)$ is the instantaneous surface elevation from mean level. Because the fluid in the moonpool is regarded as a plug of water, the vertical fluid motion in the entire moonpool is assumed to be identical to the surface elevation. ζ_S is the heave motion of the ship at the position of the moonpool and ζ_B is the vertical motion of the body in the moonpool. ρ is the fluid density.

Aalbers' equation

Aalbers starts by looking at a moonpool in a fixed vessel. For a control volume taken over the entire fluid domain inside the moonpool, the momentum conservation equation can be written on the following integral form:

$$\frac{\delta}{\delta t}\iiint_{\Omega}\rho v_j dV+\iint_{d\Omega}\rho v_j \vec{v}\cdot\vec{n}dS=\iiint_{\Omega}\rho f_j dV+\iint_{d\Omega}P_{jk}n_k dS \tag{20}$$

where Ω is the volume, $d\Omega$ is the surface, v is the velocity in all directions, n is the normal vector on the surface, f is a volume force and P is the external pressure. Now, assuming gravity g is the only volume force and that the only velocity component in the moonpool is the vertical velocity, ζ, the equation reduces to

$$\frac{\delta}{\delta t}\left(\rho A(T+\zeta)\dot{\zeta}\right)-\rho A\dot{\zeta}^2=\rho Ag(T+\zeta)+\iint_{d\Omega}P_{jk}n_k dS \tag{21}$$

The pressure forces as described here acts only on the top and bottom of the moonpool and only normal on the fluid surface. This implies that there are no effects of viscosity included. Applying Bernoulli's equation gives an expression for the pressure difference:

$$\begin{aligned}\iint_{d\Omega}P_{jk}n_k dS &= -0.5\rho A\dot{\zeta}^2-\rho AgT-\rho\iint_{s}\frac{\partial\phi}{\partial t}ndS \\ &= -0.5\rho A\dot{\zeta}^2-\rho AgT-a_\zeta\ddot{\zeta}-b_\zeta\dot{\zeta}+\text{higher order terms}\end{aligned} \tag{22}$$

where φ is the velocity potential of the fluid and a and b are the added mass and damping coefficients. The last transform resulting in the added mass and damping terms comes from the Haskind relations. Inserted, the equation of motion becomes:

$$(\rho A(T+\zeta)+a_\zeta)\ddot{\zeta}+b_\zeta\dot{\zeta}+\rho Ag\zeta+\text{higher order terms}=0 \tag{23}$$

At this point Aalbers introduces a term for taking non-linear damping effects into account. These effects include friction and vortex shedding. The term is on the following form:

$$b_2 |\dot{\zeta}| \dot{\zeta} \tag{24}$$

The next step is to take the vertical ship motions, ζ_S ,into account. The non-linear damping term now becomes dependent of the moonpool motions relative to the ship. In addition, Aalbers allows the moonpool to affect the vessel's damping and added mass. This is modelled by including a term with an added mass interaction coefficient, d, and a term with a damping interaction coefficient, e. Finally, if wave excitation forces F_{wave} are included the resulting governing equation becomes:

$$(\rho A(T+\zeta)+a_\zeta)\ddot{\zeta}+b_\zeta\dot{\zeta}+b_2|\dot{\zeta}-\dot{\zeta}_S|(\dot{\zeta}-\dot{\zeta}_S)+\rho Ag\zeta+d\ddot{\zeta}_S+e\dot{\zeta}_S=F_{wave} \tag{25}$$

The equation is relatively simple, but it contains non-linear terms and therefore requires a solution in the time domain unless linearized approximations are introduced. The equation also contains several coefficients. According to research done by Aalbers, all of them can be determined theoretically with a reasonable degree of accuracy with the exception of the non-linear damping coefficient. Aalbers recommends using empirical results from model tests for this parameter.

Based on comparisons with model tests, Aalbers concludes that this equation is useful for understanding the behaviour of the water column inside a moonpool, assuming the coefficients are determined with sufficient accuracy.

Madsen's equation

Madsen uses a slightly different approach and includes some extra non-linear terms in his final equation. The first step is to establish the momentum P of the fluid in the moonpool, given by

$$P=\rho A(T+T'+\zeta)\dot{\zeta} \tag{26}$$

where the term ρAT' represents the added mass and T' is an equivalent length suggested by (Fukuda 1977) to be

$$T'=0.45\sqrt{A} \tag{27}$$

The factor of 0.45 relates to the κ-factor found by Molin (Molin 2001).

According to Newton's second law of motion the external forces on an object equals the momentum differentiated with respect to time, that is

$$\frac{dP}{dt}=\rho A(T+T')\ddot{\zeta}+\rho A\dot{\zeta}^2+\rho A\zeta\ddot{\zeta}=\sum \text{all external forces} \tag{28}$$

The external forces consist of wave forces (F_{wave}), restoring forces ($-\rho gA\zeta$), and non-linear damping forces. The force acting on the fluid at the inlet of the moonpool can be written as:

$$F_{entrance} = -\frac{\gamma}{2}\rho A|\dot{\zeta} - \dot{\zeta}_S|(\dot{\zeta} - \dot{\zeta}_S) \tag{29}$$

where γ is a constant which can be set to 1 for flow running out of the moonpool (Massey 1975). For flow running in, it depends on the geometry. This term is meant to include effects of flow separation. An empirical non-linear damping term is also included in a similar way:

$$F_{damping,other} = -\frac{\beta}{2}\rho A|\dot{\zeta} - \dot{\zeta}_S|(\dot{\zeta} - \dot{\zeta}_S) \tag{30}$$

where β is an empirical constant. Collecting all force terms yields the final equation for the fluid motion in the moonpool:

$$\rho A(T + T')\ddot{\zeta} + \rho A\dot{\zeta}^2 + \rho A\zeta\ddot{\zeta} + \frac{\beta + \gamma}{2}\rho A|\dot{\zeta} - \dot{\zeta}_S|(\dot{\zeta} - \dot{\zeta}_S) + \rho g A\zeta = F_{wave} \tag{31}$$

For verification of the equation, Madsen did a series of model tests. He concludes that the equation gives a satisfactory description of the fluid motions inside the moonpool, although also in this case the non-linear damping had to be determined based on model tests. The γ-factor alone was not enough to get a good correspondence between numerical and experimental results.

Differences and similarities

The two equations are essentially the same, with the exception of the terms proportional to the velocity. The non-linear damping term derived by Madsen looks different from Aalber's equation, but it is just described by a combination of several constants instead of only b_2.

Aalbers includes a linear damping term that is not included by Madsen. On the other hand, Madsen includes an extra non-linear damping term that is proportional to the absolute fluid velocity squared (the other non-linear damping term is proportional to the relative velocity squared). This is one of the terms that Aalbers calls "higher order terms" and neglects. Both these terms turn out to be of little significance compared to the main non-linear damping term.

Body inside moonpool

Madsen takes it one step further than Aalbers and expands his equation to include a body inside the moonpool. The hydrodynamic forces on the object are assumed to be given by Morison's formula (for relative motion):

$$F_{body} = \rho V(1+C_M)\ddot{\zeta} - \rho V C_M \ddot{\zeta}_B - \frac{1}{2}\rho A_B C_D \mid \dot{\zeta}_B - \dot{\zeta} \mid (\dot{\zeta}_B - \dot{\zeta}) \tag{32}$$

where C_M is the added mass coefficient for the body, C_D is the drag coefficient, V is the volume of the body and A_B is the vertical projected area of the body.

The body will also give a contributing term to the change in momentum of the fluid in the moonpool given by:

$$\left.\frac{dP}{dt}\right|_{Body-effect} = -\rho V \ddot{\zeta}_B \tag{33}$$

The minus sign is explained by the fact that "the momentum in the surrounding liquid caused by the bell moving upwards with a velocity is equivalent to that of the same volume of water moving downwards with the same velocity" (Madsen 1980).

Combining these new terms with the equation already derived for the empty moonpool results in Madsen's final equation:

$$\begin{aligned} &\rho A(T+T')\ddot{\zeta} + \rho A\dot{\zeta}^2 + \rho A\zeta\ddot{\zeta} + \frac{\beta+\gamma}{2}\rho A \mid \dot{\zeta} - \dot{\zeta}_S \mid (\dot{\zeta} - \dot{\zeta}_S) + \rho g A\zeta \\ &-\frac{1}{2}\rho A_B C_D \mid \dot{\zeta}_B - \dot{\zeta} \mid (\dot{\zeta}_B - \dot{\zeta}) - V(1+C_M)(\ddot{\zeta}_B - \ddot{\zeta}) = F_{wave} \end{aligned} \tag{34}$$

Also this equation, when solved in the time-domain, was found to give good agreement with experiments, as long as the coefficients were determined.

Advanced numerical methods applied on moonpools

Solution of the Navier-Stokes equations (CFD)

The Navier-Stokes equation is a non-linear partial differential equation which is derived from Newton's second law of motion. It is valid for a fluid particle and is in theory capable of describing any fluid motion when solved. Assuming incompressibility and Newtonian fluid (which is true for water), the equation can be written on the following form:

$$\rho\left(\frac{\partial \vec{v}}{\partial t}+\vec{v}\cdot\nabla\vec{v}\right)=\rho g-\nabla p+\mu\nabla^2\vec{v} \tag{35}$$

where ρ is the fluid density, v is the velocity vector, g is the gravitational constant, p is the pressure and μ is the fluid viscosity. This is a vector equation, so it can be split into three components. This results in an equation system with three equations and four unknowns (three velocity components and pressure). The continuity equation is used to close the system:

$$\nabla\cdot\vec{v}=0 \tag{36}$$

Except for a few very simple cases, the only way to solve the Navier-Stokes equation is to discretize the fluid domain and solve an integral form of the equation for each element. This is often called computational fluid dynamics, or just CFD. CFD can be very time-consuming even for powerful modern computers. Because of this, simplifications are often necessary. For the moonpool-elevation case most work has been done in two dimensions, which makes the problem considerably less challenging.

To account for the free surface, a volume of fluid model is often used. The volume of fluid, VOF, method makes it possible to solve a problem with two fluids, in this case air and water. In every cell of the discretized fluid domain, a separate equation which determines the fraction of one of the fluids in the cell is solved (Ferziger et al. 2002). If this fraction is denoted c (must by definition be between 0 and 1) the extra transport equation can be written as

$$\frac{\partial c}{\partial t}+\nabla\cdot c\vec{v}=0 \tag{37}$$

There are two major drawbacks with the method; it increases computational time and it cannot represent an exact sharp boundary (like a free surface) on its own.

Heo et al. compared several methods for calculating the wave elevation in an empty moonpool including a potential scheme and a CFD scheme, both in two dimensions (Heo et al. 2010). Figure 14 shows the analysed cases. The twin-hull structure is given a forced harmonic motion with an amplitude of 0.0025m.

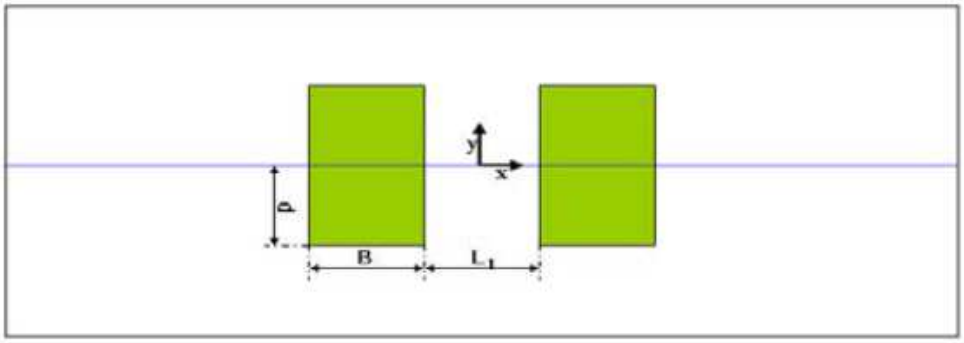

Figure 14 - Analysed case (Heo et al. 2010)

B=0.36m, d=0.18m and L=0.18m (Case A) and L=0.36m (Case B).

The results from both the potential and the CFD approach are presented in Figure 15 for Case A and Case B, along with potential and experimental results for a similar set-up, found by Faltinsen et al. (Faltinsen et al. 2007).

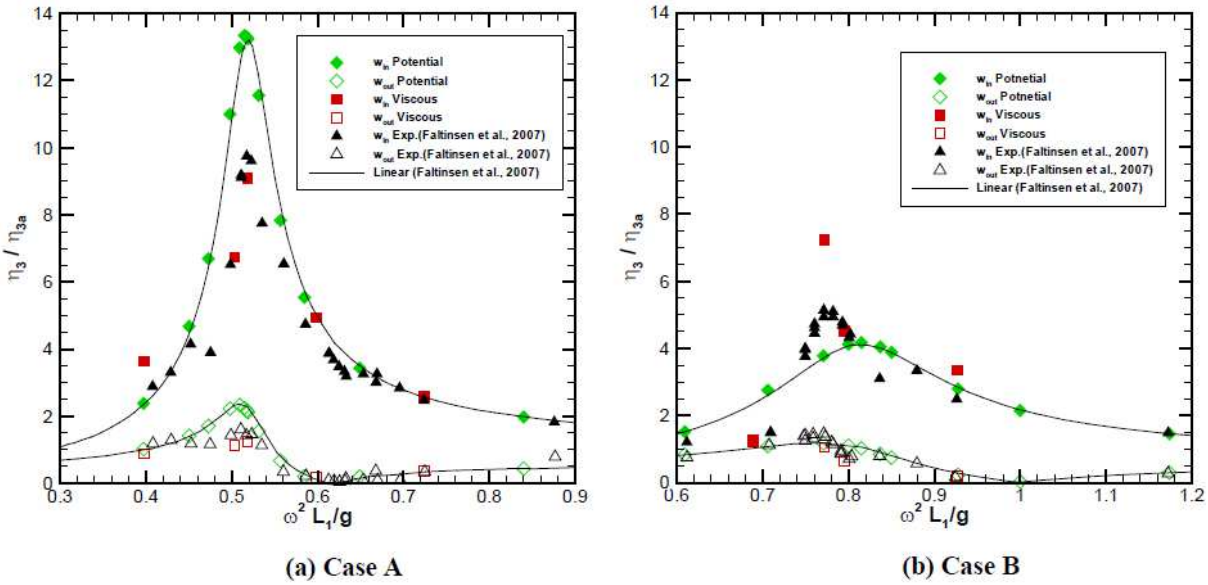

(a) Case A (b) Case B

Figure 15 - Non-dimensional response amplitude (Heo et al. 2010)

The non-linear potential method, termed “w_potential” produces almost exactly the same results as the linear method of Faltinsen, i.e. the inclusion of non-linear terms does not give any significant improvement for this application. However, the authors claim that “the wave height is so small that nonlinearity is not occurred”, suggesting that more severe motions may give different and, assumingly, better results with a nonlinear code.

The CFD-results are termed “viscous” in Figure 15. Due to the small motions, the flow was assumed to be laminar and no turbulence model was adopted. A VOF-method was used.

For case A the results from the CFD calculations are generally very good. At resonance this method predicts elevations which are quite close to those obtained in the model tests while both potential schemes over-predict the elevation.

The results from case B are not as unambiguous. The CFD results coincide very well with the experimental results also here except at resonance; where for some reason the calculation significantly over-predicts the elevation. Unfortunately Heo et al. do not discuss why this happened and it is hard to tell whether there is a flaw in the method itself or whether something simply went wrong for this particular simulation.

In spite of this single discrepancy, Heo et al. concludes that “CFD can simulate the flow characteristics of the two-dimensional moonpool including the piston mode, and the overall accuracy compared to the experimental results is acceptable”.

A possible simplification of the Navier-Stokes equation is to disregard the viscosity term. The equation is then reduced to the so-called Euler-equation. In order to investigate the effect of viscosity Heo et al. tried this approach as well. A consequence of this assumption is that there will be no friction between the fluid and the walls of the moonpool. The results were compared with the results from the full Navier-Stokes equation and it turned out that the effect of friction was of little importance compared to the effect of vortex shedding (vortex shedding effects at a sharp corners are captured also by the Euler equation). This is also the conclusion of Aalbers (Aalbers 1984) who states that “the magnitude of the frictional damping is very small and may be neglected in comparison with the potential damping and energy loss due to vortices".

Kristiansen’s hybrid scheme

Two key points made so far in this section are:

- CFD can in most cases predict the moonpool elevation with sufficient accuracy. However, the method is computationally very demanding. This makes it an unpractical tool if many configurations or environmental conditions need to be analysed.
- Potential theory will in general over-predict the motions in a moonpool especially at resonance because of its inability to include flow separation.

Kristiansen et al. found a clever way to combine the best characteristics of both methods while at the same time eliminating the weaknesses (Kristiansen et al. 2011). The presence of the free surface is the main reason why a full CFD simulation is so computationally demanding for this application. The free surface has to be dealt with by an interface-capturing method, usually VOF as described earlier. However, Kristiansen realized that the surface and the water close to the surface can be simulated with sufficient accuracy using potential theory. On the other hand, only CFD can predict the fluid motions at the entrance of the moonpool where the crucial vortices are formed.

Keeping these principles in mind, Kristiansen constructed a numerical model where the fluid domain is divided in two:

- The fluid at and near the surface is governed by linear potential theory. Also, far away from the body potential theory is used for all water depths.
- In the rest of the fluid domain, the full Navier-Stokes equations are applied.

The resulting discretized fluid domain of the numerical wavetank can be seen in Figure 16 where the potential theory domain is blue and the CFD domain is red. Like many others, Kristiansen assumed symmetry about the moonpool centre.

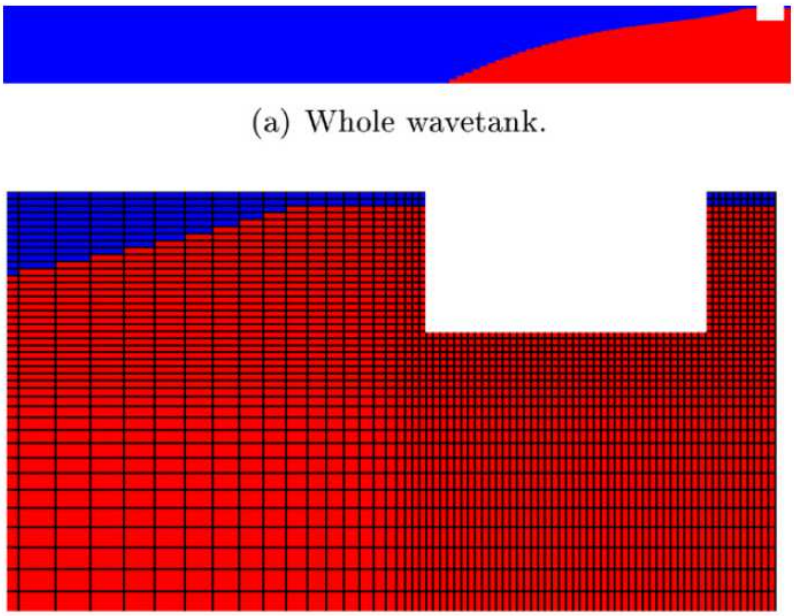

(a) Whole wavetank.

(b) Zoom around structure.

Figure 16 - Numerical fluid domain decomposition (Kristiansen et al. 2011)

Kristiansen applied his hybrid scheme on various geometries of the moonpool inlet. He then compared his results with model tests. One of the resulting response plots can be seen in Figure 17.

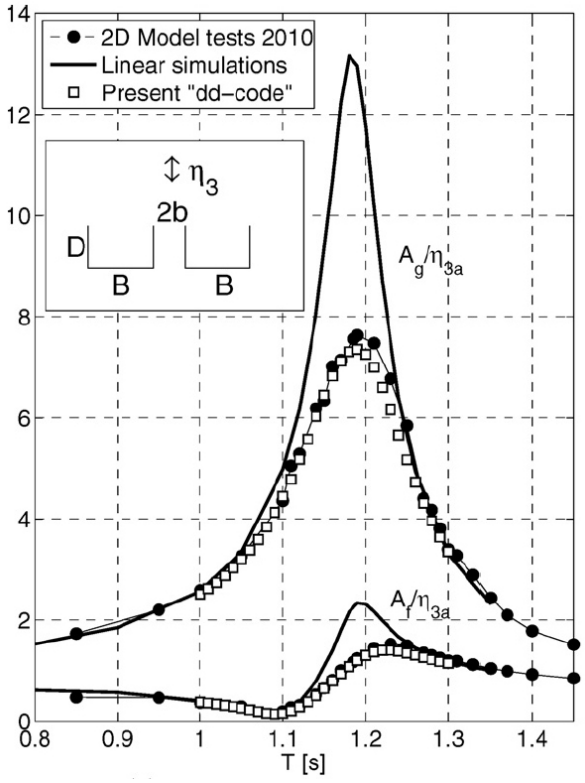

Figure 17 - Non-dimensional response amplitude (Kristiansen et al. 2011)

In this figure the amplitude ratio of the moonpool elevation, A_g/η_{3a} is plotted. The lower curve, A_f/η_{3a}, is the wave elevation outside the moonpool. Results from Kristiansen's hybrid code, a conventional linear potential code and experiments are included. As usual, potential theory over-predicts the elevation especially at periods close to resonance. The hybrid code is however almost spot on. Some minor discrepancies are found, but this is partly assumed to be an effect of wave reflections from a poorly adjusted wave beach.

Other inlet geometries were tested as well. Figure 18 shows the results from a moonpool with damping plates. The rest of the parameters, including the forcing amplitude, are the same.

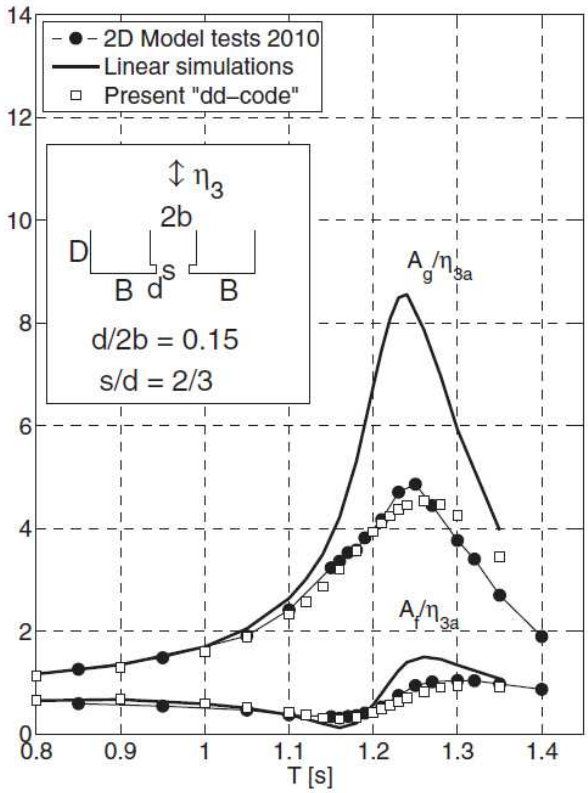

Figure 18 - Non-dimensional response amplitude (Kristiansen et al. 2011)

The same trends can be seen here; potential theory overestimates the response while the hybrid code coincides very well with the experiments. Additionally, it is very interesting to compare the results for these two geometries. The response amplitude of the moonpool with the damping plates are considerably lower than the for the moonpool without any appendages. The natural period is also higher.

Research on hydrodynamic coefficients of objects in moonpool

Morison's equation, as previously described in this section, is frequently proposed as a tool for determining the hydrodynamic forces on an object in a moonpool, i.e. the total force is a sum of drag and added mass forces. Both these contributions are dependent on coefficients, one for drag and one for added mass.

Drag and added mass coefficients are thoroughly studied for basic objects such as circular or square cylinders in an unrestricted fluid domain. The fluid domain inside a moonpool is however far from unrestricted. In some ways the situation resembles that of an object inside a confined tube or channel, conditions which have been given some attention in the past, e.g. in the work by Sharma et al. (Sharma et al. 2004), although mostly for flows of low Reynolds numbers, typically lower than 10^3. For flow past a body, the Reynolds number is defined as:

$$\mathrm{Re} = \frac{VD}{\nu} \tag{38}$$

where V is the undisturbed incoming fluid velocity, D is the diameter of the object and ν is the kinematic viscosity of the fluid. In full scale moonpool situations the Reynolds number is usually in the area between 10^5 and 10^8.

For objects in a tube or channel the blockage ratio is an important parameter, defined as

$$r_{blockage} = \frac{A_{object}}{A_{channel}} \tag{39}$$

where A_{object} is the projected area of the object and $A_{channel}$ is the cross sectional area of the channel or tube (or moonpool). When the forces on objects in such confined spaces are determined using Morison's equation, correction factors based on the blockage ratio are often applied.

A comprehensive description of blockage effects for circular cylinders for the full range of Reynolds numbers has been published by M.M. Zdravkovich (Zdravkovich 2003). Zdravkovich divides the effect of blockage ratio into three classes:

Blockage ratio	Effect on flow and forces
< 0.1	Blockage effects are small and may be ignored
0.1 < 0.6	Flow is modified, corrections of coefficients are necessary
> 0.6	Flow is radically altered and correction factors are meaningless

It is an interesting observation that blockage ratios above 0.6 are considered above the limit of what can be handled by correction factors as the flow in these regimes behave completely different.

Another issue to account for in a moonpool situation is the oscillating ambient flow. Vortices are often shed from the kind of bluff bodies one would deploy through a moonpool. When the ambient flow turns, the vortices may return back to the body and affect it. The most important parameter for this effect is the Keulegan-Carpenter number, defined as:

$$KC = \frac{VT}{D} = 2\pi\frac{A}{D} \tag{40}$$

where V is the undisturbed oscillating fluid velocity amplitude, D is the diameter of the object, T is the period of the fluid oscillation and A is the amplitude of the fluid motion. The most critical KC range is from around 4 to 25 (Pettersen 2007), in which the returning vortices are assumed to be of considerable importance. For higher KC numbers the situation resembles steady flow (Faltinsen 1990). The limits of this range depend on many factors, including the shape of the object. The critical range may also be different for confined fluid domains, as the vortex shedding characteristics has been found to be dependent on the blockage ratio (Singha et al. 2010). In a moonpool situation it is not unusual to experience KC numbers in the critical range.

Madsen's experiments

As part of a moonpool research project, experiments were done by Madsen for models of three different diving bells oscillating inside a tube of varying diameter (Madsen 1980). The three diving bells can be seen in Figure 19.

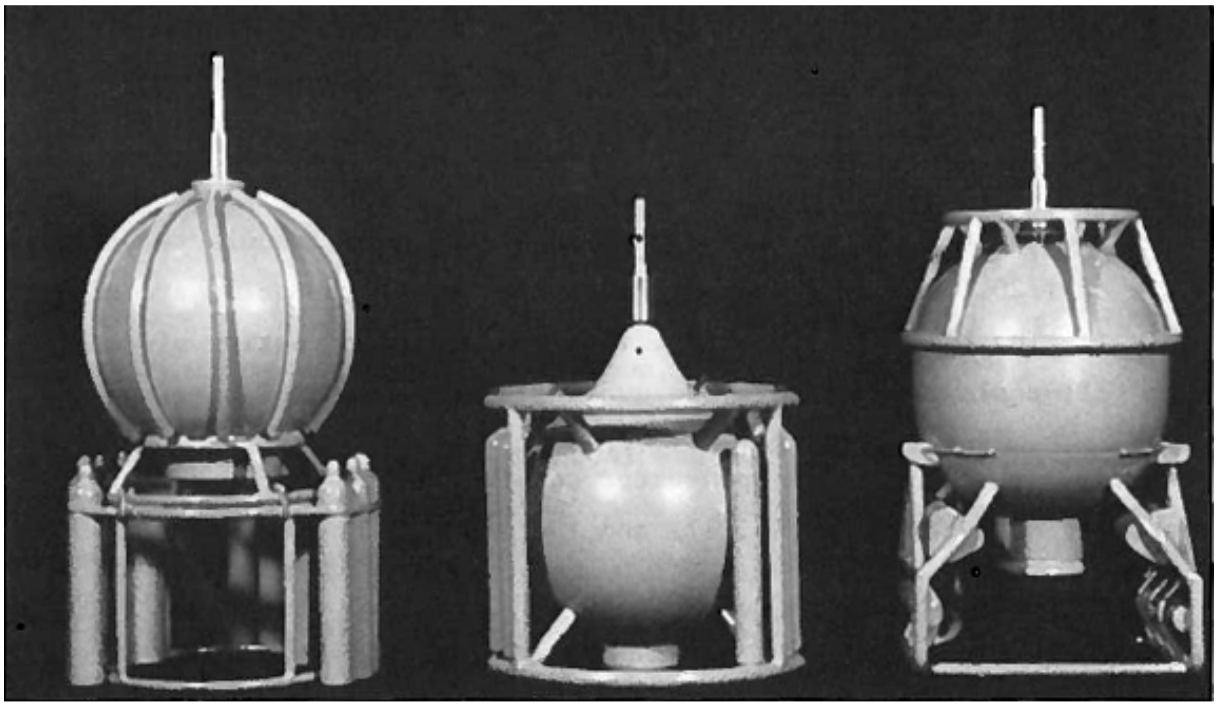

Figure 19 - Tested diving bells (Madsen 1980)

From left to right, the models are termed I, II and III. They all comprise of a sphere with different piping configurations around them. Unfortunately a clean sphere was not tested.

Madsen termed the blockage ratio (A_b/A_t) and presented his resulting correction factors as functions of this.

For the added mass coefficient, C_m, the results turned out as seen in Figure 20.

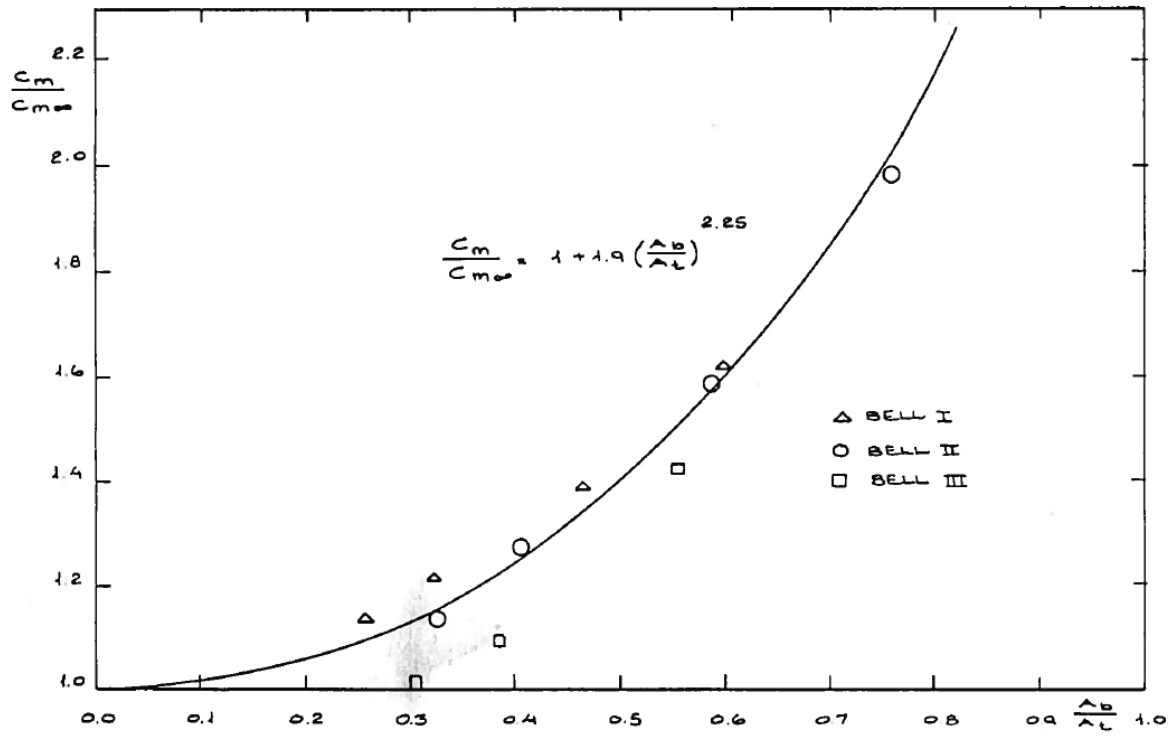

Figure 20 - Added mass plot (Madsen 1980)

The increase in the added mass coefficient seems to follow the line in the figure reasonably well. The resulting equation describing the ratio between added mass in a restricted flow and added mass in an unrestricted flow is:

$$\frac{C_M}{C_{M\infty}} = 1 + 1.9\left(\frac{A_b}{A_t}\right)^{2.25} \tag{41}$$

It should be noted that Madsen also found that C_m is dependent on the length of the tube only when A_b/A_t approaches 1.

A similar result was found for the drag coefficient. Figure 21 shows how the drag varies.

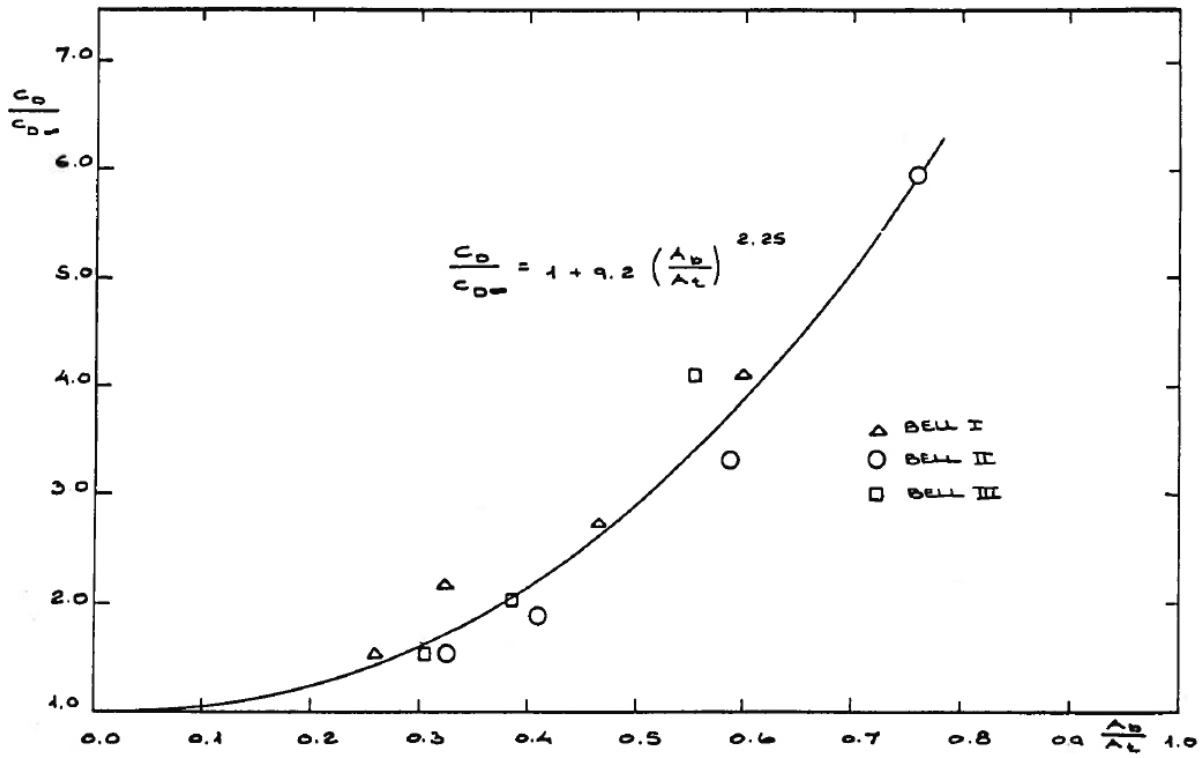

Figure 21 - Drag plot (Madsen 1980)

Here, the equation for the plotted line is:

$$\frac{C_D}{C_{D\infty}} = 1 + 9.2\left(\frac{A_b}{A_t}\right)^{2.25} \tag{42}$$

Madsen also discovered that the drag coefficient was practically independent of the velocity magnitude.

Based on these experiments the two proposed equations for drag and added mass seem to be quite good. It should be noted that both drag and added mass coefficients are dependent on the blockage ratio raised to the same power; 2.25. The proposed correction factors also appear to work well for blockage ratios up to 0.8, in spite of Zdravkovich's statement that 0.6 is the limit for the validity of correction factors. It may be a coincidence that Madsen got such a good fit, but it may also be that the limit is different for objects not of a perfect circular shape.

Although the experiments seem to produce very nice results it is important to remember they are done for objects in a tube and not for objects in realistic moonpool conditions. The shortcomings of this approach will be discussed later in this section.

DNV's recommended practices for moonpool operations

For analyses and planning of offshore operations, DNV (Det Norske Veritas) provide guidelines and recommendations. In *Modelling and Analysis of Marine Operations* (DNV 2011) an entire section is dedicated to moonpool operations. Most of the section is devoted to a so-called simplified analysis, while a more advanced approach is outlined at the end of the section. Both methods will be presented here.

Simplified analysis

The methodology described here is based on the following assumptions:

- The dimensions of the moonpool are small compared to the breadth of the ship.
- Only vertical forces and motions of the water and the object in the moonpool are considered, i.e. only the piston mode is taken into account.
- The blocking effect of objects in the moonpool is moderate.

The governing equation of motion for the water and the body inside the moonpool is given as:

$$(M + A_{33})\ddot{\zeta} + C_S \,|\dot{\zeta} - \dot{\zeta}_S\,|(\dot{\zeta} - \dot{\zeta}_S) + C_B \,|\dot{\zeta} - \dot{\zeta}_B\,|(\dot{\zeta} - \dot{\zeta}_B) + K\zeta = F(t) \qquad (43)$$

where M is the mass of the water inside the moonpool, A_{33} is the added mass of the water plug, ζ is the vertical motion of the water plug, ζ_S is the heave motion of the ship, ζ_B is the vertical motion of the body in the moonpool, C_S is the damping coefficient for the relative motion between the water and the ship, C_B is the damping coefficient for the relative motion between the water and the body, K is the water plane stiffness and F(t) is the wave excitation force on the water plug. Figure 22 shows the model.

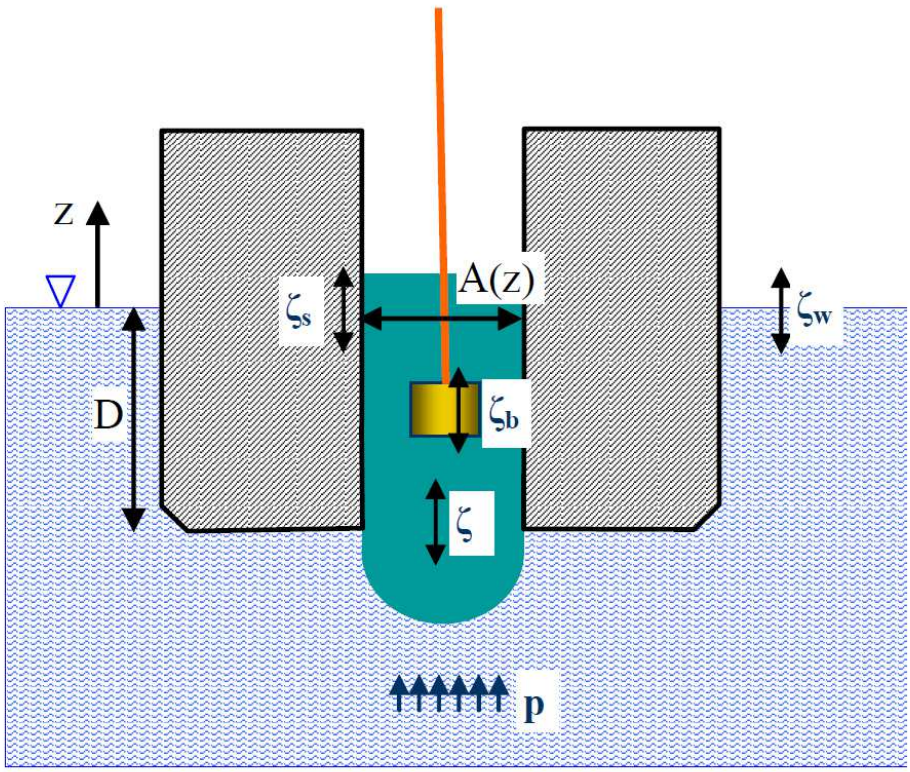

Figure 22 - Simplified moonpool model (DNV 2011)

This is a simplified form of the equations derived by Aalbers and Madsen as described earlier. The equation recommended by DNV makes the following simplifications:

- The volume of the moving water inside the moonpool is constant.
- The inertia term from Morison's equation is not included in the equation for determining the fluid motion in the moonpool.
- There is no linear damping coefficient between the motion of the water and the motion of the ship, only quadratic damping is taken into account.
- The added mass and damping of the absolute motion of the ship is not considered.

The last simplification implies that the moonpool motions do not affect the motions of the ship. This may be reasonable as it is already assumed that the moonpool is small compared to the ship.

DNV recommends using normal linear transfer functions for the motions of the vessel as is normal practice for a wide range of modelling situations. Also, for the external forces acting on the water in the moonpool the use of transfer functions are suggested. The transfer functions for the forces will then be on the form:

$$G_W = \frac{F(t)}{\zeta_W} \tag{44}$$

where G_W is the transfer function and ζ_W is the surface elevation of the incoming undisturbed wave. For the simplified approach DNV models the total force as a sum of the force from the undisturbed wave (Froude-Krylov-force) and the force from the ship motion (diffraction force). The force can be evaluated at the moonpool inlet and will be:

$$F(t) = F_{FK}(t) + F_{Diffraction}(t) = p_{FK}A + A_{33}\ddot{\zeta}_S = \rho A\zeta_W(ge^{-kD} - \omega^2\kappa\sqrt{A}G_S) \tag{45}$$

where p_{FK} is the Froude-Krylov-pressure, g is the gravitational constant, k is the wave number, ω is the wave frequency, G_S is the linear transfer function for the vessels heave at the moonpool position and κ is a constant that can be set between 0.45 and 0.47 for rectangular moonpools and 0.48 for circular moonpools. κ relates to Molin's research (Molin 2001) as previously discussed in this section.

In this equation it is implied that the added mass of the water plug is given as

$$A_{33} = \rho A\kappa\sqrt{A} \tag{46}$$

which, if κ is set to 0.45, is the same as Madsen recommends (Madsen 1980).

An equation for the resonance period of the moonpool is derived from continuity and energy conservation. For a moonpool with a varying cross section area A the resonance period can be taken as (DNV 2011):

$$T_0 = \frac{2\pi}{g}\sqrt{\int_{z=-D}^{0}\frac{A(0)}{A(z)}dz + \frac{A(0)}{A(-D)}\kappa\sqrt{A(-D)}} \tag{47}$$

where T_0 is the resonance period, g is the gravitational constant, z is the vertical axis ranging from –D at the bottom of the moonpool to 0 at the free surface, A(z) is the varying cross sectional area of the moonpool, A(0) is the area at the surface and A(-D) is the area at the inlet. If the moonpool has a constant cross section the equation reduces to

$$T_0 = \frac{2\pi}{\sqrt{g}}\sqrt{D + \kappa\sqrt{A}} \tag{48}$$

which can be directly related to the equation found by Molin (Molin 2001).

The non-linear damping of the water motions inside the moonpool can be quite large and as shown elsewhere it is of vital importance. DNV presents a crude approach for determining the non-linear damping coefficient, C_S. Using linearized theory to extract the damping from model tests, DNV recommends the following equation:

$$C_S = \frac{3\pi}{8} \bullet \omega\zeta_0 \bullet 2\eta\sqrt{KM} \quad ` \tag{49}$$

where ω is the angular frequency of the motion, ζ_0 is the amplitude of the relative motion, η is the linearized damping ratio, K is the water plane stiffness and M is the mass of the water inside the moonpool including the added mass. η is called relative damping and varies from 0.08 to 0.45 depending on the damping devices installed. A list of typical values for the relative damping for different moonpool designs is included, but the selection of η does involve a certain level of guessing.

To illustrate the effect of different damping levels, DNV includes a figure with RAO's (response amplitude operators) for the relative moonpool wave elevation for different damping levels. The RAO's are defined as:

$$RAO = \left|\frac{\zeta - \zeta_S}{\zeta_W}\right| = \left|\frac{\zeta}{\zeta_W} - G_S\right| \tag{50}$$

i.e. they provide the link between the relative wave elevation in the moonpool and the incoming undisturbed waves. As defined here, the transfer function for the vessel heave at the position of the moonpool, G_s, which is assumed to be known, is therefore subtracted. The subtraction of the vessel heave has been done in all included example moonpool RAO's and it is important to keep in mind that these contain also this variable.

The example RAO's can be seen in Figure 23.

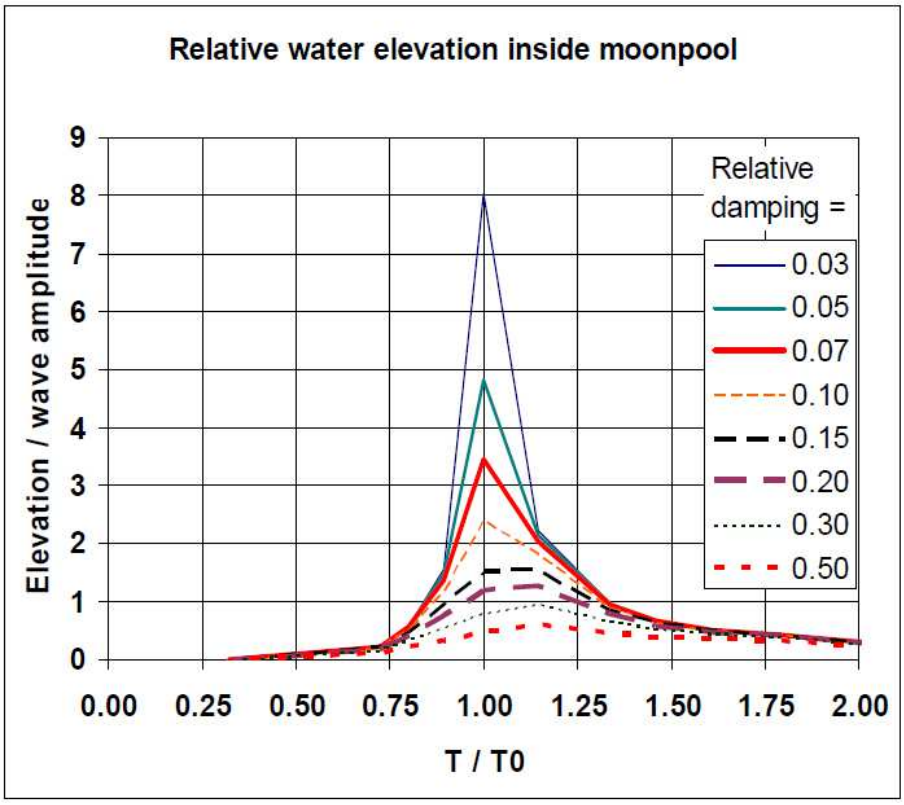

Figure 23 - Example RAO's (DNV 2011)

The figure clearly underlines the importance of a good prediction of the damping level. Even a small change can give a very different response at resonance. However, as already discussed elsewhere, determining the damping is not straight forward.

Assuming the damping level of the moonpool is determined, it is now possible to calculate an RAO for the moonpool to be analysed, and when the vessel heave RAO is subtracted the result should be similar to the examples seen in Figure 23. With an RAO there is also an associated phase angle, but this is not given much attention in the guidelines.

For calculation of forces on objects inside the moonpool, the method assumes "small-body" forces. This implies that the total force can be described by a combination of inertia and drag forces, i.e. Morison's equation is applicable. To account for the confined space inside the moonpool, DNV provides a simple relationship between the added mass coefficient for an unlimited fluid domain and a confined domain and a similar relationship for the drag coefficient (DNV 2011):

$$\frac{C_A}{C_{A0}} = 1 + 1.9\left(\frac{A_b}{A}\right)^{9/4}$$

$$\frac{C_D}{C_{D0}} = \frac{1 - 0.5A_b / A}{(1 - A_b / A)^2} \tag{51}$$

where C_A and C_{A0} are the added mass coefficients for confined and unlimited fluid domain, C_D and C_{D0} are the corresponding drag coefficients, A_b is the projected area of the body and A is the cross-sectional area of the moonpool.

The formula for the added mass coefficient is identical to what Madsen found in his experiments (Madsen 1980) as described earlier. However, the drag formula provided by DNV does not match Madsen's results. For comparison, the two formulas have been plotted in Figure 24 for a blockage ratio from 0 to 0.8.

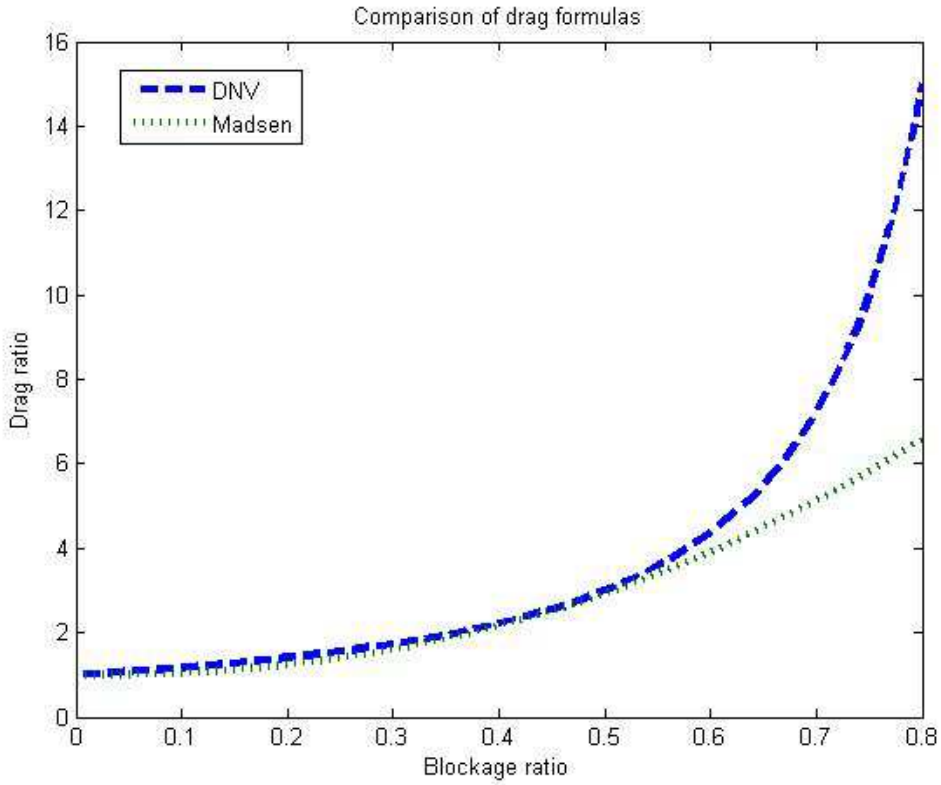

Figure 24 - Comparison of drag formulas

The two formulas give almost identical results for small blockage ratios, but from around a blockage ratio of 0.5 DNV's formula produces a much higher drag than Madsen's formula. The fact that Madsen got experimental results very close to his formula for a blockage ratio of almost 0.8 makes DNV's formula questionable (especially as it is implied that it can be used for a blockage ratio up to 0.8, where it is more than twice as big as Madsen's formula).

Comprehensive calculation method

If the object covers more than 80% of the moonpool area or if the lifted object is not rigidly connected to the vessel, DNV recommends a more comprehensive calculation method.

The first step in this method is to find transfer functions for the excitation force at the moonpool inlet. These should be found using a diffraction theory program with a panel model, and not from the scheme used in the simplified method.

Secondly, the operation should be modelled in time-domain, including non-linear effects. However, the fluid in the moonpool is still only seen as an oscillating water plug with no horizontal motions.

DNV emphasizes that the non-linear damping of the moonpool elevation should be included, but they do not give any further recommendations for determining the damping coefficient. As previously discussed, only CFD-based schemes can numerically predict a realistic fluid motion in a moonpool. Still, DNV states that

> "The use of Computational Fluid Dynamics (CFD) may not be recommended for moonpool dynamics. Even though CFD can analyse the fluid dynamic interaction between the lifted object and the water plug inside the moonpool, it is difficult to couple with the dynamic characteristics of ship in waves and the response of the lifting system. Force predictions may hence be uncertain."

Shortcomings in the knowledge of moonpools

In the past, most effort has been put into examining the fluid motions inside an empty moonpool. It has been showed many times that relatively simple numerical schemes based on potential theory are able to predict the resonance period with acceptable accuracy and the equation DNV proposes for this seems reasonable. However, the amplitude of the response is much harder to predict unless model tests or very computationally demanding numerical schemes are applied. DNV provides generic RAO's to select from, but this involves some level of guesswork and is a questionable approach, especially because even small changes in the non-linear damping have a very large impact on the fluid motions near resonance. There is definitely need for a tool which is able to predict the wave elevation without being as complicated as a full CFD scheme. Kristiansen's hybrid code could possibly be a solution, but it is still in the development stage.

For determining the forces on objects in a moonpool, there is a large gap in the knowledge concerning the interaction between the fluid motion and the forces on the objects. The underlying assumptions in previous work are:

- The flow does not change its characteristics to a significant extent when an object is positioned inside the moonpool.
- The forces acting on the object can be found using Morison's equation with correction factors based on blockage ratio (as for a flow in a confined channel).

These are bold assumptions. Consider the following: The water plug in a moonpool oscillates in the vertical direction. It has a finite amount of energy. When an object is placed in the moonpool, the fluid will exert a force on it. This will reduce the total energy of the fluid, which again will reduce the total force on the object etc. This is an iterative process, and although its exact behaviour is basically unknown, it is obvious that the first assumption (that the presence of the object does not alter the flow characteristics) is not absolutely correct. The question is not whether the flow is altered or not, the question is how much it is altered and how much the changes affect the force calculations.

The current model tests described in the rest of this thesis aims to quantify the magnitude of the forces exerted on objects in a moonpool and to identify how the presence of the object affects the ambient flow. It is also of great interest to compare the results from the model tests with estimates based on the simplified methods outlined by DNV which are based on the assumptions discussed above.

3. Experimental set-up

The experiments described in this thesis have been performed at MARINTEK in April 2013. In order to simulate a two dimensional moonpool, two rigidly connected and partially submerged rectangular bodies have been used as seen on Figure 25.

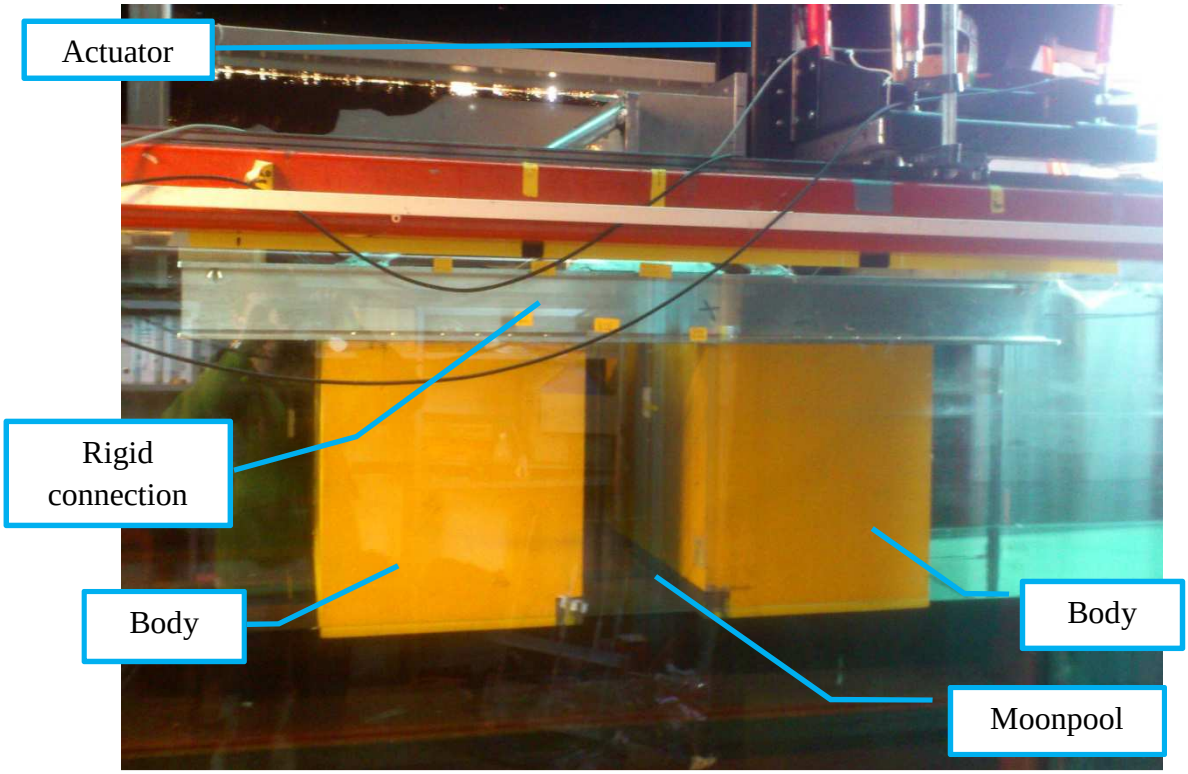

Figure 25 - Replication of Kristiansen's set-up

Replication of Kristiansen's set-up

The first part of the experiments was devoted to recreating one of the set-ups used by Kristiansen for the validation of his numerical results (Kristiansen et al. 2011). This set-up comprised of an empty moonpool with a sharp inlet and a constant cross section and is referred to as "base case" throughout the thesis. With reference to Figure 26, the main dimensions for this part were as follows:

Breadth B: 36cm
Breadth at inlet b: 18cm
Draught D: 18cm
Water depth h: 103cm

The horizontal dimensions of the tank itself were 0.6m x 13.7m.

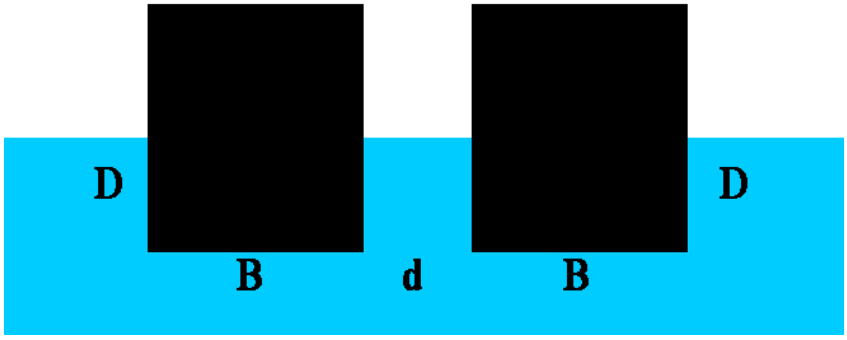

Figure 26 - Main dimensions

Forced harmonic heave motion of the moonpool was the only source of excitation. To achieve this, the model was connected to an actuator controlled by a computer. The only necessary input was the vertical zero level and the amplitude and period of the motion. However, the actuator did not produce the exact prescribed amplitudes. Therefore a displacement gauge was mounted on the model in order to record the actual heave motions.

Six wave probes were used to record the wave elevation inside the moonpool and two were mounted on the outside, 0.7m to the side of each body. The arrangement of the wave probes is illustrated as viewed from above in Figure 27. Kristiansen used an additional wave probe inside the moonpool, but in this case only eight channels were available and the six internal wave probes were assumed to be sufficient.

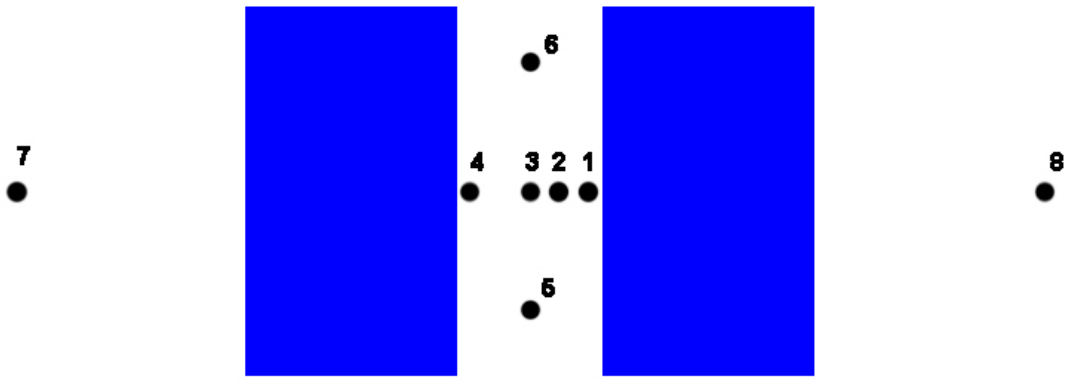

Figure 27 - Wave probe arrangement

Wave beaches were installed at the two ends of the tank. This was necessary in order to minimize wave reflections. Reflecting waves are often problematic in 2-dimensional experiments like this because the waves do not radiate their energy in the same manner as 3-dimensional short-crested waves. Wave beaches usually work by forcing the waves to break. However, many of the waves produced in these experiments had very small amplitudes and hence did not break that easily. The solution, as discovered by Kristiansen, was to position the top end of the beaches just below the surface. This made the waves roll over the beach and get “trapped” on the other side. This turned out to be quite effective.

Seven Viking-model

The same basic set-up was used for the *Seven Viking*-model, with some modifications. The moonpool on *Seven Viking* has rounded damping plates at the inlet and perforated walls. Figure 28 shows the model. A description of the vessel itself can be found in Appendix B.

Figure 28 - *Seven Viking*-moonpool model

The main full scale dimensions of the *Seven Viking*-moonpool are:

Breadth at inlet:	7.175m
Breadth at water line:	8.39m
Draught:	6.5m

Details of the design of the inlet and the perforated walls are not included in this thesis due to confidentiality issues.

The inlet geometry was modified by exchanging the original corners of the base case model by a set of new corners. In order to keep the same dimension of the actual inlet, the distance between the two bodies which make up the model was increased to 210.5mm. The geometric scale factor of the model thus became

$$\lambda = 39.8611 \tag{52}$$

The perforated walls of the model were produced in 5mm aluminium to ensure enough stiffness. This is not according to scale and accordingly the gap between the perforated walls and the solid vessel, as seen in Figure 29, is smaller than in reality. This discrepancy might have an impact on the results, but for studying trends (which is the main point of the model tests) it matters very little.

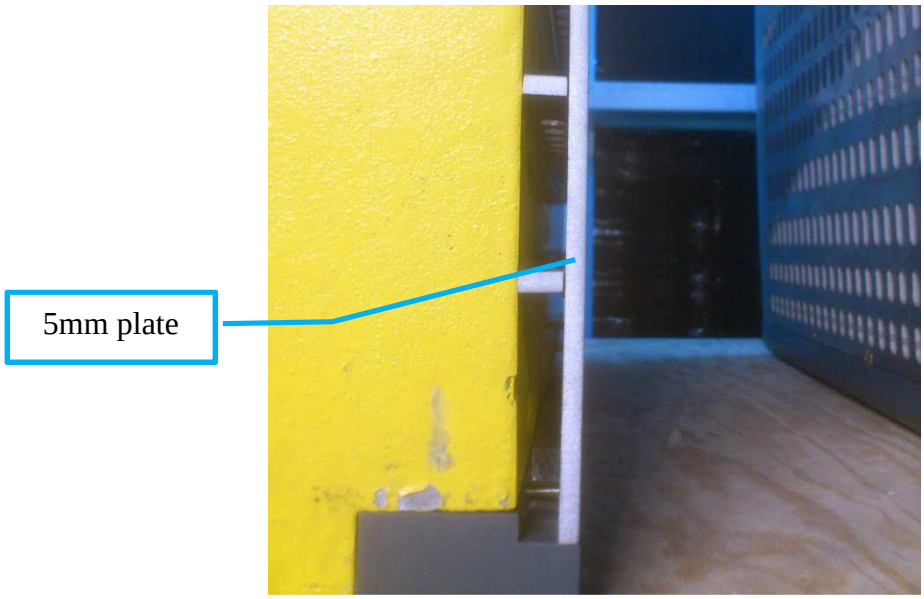

Figure 29 - Perforated walls closeup

The *Seven Viking*-model was also tested with two objects with square cross-sections inside the moonpool. The dimensions of the cross sections of the objects were 3x3m and 4x4 in full scale, which implied blockage ratios of 0.42 and 0.56 respectively. The 3x3m object is termed "small" and the 4x4m object is termed "large" throughout the rest of the thesis. In the 3-dimensional model tests carried out by Kjetil Berget, an object corresponding to the large object was tested as a validation case (with full scale dimensions of 4x4x4m).

The objects were positioned at the bottom of the moonpool, i.e. the bottoms of the objects were flush with the bottom of the moonpool and were rigidly connected to the model in two points using aluminium profiles equipped with force transducers, as seen in Figure 30.

Figure 30 - Small object in moonpool

PIV set-up

Because it was assumed that the flow inside the moonpool would have small out of plane motions it was decided that a 2-dimensional PIV set-up would be sufficient. Figure 31 shows a sketch of the set-up as seen from above.

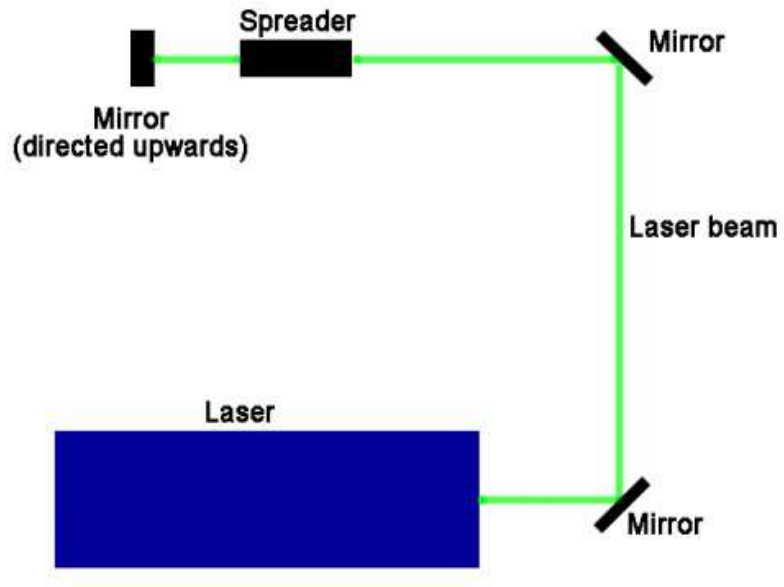

Figure 31 - PIV set-up from above

The laser beam was guided to underneath the water tank using mirrors. It was then spread into a thin sheet of light using a lens and directed upwards, so that it illuminated a cross section of the 2-dimensional moonpool close to the centre as indicated on Figure 33 and visualized in Figure 32. Great care had to be taken when adjusting the laser beam so that the light sheet would hit the right cross section of the moonpool without being tilted in any direction.

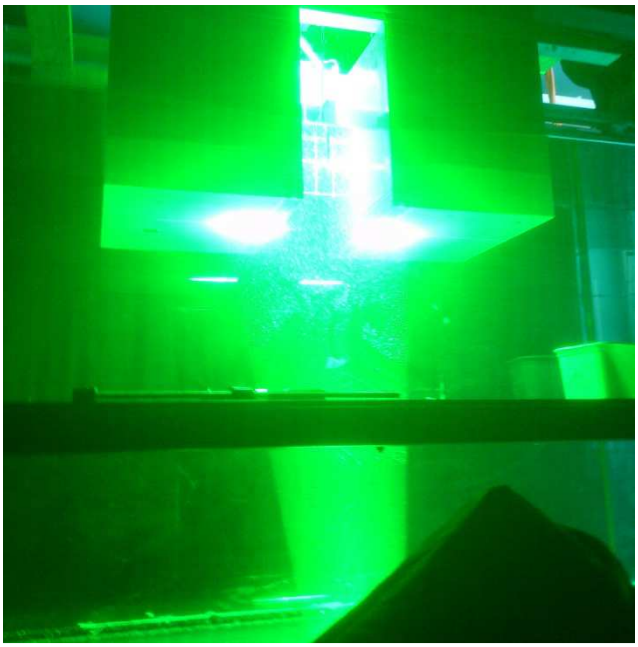

Figure 32 - PIV in use

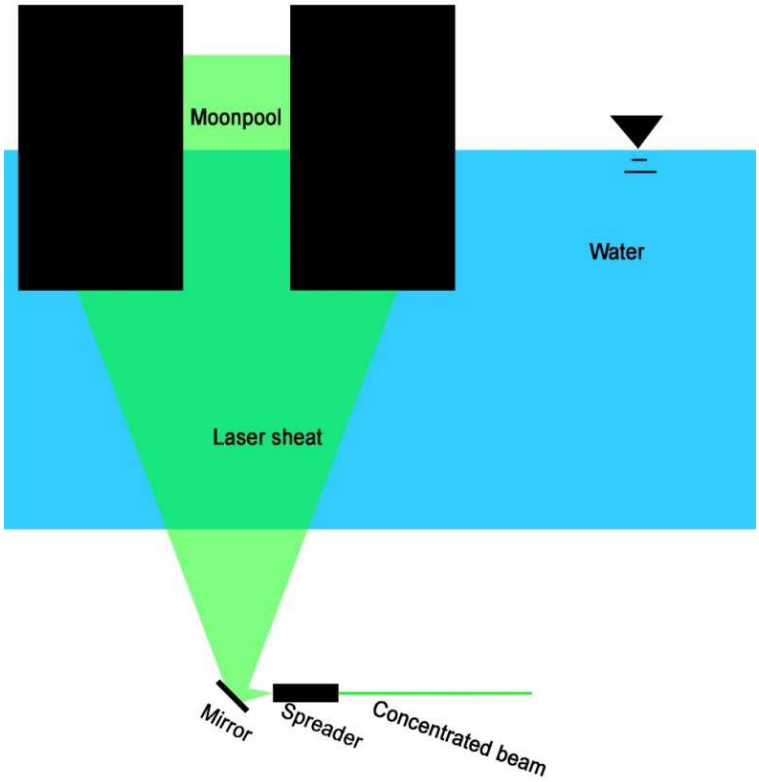

Figure 33 - PIV set-up from the side

A laser designed to emit pulses at 1kHz was used. Such a high frequency was not required for this experiment and the operating frequency was therefore set to 500Hz. This is still higher than strictly necessary, but it was not recommended to use the laser too far from its design frequency.

A high speed camera was positioned at the side of the water tank perpendicular on the light sheet. The camera had a resolution of 1024x1024 pixels. It was capable of recording time series of 8 seconds for the frequency used in the tests, corresponding to 5-6 oscillations of the moonpool.

Polyamide particles with a diameter of 80µm were selected as seeding particles after testing a few options. This seemed to work fine.

4. Analysis methods

Wave elevation transfer functions

Because all tests were performed with regular waves, producing transfer functions (RAO's) for the wave elevation inside and outside the moonpool was fairly straight forward. Everything was done in Matlab in the following order:

- Time sequences of steady wave response were selected manually from visual inspection of the time series of the wave probes. An example is shown in Figure 34 where the responses of the wave probes inside the moonpool are plotted. The red square indicates a selected time interval. Notice how steady the response is.

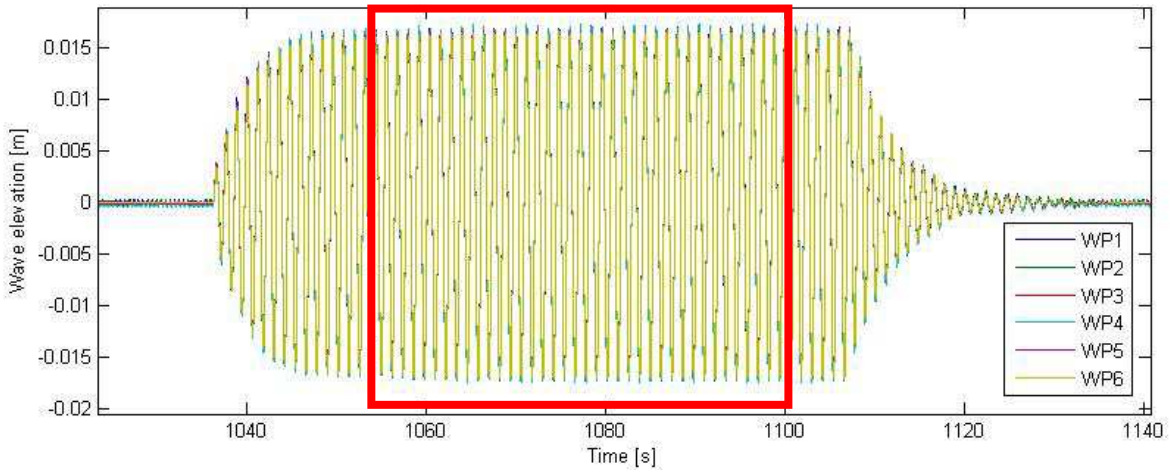

Figure 34 - Example of wave elevations in moonpool

- The six wave probes inside the moonpool were averaged, as were the two outside.
- For the first part of the tests, the motions of the model itself were subtracted from the wave motions in order to determine the absolute wave motions instead of the measured relative motions. For the second part, which involved the *Seven Viking*-model, the relative motions were used instead.
- For the selected interval, all wave maxima and displacement maxima were identified and averaged. It may sound unnecessary to find the displacement in this manner; it is after all given as input to the actuator. However, there was always a small discrepancy between the prescribed and the actual motions, illustrated by an example in Figure 35. Here, the prescribed amplitude was 100mm, but the actual amplitude is around 90mm.

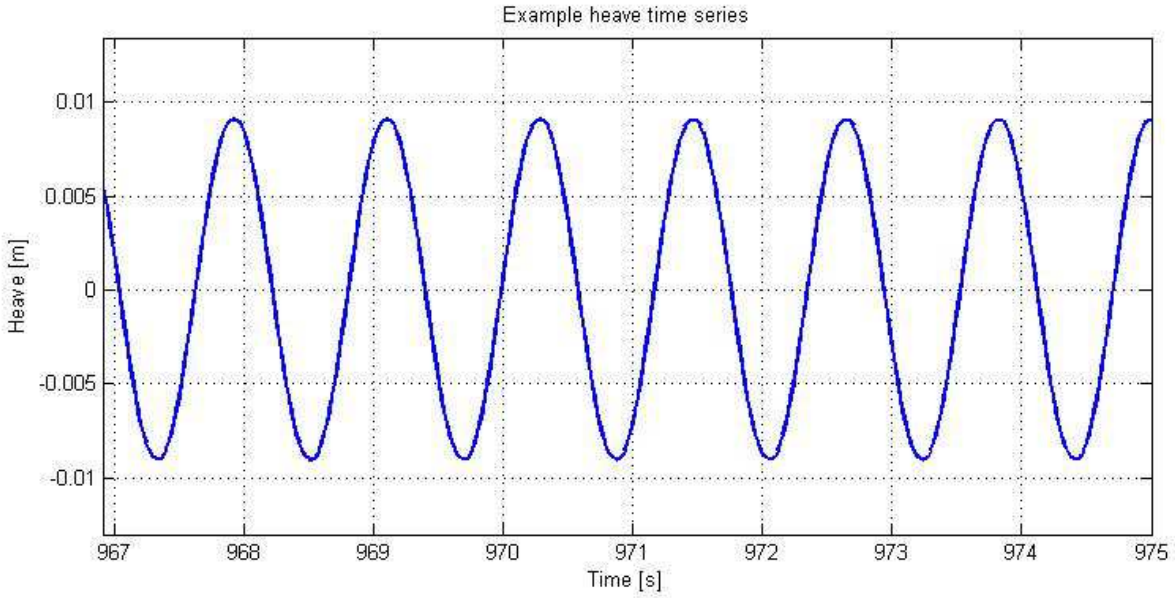

Figure 35 - Example of measured heave

- The values for the transfer functions were found by dividing the averaged maximum wave elevations by the averaged maximum heave displacements, and thus producing dimensionless RAO's on the form:

$$\text{wave elevation transfer} = \frac{\text{moonpool wave}}{\text{heave}} \tag{53}$$

Force transfer functions

The force transfer functions are defined as the force on the object divided by the moonpool wave elevation in a corresponding empty moonpool, i.e.

$$\text{force transfer} = \frac{\text{sectional force}}{\text{empty moonpool wave elevation}} \tag{54}$$

It may sound like an illogical choice at first to divide by the corresponding empty moonpool wave elevation instead of the actual wave elevation with the object. The reason for this choice is that a transfer function should connect an unknown quantity (in this case: the force) with a known quantity, and the wave elevation inside the moonpool with an object inside is usually not known. However, based on model tests, CFD or perhaps on-sight measurements, the wave elevation in an empty moonpool may be predicted.

In the 2-dimensional tests the resulting force is given as force per length, giving the force transfer functions a dimension of:

$$\frac{force\,/\,length}{length} \tag{55}$$

which, for convenience in full scale, is presented as:

$$\left[\frac{kN/m}{m}\right] \tag{56}$$

The methodology for determining the force transfer functions follows mainly the same procedure as for the wave elevation:

- The same time intervals were selected as for the wave elevations.
- The signals from the two force transducers were added together.
- Because only the hydrodynamic force was of interest, the inertia force was subtracted from the total force using the formula:

$$F_{hydrodynamic} = F_{total} - F_{inertia} = F_{total} - m_{object}a_{object} \tag{57}$$

  The acceleration of the object was assumed to be equal to the acceleration of the rest of the model, which is probably a valid assumption due to the rigid connection. The acceleration was determined by differentiating the heave time series twice.
- The resulting force signals had high-frequency components in addition to the expected heave-frequency components. These were removed using a built-in smoothing function in Matlab called "mslowless". Figure 36 shows an example of a force time series before and after the smoothing.

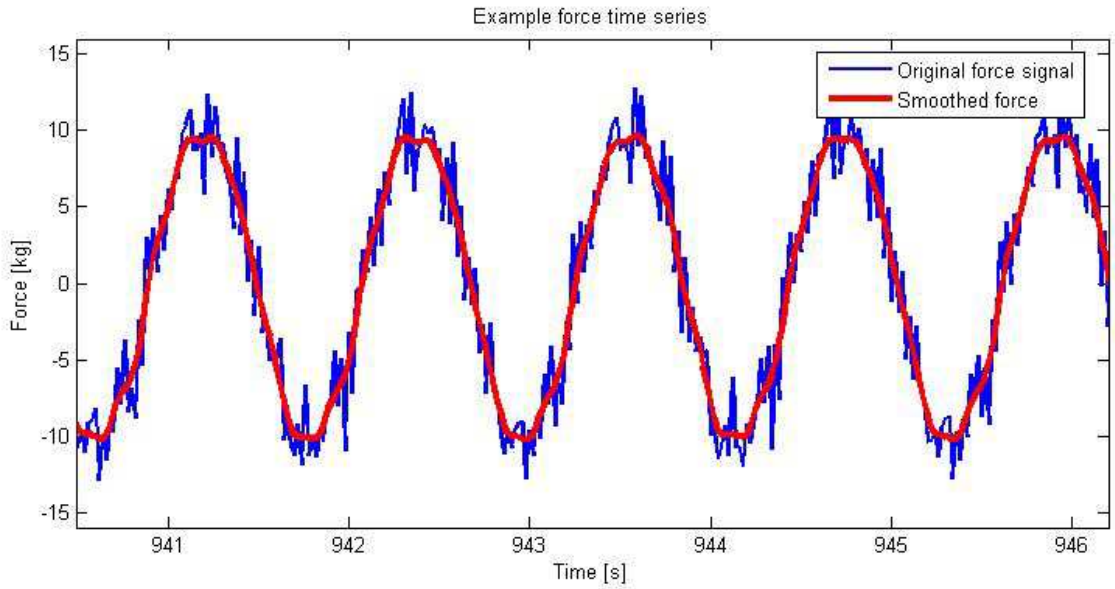

Figure 36 - Example of raw and smoothed force signal

- All the force maxima in the selected intervals were identified and averaged.
- The final force transfer functions were found by dividing the averaged force maxima by the corresponding averaged wave elevation maxima.

Force coefficients

The underlying assumption for this part is that the hydrodynamic force can be described using Morison's equation, i.e. the total force has one component proportional to acceleration (mass term) and one component proportional to velocity squared (drag term).

Simple theory of harmonic motion tells that the velocity is at its maximum when the displacement is zero (the wave elevation is between a minimum and a maximum). At this instant the acceleration is also zero. Therefore, the total force at this instant will be completely governed by the velocity-term (i.e. the drag term) and is given by:

$$F_D = \frac{1}{2}\rho A_p C_D |w| w \tag{58}$$

where ρ is the fluid density, A_p is the projected area of the object, C_D is the drag coefficient and w is the vertical fluid velocity. By rearranging, C_D can be determined from:

$$C_D = \left| \frac{F_{\text{total, zero displacement}}}{\frac{1}{2}\rho A_p (w_{\text{zero displacement}})^2} \right| \tag{59}$$

Similarly, when the acceleration and displacement is at a maximum, the velocity is zero. Therefore, at these instants, the total force will only comprise of the mass force which is given as:

$$F_D = \rho(1 + C_A) V a_z \tag{60}$$

where ρ is the fluid density, V is the volume of the object, C_A is the added mass coefficient and a_z is the vertical fluid acceleration. Again by rearranging, C_A can be found from:

$$C_A = \left| \frac{F_{\text{total, max displacement}}}{\rho V a_{\text{z, max displacement}}} \right| - 1 \tag{61}$$

The total force is found using the same approach as outlined in the methodology for the force transfer functions. The fluid velocity and acceleration is found by differentiating the wave elevation once and twice respectively.

PIV analysis

In this chapter the principles behind the particle image velocimetry technique is presented, as described by Visscher in his PhD thesis (Visscher 2011) and Adrian et al. (Adrian et al. 2011). A complete description of the background theory of PIV is beyond the scope of this thesis, but can be found in the mentioned references.

The raw output from a PIV test is a series of images of the laser-illuminated particles. Figure 37 shows an example frame from a test with the *Seven Viking*-model.

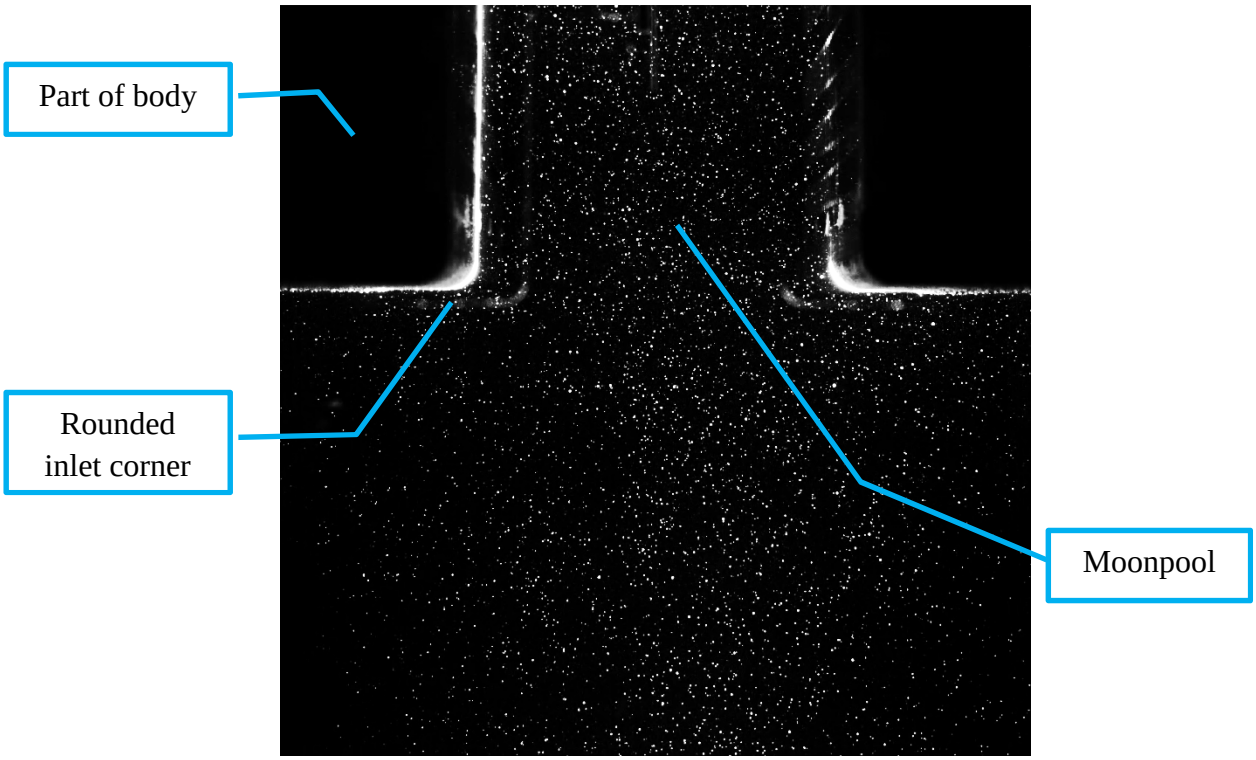

Figure 37 - PIV picture of *Seven Viking*-model

To obtain the flow velocity fields from these images a methodology based on correlation between succeeding image frames is applied. The images are divided into squares (or cells) of e.g. 16x16 pixels. It is assumed that all particles inside one cell have a uniform motion from one frame to the next. The validity of this assumption depends on how large the velocity gradient in the flow is compared to the size of the cells. In order to identify the correct motion of the particles a correlation function between two time steps is applied. The correlation function will have a peak which corresponds to the most likely motion and, ideally, this also corresponds to the true motion. This scheme is applied for all cells at all time steps.

This rather clever scheme should in theory be flawless. In reality however, there are several issues which may affect the quality of the results including:

- The image quality. The software must be able to identify the seeding particles from the background. This requires a camera with sufficient resolution and good optics, correct focus and well illuminated seeding particles.
- The particle density. Some particles will move out of the cell from one time step to another, while others may move out of plane. Therefore it is necessary to have enough particles in order to get good correlation. At the same time too many particles will make it impossible to obtain a meaningful correlation function.

- The magnitude of the particle motion from one time step to another. If the particles move too much it is difficult to trace them. On the other hand, it is important to keep in mind that a computer operates with discretized quantities and only sees the particle motions as a change in pixels. Consider as an example that the true motion from one time step to another corresponds to 0.5 pixels. Based on the discretized correlation function, the computer will probably decide that the motion is either 0 or 1 pixel, both of which are very wrong. Because of this it is important to make sure the time step is large enough to allow the particles to move a significant distance. There is a numerical scheme which partially overcomes this problem (which will be discussed later) but it is not perfect and hence should not be relied on too much.

The software *PIVview2C* was used for the PIV-analyses in these experiments. The program allows the user to create a parameter-file based on one image pair and then employ the parameters for all time steps. This was done through a batch-script in *Matlab*. The following parameters were set in the parameter-file:

- A mask was created to cover the body. Figure 38 shows the mask for the validation moonpool. Notice also the wave probes, which were not removed in this particular case, and the reflections of the laser on the tank walls.

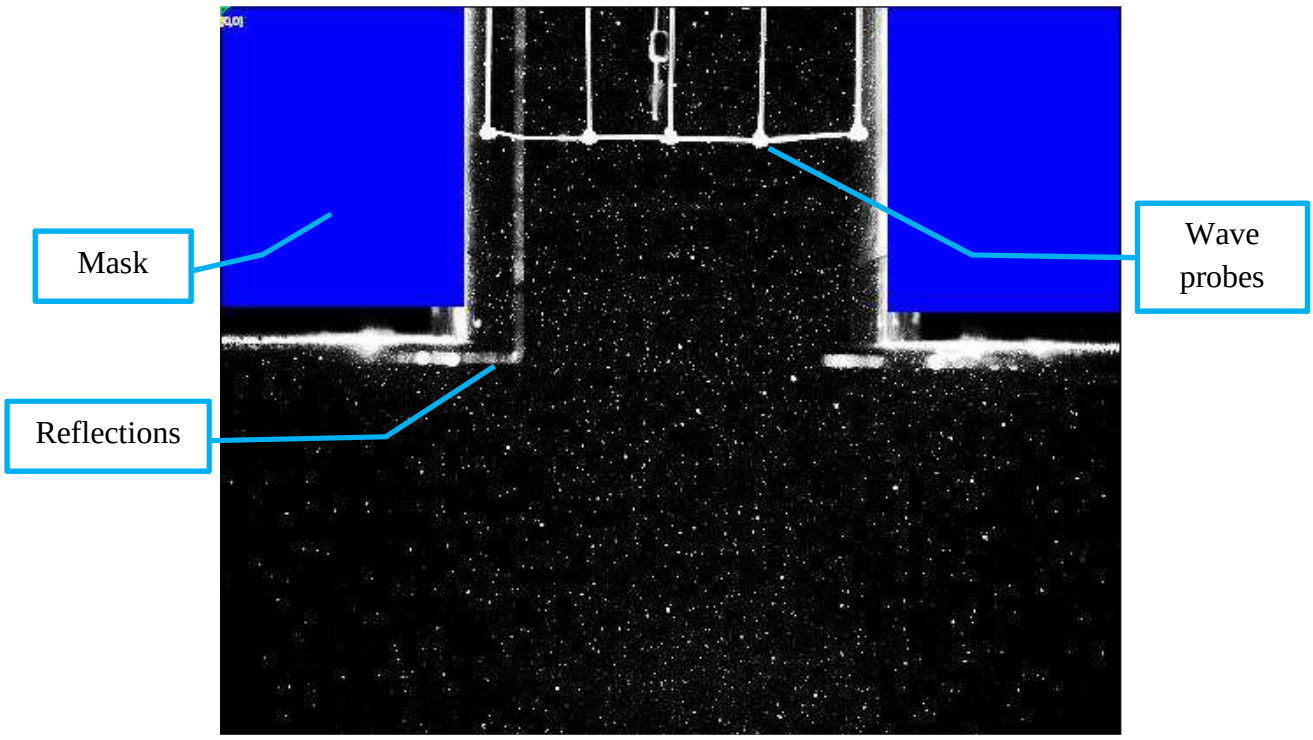

Figure 38 - PIV picture with mask

- A cell size of 16x16 pixels was selected with 50% overlap between cells.
- A multi grid refinement-scheme was selected, meaning the program evaluates every time step three times with cell sizes decreasing from 64x64 to 16x16 pixels in three steps.
- On the final refinement-step, sub-pixel image shifting was enabled. This is a numerical scheme applied on the discretized correlation functions. The functions are approximated numerically using Whittaker reconstruction, allowing the correlation peak to lie between the discretized values. B-spline interpolation of the third order was used to identify peaks.
- Two criteria for identification of outliers (vectors very different from their neighbour vectors) were used; a maximum displacement criterion set to 20px and a normalized

median test set to 3. Outliers were then tried replaced by a secondary peak in the correlation function (assuming the wrong peak had been selected in the first place) or, if that failed, interpolated from the surrounding vectors.

Correlation was performed on images taken with 8ms delay. This was found to be the best compromise for having the particles move a sufficient but not too large distance each time step.

Time-averaging over three time steps was done manually after the processing of the images, i.e. for a generic vector x_i at time step i the time-averaged vector was obtained as

$$\overline{x_i} = \frac{x_{i-1} + x_i + x_{i+1}}{3} \tag{62}$$

This led to smoother results and because of the high sampling frequency, 500Hz, it is assumed that any fluctuations cancelled out by this scheme were only the result of numerical instabilities.

Additionally, phase averaging was applied in order to cancel out random flow effects and hence to get a stronger representation of the cyclical phenomena such as the vortex formations. This averaging was done over five cycles of the motion, i.e. a generic vector x at time t was phase-averaged as:

$$x(t)_{Phase} = \frac{1}{5}\sum_{i=1}^{5} x\left(t + (i-1)T_0\right) \tag{63}$$

where T_0 is the period of oscillation. The method worked as intended, i.e. it gave a nice representation of the cyclical effects. However, it should be kept in mind that this involves manipulation of the results and it is important to be aware of what is lost in this process. This is discussed later in sections 5 and 6.

5. Results and discussion

In this section results from the various set-ups and configurations are presented and discussed. It should be noted that all forcing amplitudes are prescribed amplitudes, and not measured.

All PIV results have been acquired using the same excitation parameters; 15mm heave amplitude and 1.17s period. For the *Seven Viking*-moonpool this corresponds to 0.6m amplitude and 7.39s period in full scale. All results are phase-averaged, unless stated otherwise.

Replication of Kristiansen's set-up

For this particular part of the experiments all results are presented in model scale. All transfer functions show the absolute wave elevation, i.e. not relative to the model.

Kristiansen applied two different forcing amplitudes on his basic set-up; 2.5mm and 5mm. His resulting transfer functions are compared to those found in the current experiments in Figure 39 and Figure 40. In the figures, the solid lines are the results from potential theory, the squares are results from Kristiansen's hybrid scheme, the solid black circles are the results from the previous experiments and the red circles are from the current model tests.

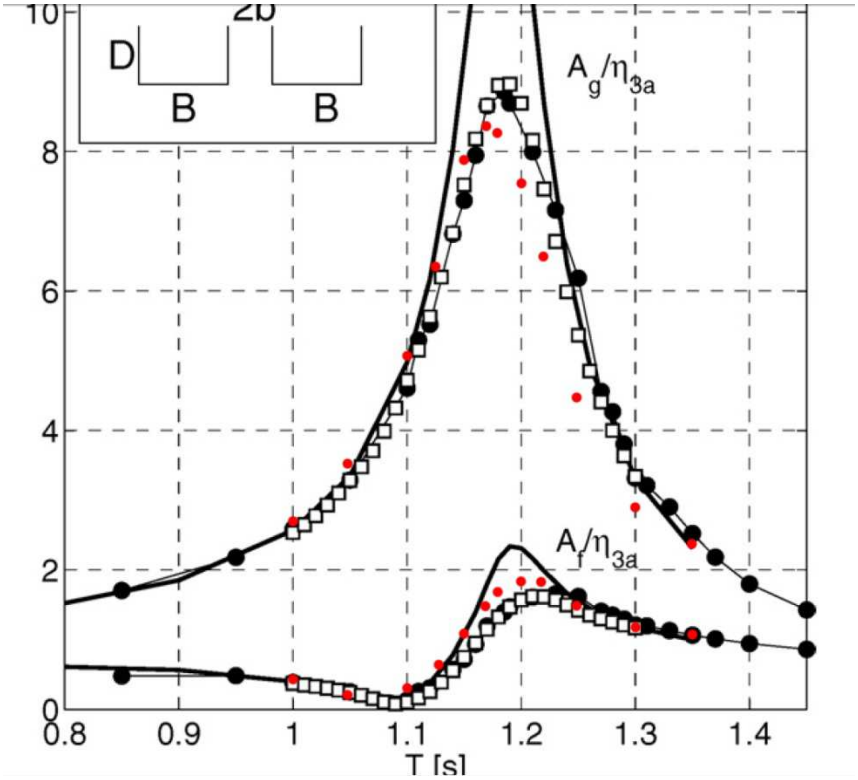

Figure 39 - Non-dimensional response amplitude 2.5mm (Kristiansen et al. 2011) Black circles: Previous model tests. Red circles: Current model tests.

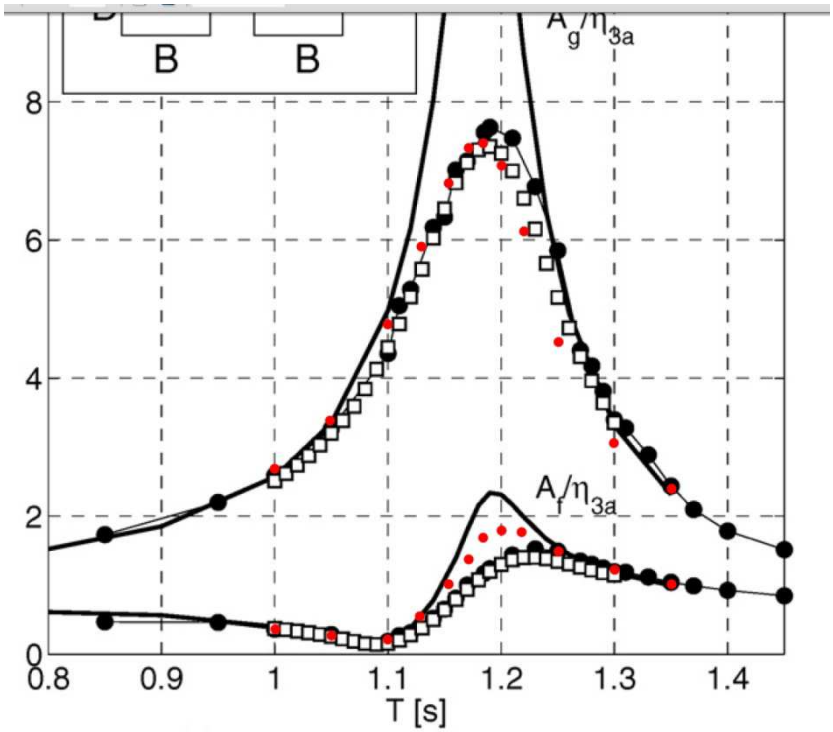

Figure 40 - Non-dimensional response amplitude 5mm (Kristiansen et al. 2011)
Black circles: Previous model tests. Red circles: Current model tests.

The results are generally satisfactory. In both cases there seem to be a small shift of the resonance period, but the discrepancy is small. The amplitudes of the plots also show an acceptable fit, especially for the wave elevations inside the moonpool. The only significant difference is the elevation outside the moonpool for 5mm excitation. The reason for this disagreement could perhaps be due to how the wave beaches were set up. Although they seemed to work fine it is hard to tell whether they were damping the waves in exactly the same manner as in Kristiansen's model tests. Another reason could be the magnitude of the heave excitation as this is very important for the response level (because of the non-linear damping). Even though the amplitude is set to e.g. 5mm, the actual amplitude is somewhat lower which again leads to a lower damping level and it is possible that the discrepancy between prescribed and actual amplitude was different in the current and in Kristiansen's experiments.

In general the current results are as close to the previous results as can be expected within reason. There are many factors present which may affect the results and it is almost impossible to reproduce experiments 100%.

Two additional excitation amplitudes were also tested; 10mm and 20mm. Figure 41 shows the transfer functions for all four cases. All four transfer functions have similar shapes, the difference lies in the magnitude, especially around resonance regions. Again, the reason for the decrease in response at higher excitation amplitudes is the non-linear damping as discussed in section 2, i.e. the damping level increases when the motions increase.

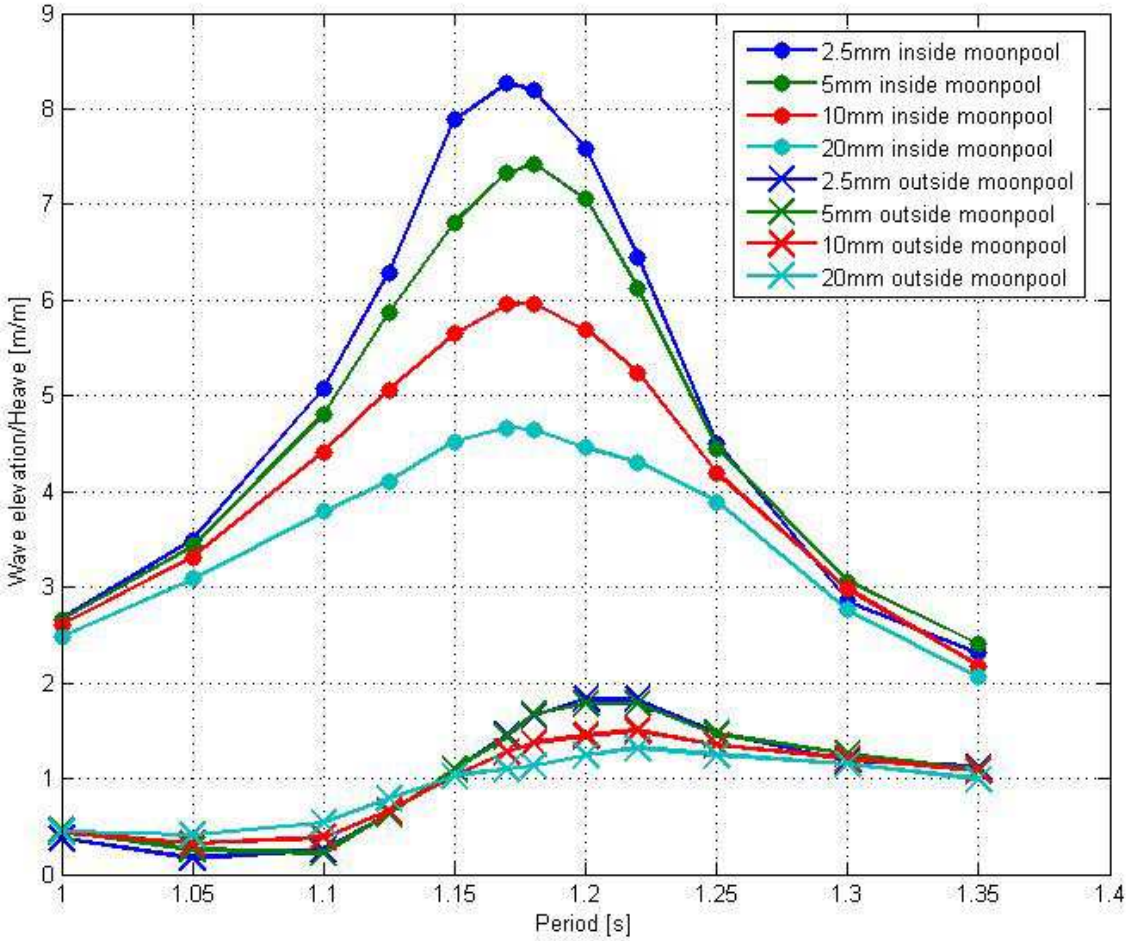

Figure 41 - Absolute wave elevation transfer functions, base case

The flow field has been visualized for one whole oscillation cycle with an excitation amplitude of 15mm and period of 1.17s. Snapshots of the whole cycle can be seen in Appendix A. One whole cycle is 360 degrees, and the start (0 degrees) is defined as the instance when the flow is at a high point inside the moonpool. An example snapshot can be seen in Figure 42. In this figure the flow is 135 degrees into the cycle, meaning it is on the way out of the moonpool and will reach a low point in 45 degrees. Notice the large vortices below and to each side of the moonpool entrance. The vortices have been separated at the inlet edges and are at this point completely free from the walls. This flow field bears a strong resemblance to that predicted by the theory of Kristiansen et al. (Kristiansen et al. 2008) which is described in section 2.

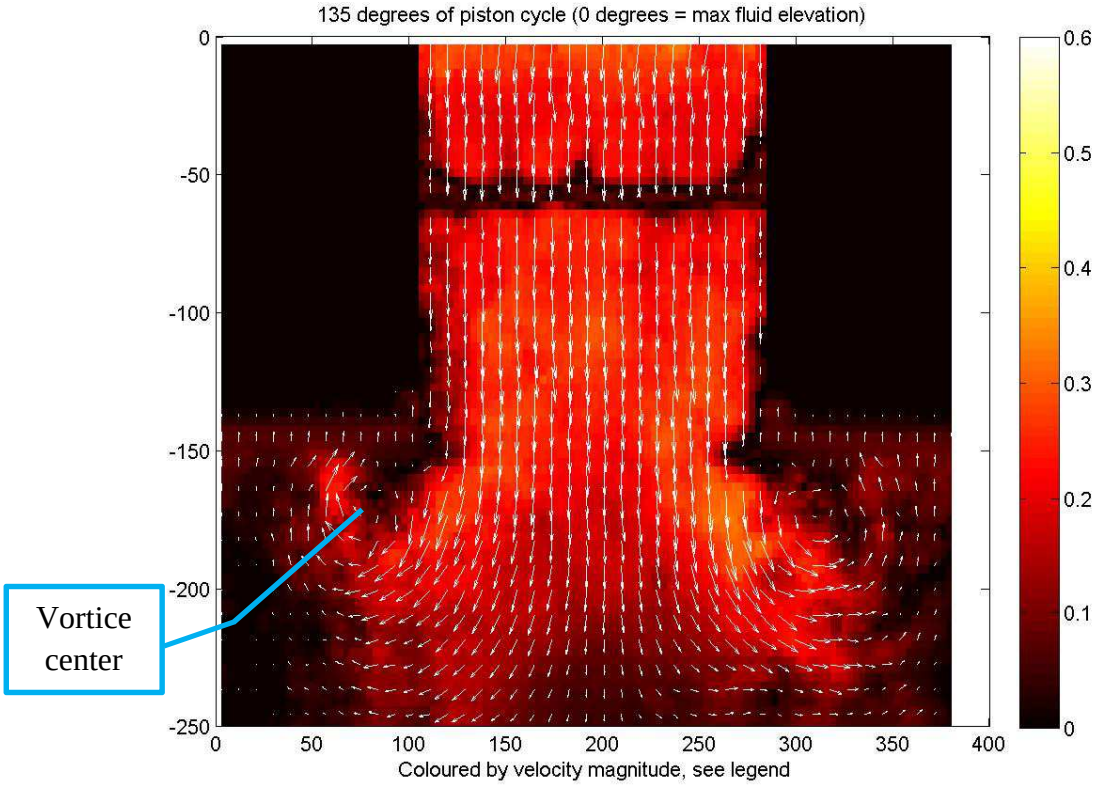

Figure 42 - PIV vectors, base case, flow out of moonpool

It appears that the vortices formed inside the moonpool when the flow enters do not reach the same strength as those formed when the flow is going out, see Figure 43. This is probably an effect of the limited size of the moonpool. Still, even though the vortices are not that apparent, there is a significant "wake zone" close to the walls of the moonpool at inflow where the motions are small which is a consequence of the vorticity induced at the corner of the inlet.

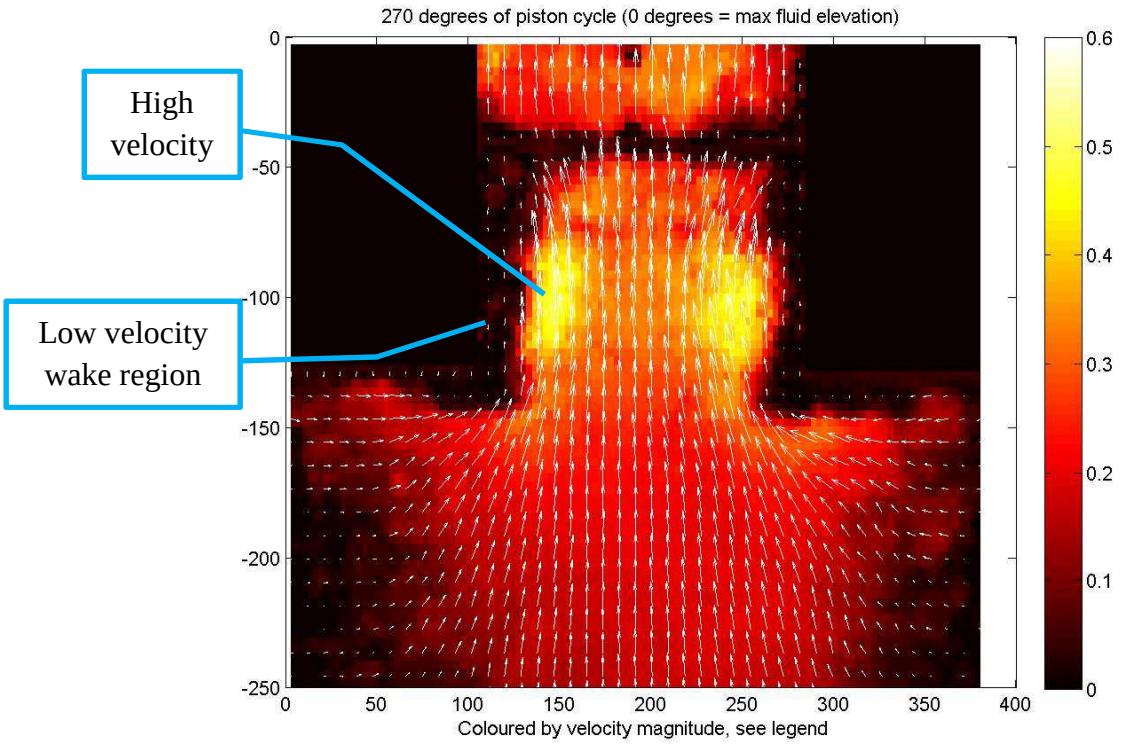

Figure 43 - PIV vectors, base case, flow into moonpool

Although the pictures from this particular case suffers somewhat from what is assumed to be a low level of seeding particles, the development of the vortices can still be seen fairly well. It is interesting to see how quickly the vortices lose their intensity after they get detached from the body, though this might partially be a result of the phase-averaging applied to these velocity fields.

Figure 44 shows vertical velocity profiles at the inlet of the moonpool over one cycle. The profiles at 0 and 180 degrees are left out in order to make the plots less chaotic. The velocities are almost zero at these instances anyway.

At first glance, the velocity profiles demonstrate how uniformly the water flows across the moonpool inlet. This is a result of the piston mode motion in which the fluid acts like a water plug oscillating in the vertical direction only. A similar result is obtained from the wave probes which measure the free surface.

However, by looking closer at the velocity profiles, it can be seen that the velocities close to (but not right next to) the moonpool walls are, most of the time, larger than the velocities in the middle. In a moonpool the fluid flows from a practically unconfined domain into a confined domain and vice versa, i.e. it experiences sudden contraction and expansion and the velocities will therefore be highest at the sharp corners of the contraction/expansion. This effect is also higher for inflow than for outflow.

On the other hand, the velocities right next to the walls (in the wake zones), especially for the inflow, are small as already discussed in connection with Figure 43.

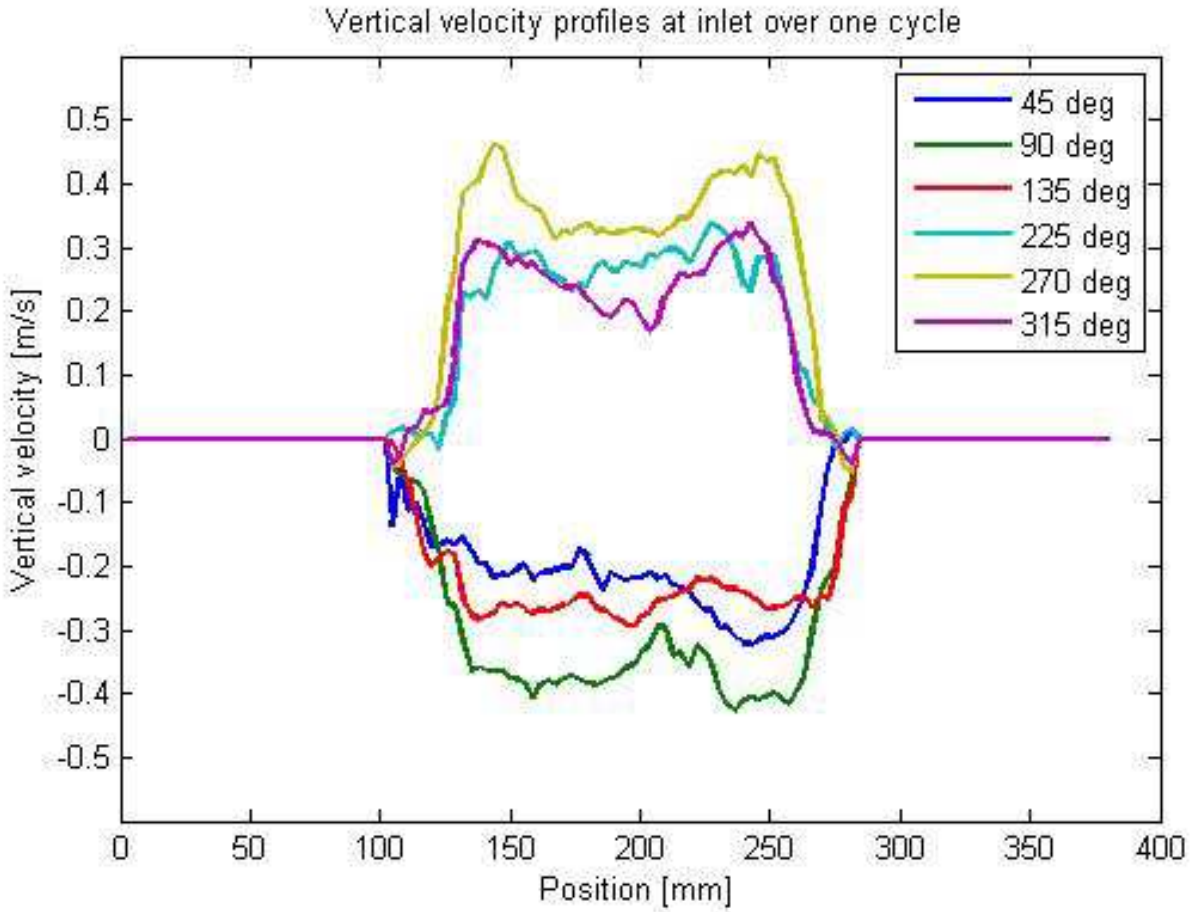

Figure 44 - PIV, base case, velocity profiles

Two final test series were performed on the basic moonpool model in which the water level was lowered to 163mm, which is the same draught as was used for the *Seven Viking*-moonpool studied in the rest of the experiments (with a scaling ratio of 39.8611). The resulting relative transfer functions, seen in Figure 45, are plotted in full scale as are all results for the *Seven Viking*-model.

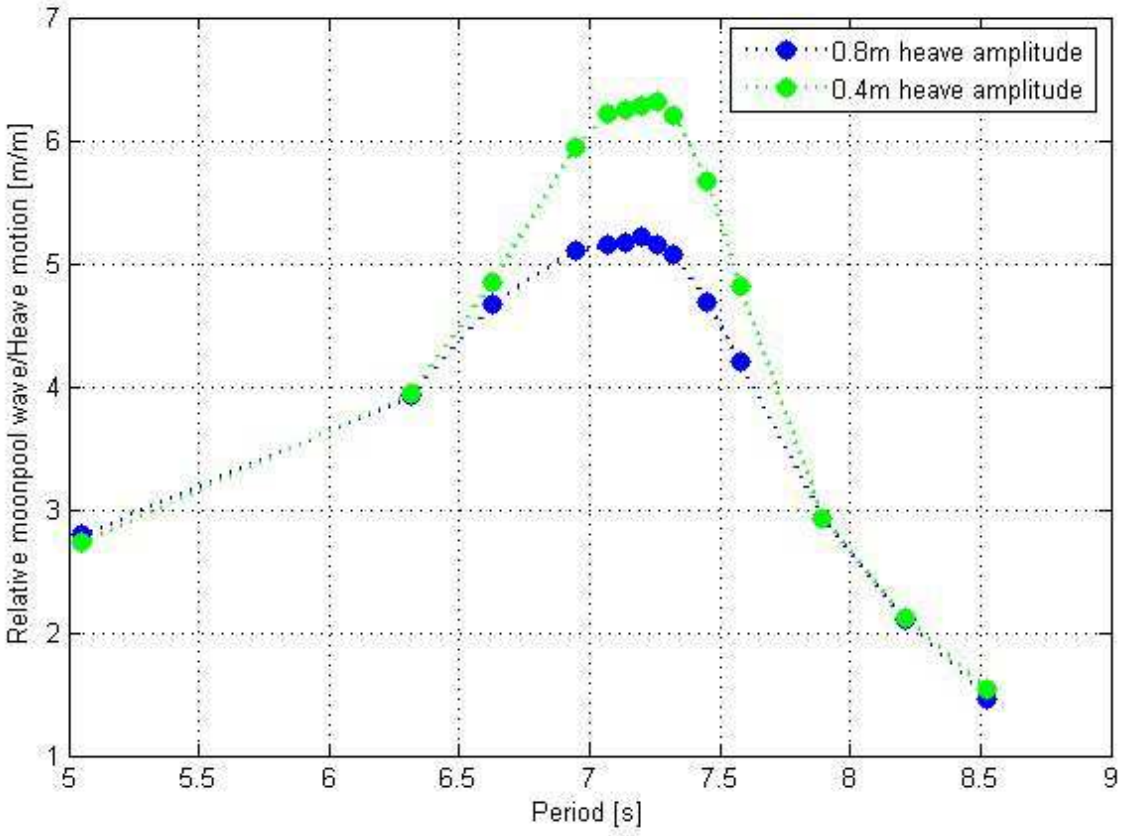

Figure 45 - Moonpool wave transfer functions, base case w/*Seven Viking* draught

The resonance period is around 7.3s in full scale and 1.16s in model scale, i.e. a bit lower than for the case with the higher water level. This is as expected according to the potential theory derived by Molin discussed in section 2.

Seven Viking-model

This case is modelled after an existing moonpool, with a scaling ratio of 39.8611. Therefore it seems natural to present the results in full scale. Furthermore, all transfer functions describe relative motions between the water and the model, i.e. the frame of reference is moving with the model. However, because of the simplified set-up the results are probably not completely representable of the real *Seven Viking*-moonpool, see section 7.

Empty moonpool

The transfer functions for the wave elevations inside the empty moonpool at all tested heave amplitudes can be seen in Figure 46.

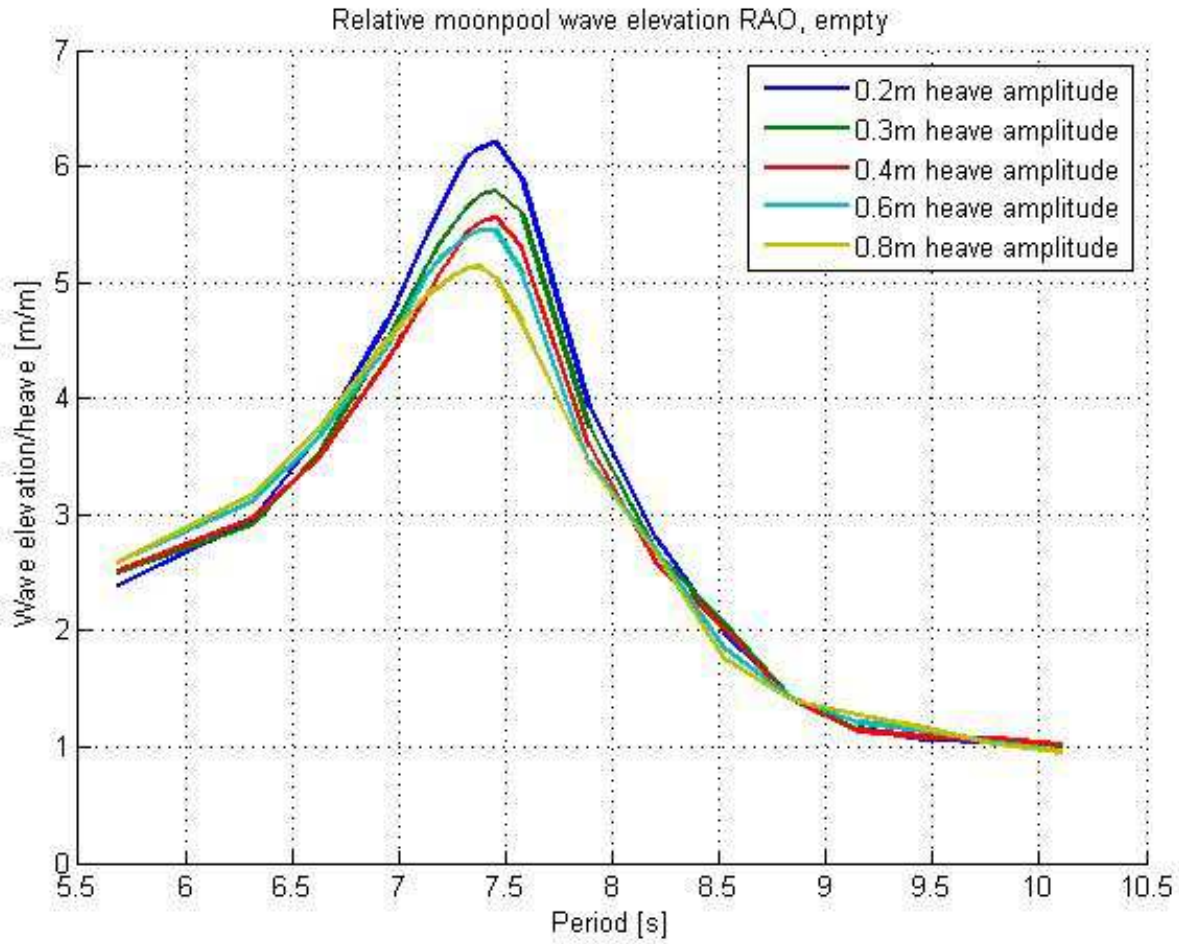

Figure 46 - Moonpool wave transfer functions, *Seven Viking* empty

The transfer functions have shapes as expected. The resonance period does not change much for different excitation amplitudes and the curves approach unity for high periods. The magnitude of the resonance peak does not decrease very much as the forcing amplitude increase, in contrast to the transfer functions seen in Figure 41 and Figure 45. This is an indication of a relatively low level of non-linear damping which can be explained by the rounded inlet edges of this particular moonpool, which are less prone to trigger vortex shedding than the sharp inlet in Kristiansen's base case. The resonance period is also slightly higher than that for the base case with the same draught as the *Seven Viking*.

The velocity fields produced with PIV show why the non-linear damping is less prominent. In Figure 47 the flow at 135 degrees into the cycle is visualized. The excitation parameters are the same as for the PIV images of the basic validation moonpool. Again, the whole cycle can be seen in Appendix A. It is evident that although there is a vortex formation at the outlet, it is smaller than for the moonpool with the sharp edges. Also, in this case the vortices do not seem to separate from the body as easily as they do for the moonpool with the sharp corners.

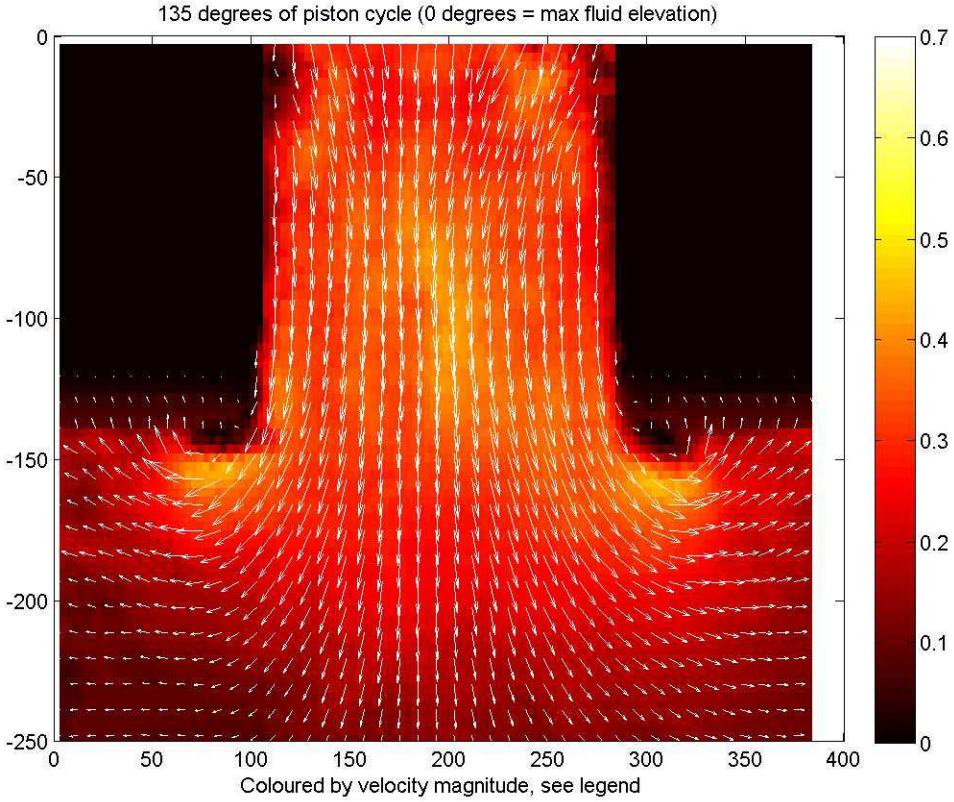

Figure 47 - PIV vectors, *Seven Viking* empty, flow out of moonpool

The difference is even larger for the inflow as seen in Figure 48. For the sharp-cornered moonpool there is a large wake region close to the moonpool walls. This effect is hardly present at all in this case except for a thin boundary layer, which is due to wall-friction. Moreover, there are little or no signs of vortices.

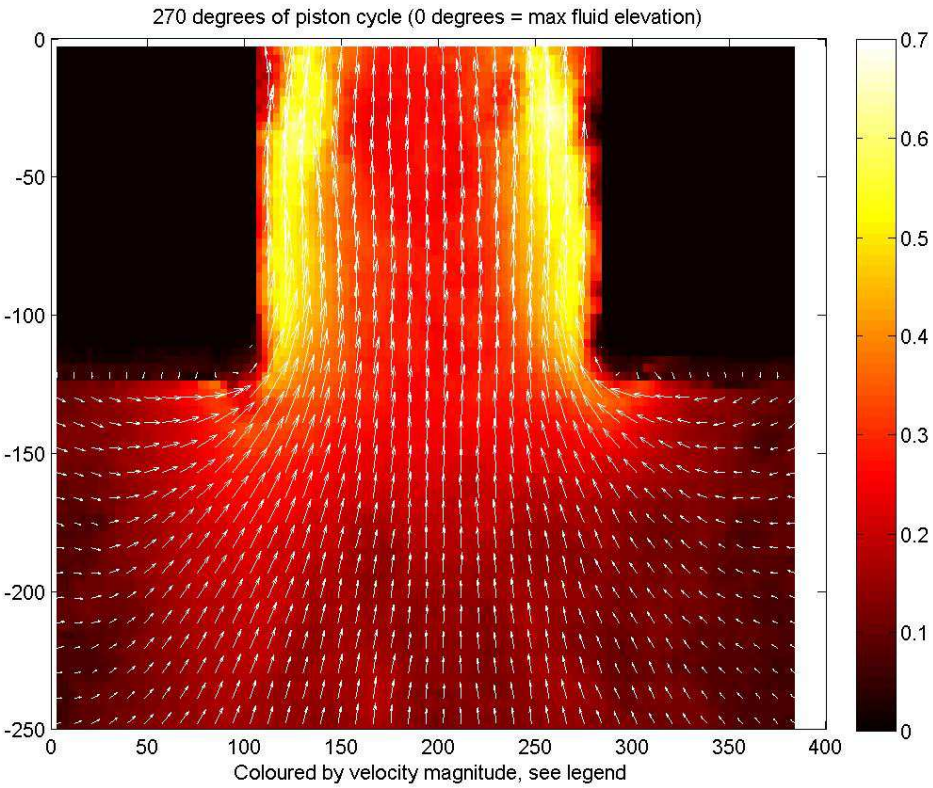

Figure 48 - PIV vectors, Seven Viking empty, flow into moonpool

It is also worth noticing how little the water seems to flow through the perforated walls. The fluid motions appears to be almost completely vertical except for close to the free surface during the outflow, where there are some signs of horizontal velocity components. The flow through the perforated walls is possibly of a random nature rather than periodic, and therefore the effect may be cancelled out to some extent by the phase-averaging. Corresponding velocity fields without phase-averaging for the empty *Seven Viking*-moonpool can be seen in Appendix A, and it is evident from these that there may be more horizontal velocities than what can be seen from the phase-averaged plots. See also section 6 for a discussion of what is lost in the phase-averaging.

The velocity profiles of the inlet, displayed in Figure 49, show that the wake zones close to the walls are much smaller here than in the base case. On the other hand, the flow in the rest of the moonpool displays a very similar behaviour for both moonpool configurations.

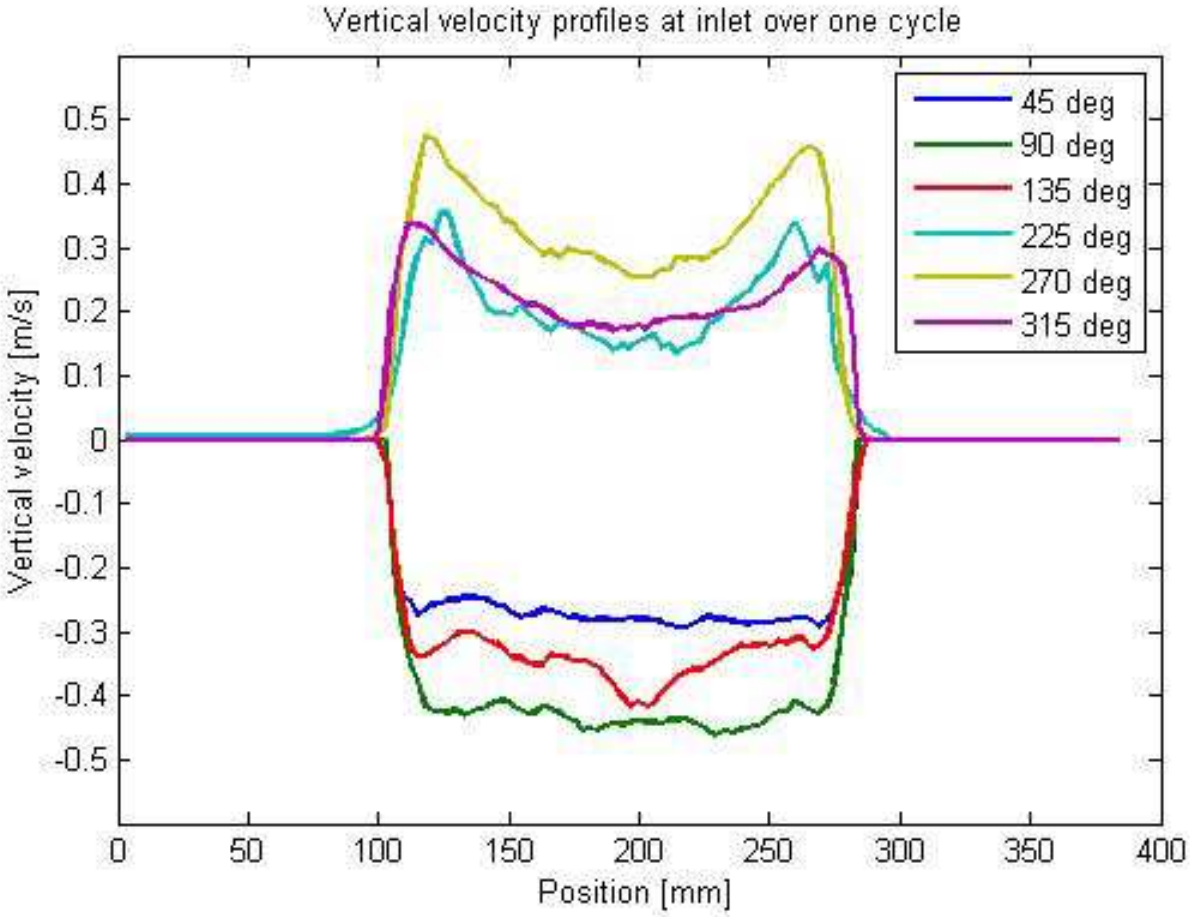

Figure 49 - PIV, *Seven Viking* empty, velocity profiles

Objects in moonpool, wave elevation

Introducing the objects in the moonpool turned out to drastically alter the transfer functions for the wave elevations. The transfer function for the small object with a blockage ratio of 0.42 can be seen in Figure 50 and for the large object with blockage ratio of 0.56 in Figure 51.

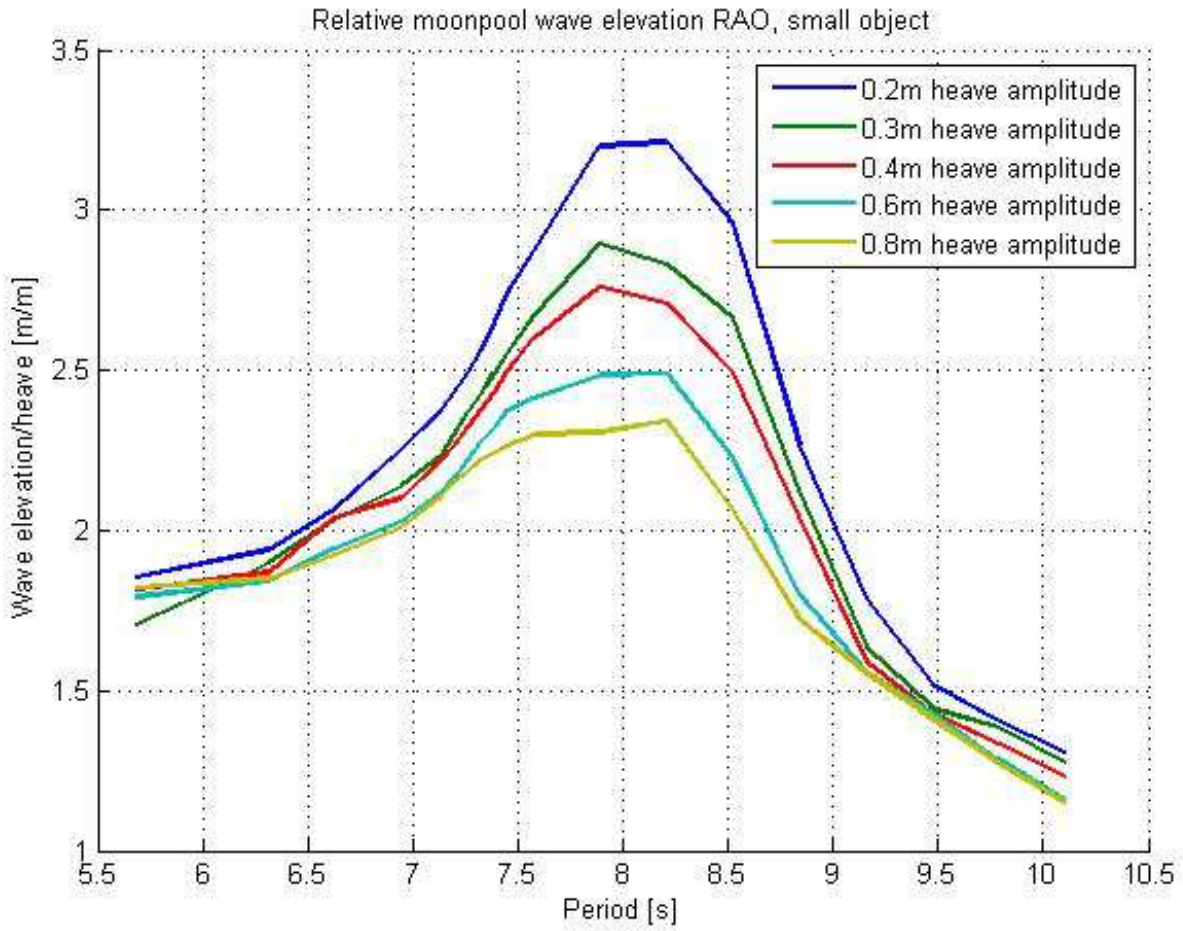

Figure 50 - Moonpool wave transfer functions, *Seven Viking* small object

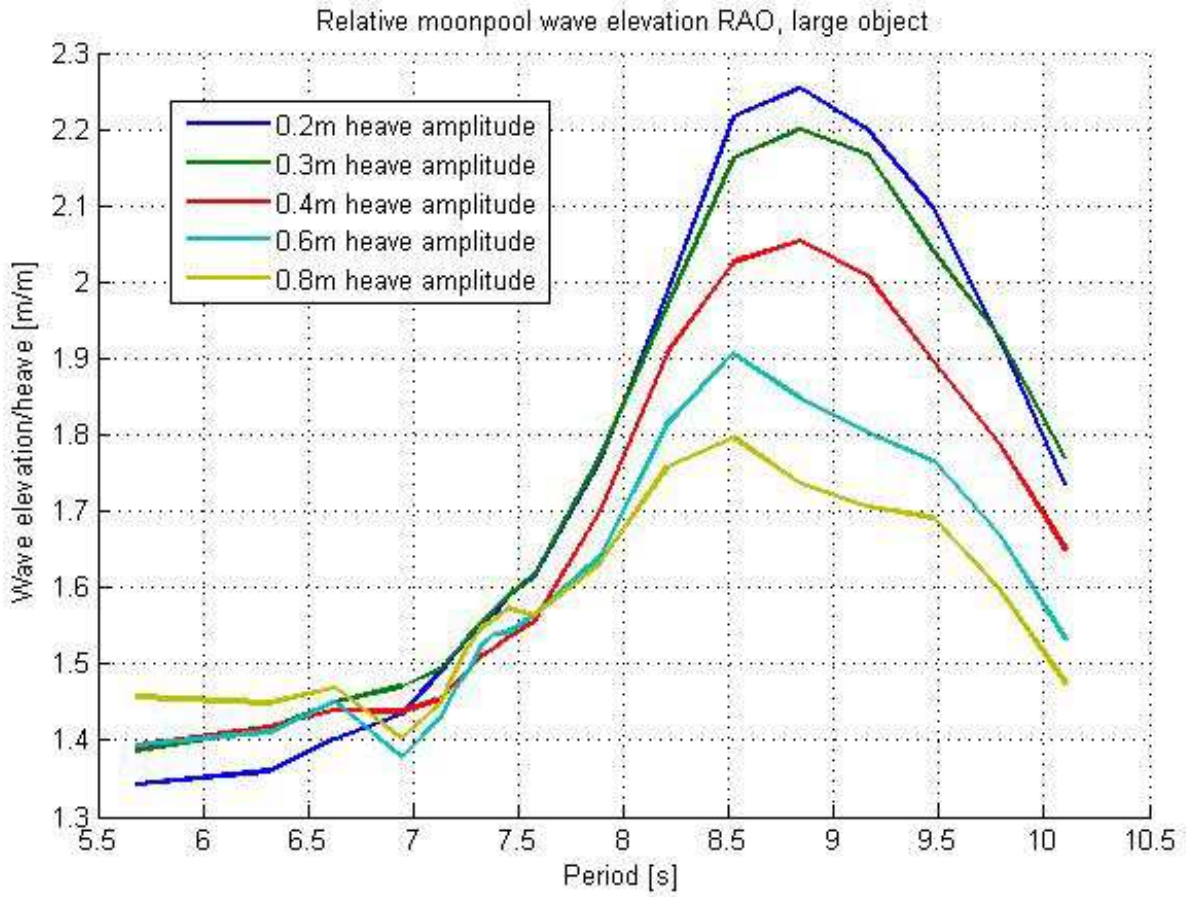

Figure 51 - Moonpool wave transfer functions, *Seven Viking* large object

In order to illustrate the differences even better, the transfer functions for one selected heave amplitude, 0.4m, for the wave elevation in the empty moonpool, with the small object and the large object can all be seen together in Figure 52.

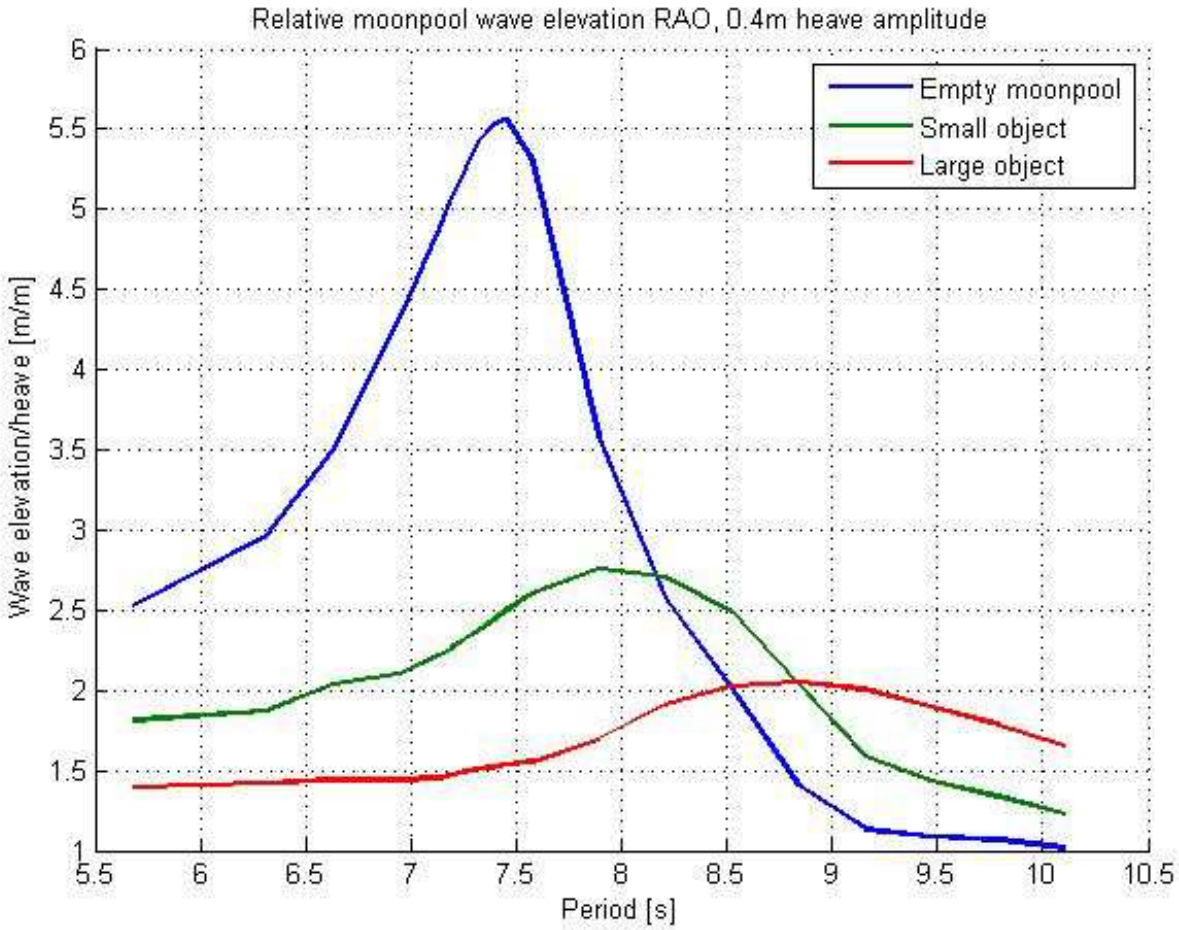

Figure 52 - Moonpool wave transfer functions, *Seven Viking*, empty, small and large

These plots demonstrate that the presence of an object in a moonpool increases the resonance period and considerably decreases the response amplitude; and the larger the object, the larger the changes are. When an object is positioned at the bottom of a moonpool, as they were in the tests, it acts as a constrictor of the inlet and hence the changes of the transfer functions are quite reasonable, based on the findings of Kristiansen et al. (Kristiansen et al. 2011) amongst others.

The extent to which even the small object changes the fluid motion inside the moonpool is striking. It is an indication of how incorrect it may be to model operations involving deployment through a moonpool using only transfer functions for an empty moonpool.

The PIV velocity fields for the small object, evaluated at the same instances and for the same excitation parameters as for the empty moonpools, can be seen in Figure 53 and Figure 54.

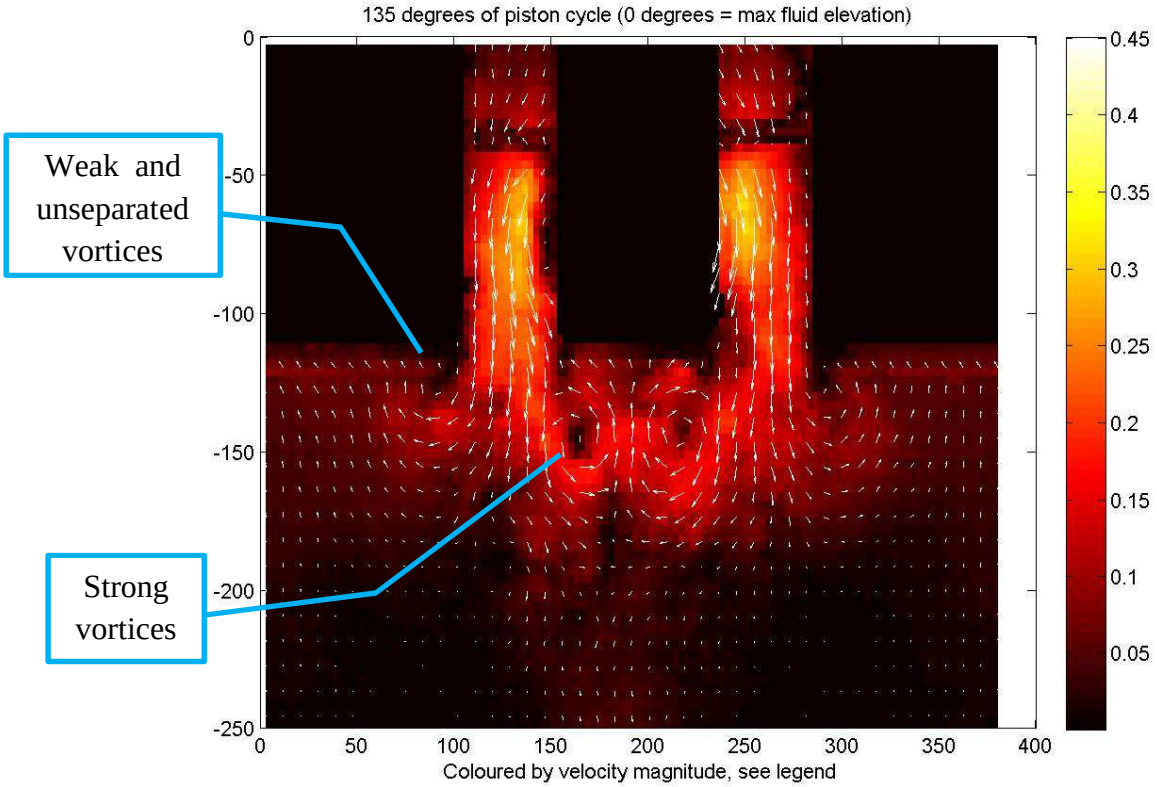

Figure 53 - PIV vectors, *Seven Viking* small object, flow out of moonpool

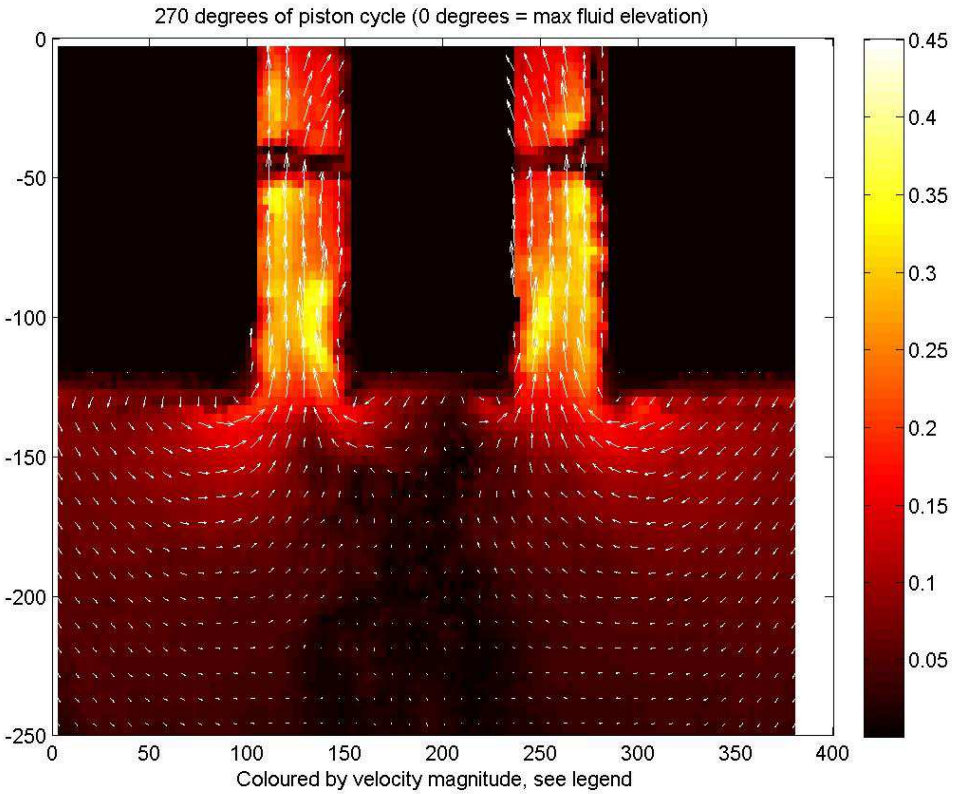

Figure 54 - PIV vectors, *Seven Viking* small object, flow into moonpool

Especially the velocity field of the outflow is attention-grabbing as it nicely illustrates the difference between flow separation from a rounded (the moonpool) and a sharp corner (the object). The sharp corner triggers vortex shedding to a much higher extent. This is also visible in the inflow, although the vortices are quite supressed by the narrow gap. The increased vortex shedding with the object inside the moonpool also leads to higher non-linear damping of the wave elevation, which is reflected in the transfer functions for the wave elevation; there is larger difference between the response levels at resonance with objects than there is without.

The same trends can also be seen for the outflow in Figure 55 with the large object in the moonpool.

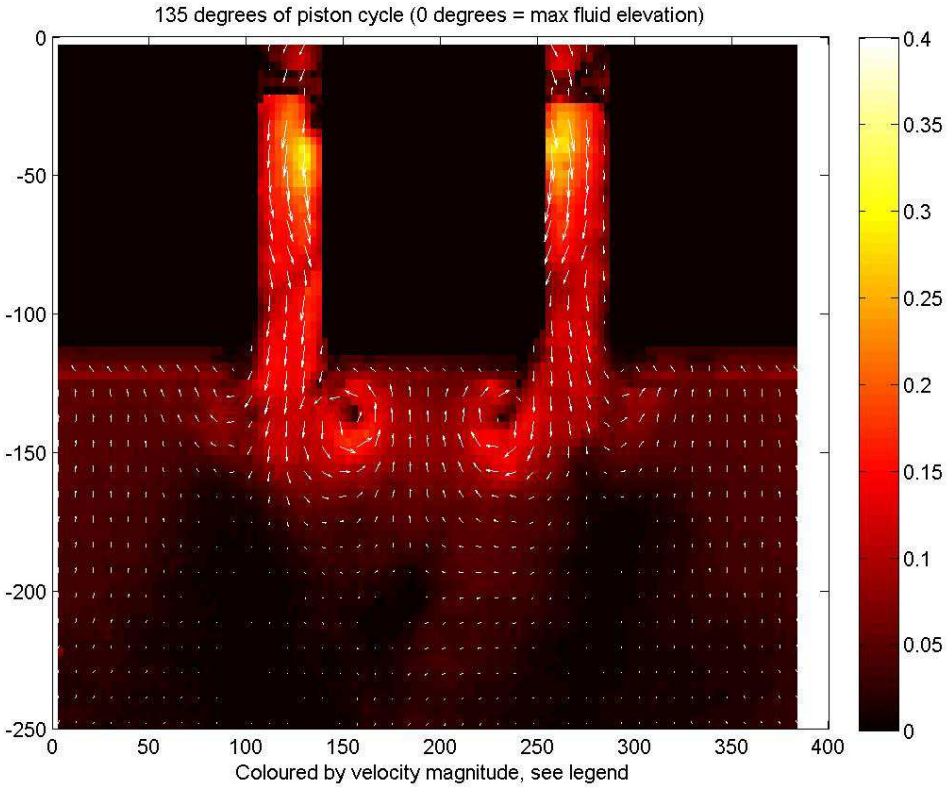

Figure 55 - PIV vectors, *Seven Viking* large object, flow out of moonpool

The wave transfer functions show that the amplitude of the wave elevation inside the moonpool is much lower with objects than it is without. If the wave elevation was to remain the same, the velocities would have to be much larger with objects than without to preserve the same volume flow. This is however not the case as seen in the PIV results. The velocities are actually smaller with an object than they are without. This is a consequence of the interaction between the object and the fluid which is mentioned at the end of section 2.

Objects in moonpool, force measurements

The force transfer functions for the small object are presented in Figure 56 and for the large object in Figure 57.

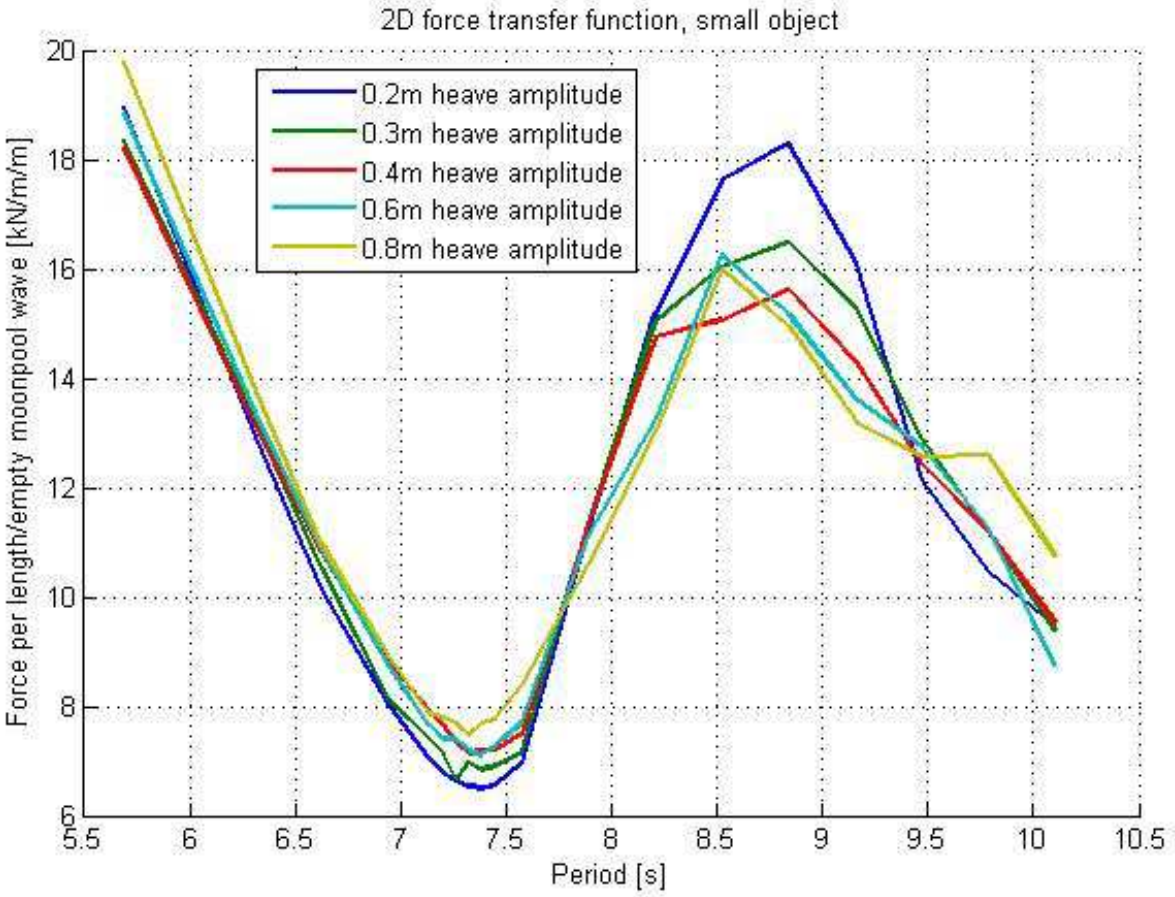

Figure 56 - Force transfer functions, small object

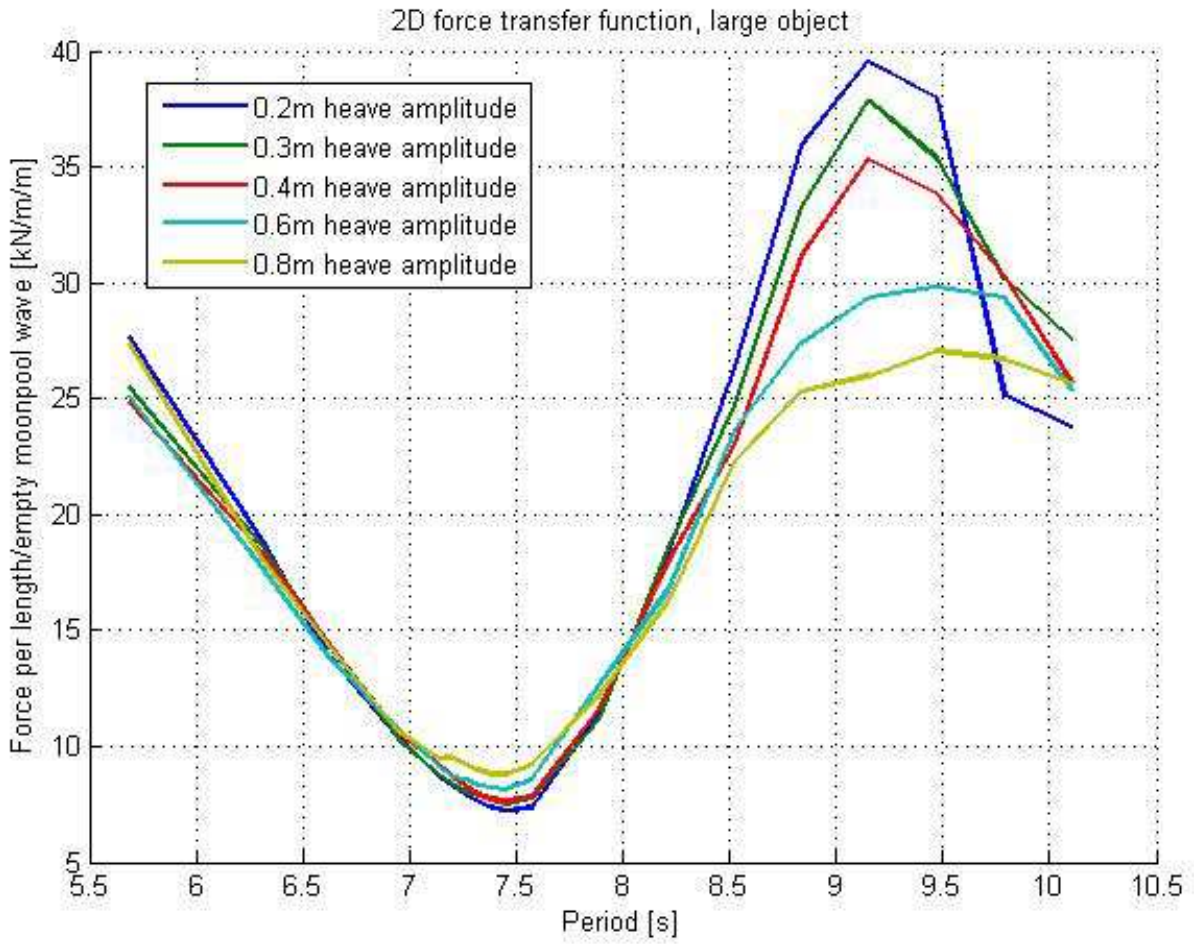

Figure 57 - Force transfer functions, large object

Because of the way the transfer functions are defined (force divided by the corresponding elevation in the empty moonpool) the curves have a low point around the empty moonpool resonance region, where the actual wave elevation with the object is much smaller than for the empty moonpool. Correspondingly, there are high points around the resonance region of the actual wave elevation.

It is remarkable how little the force transfer magnitude changes with excitation amplitude, except at the peaks in the force transfer functions. This implies a more or less linear relationship between the force and the excitation amplitude, which again implies, if one for a moment assumes the hydrodynamic force to be a combination of added mass and drag force, that the force is added mass-dominated. It should be kept in mind that this will not necessarily be the same in full scale.

If it is assumed that the total hydrodynamic force can be completely described by Morison's equation, i.e. the force is a sum of added mass and drag forces, it is possible to extract estimates for the drag and added mass coefficients using the method described in section 4. The resulting added mass coefficients for both objects are shown in Figure 58 and Figure 59.

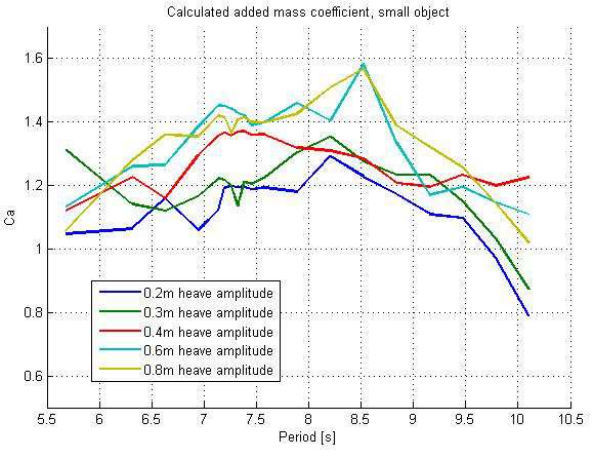

Figure 58 - Ca, small object

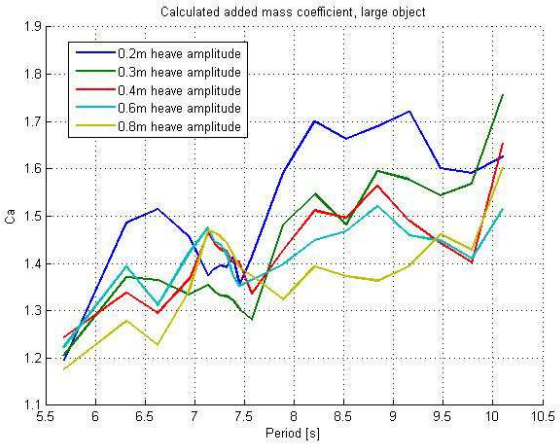

Figure 59 - Ca, large object

The results are quite inconsistent. The coefficients change significantly as the amplitude and period change. The results for the drag coefficients are even more fluctuating as seen in Figure 60 and Figure 61.

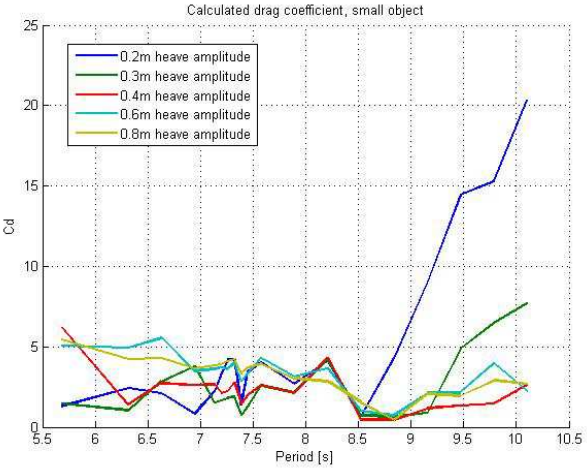

Figure 60 - Cd, small object

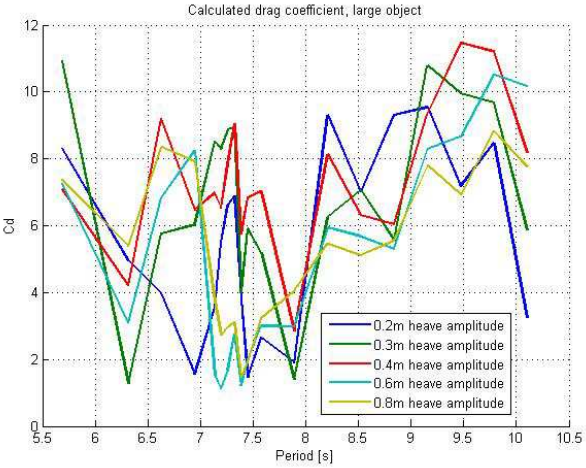

Figure 61 - Cd, large object

The drag coefficients are unstable to an extent which makes them not very trustworthy. One reason for this may be that the added mass-term is much larger than the drag-term and the drag-force is so small that even small changes have a large impact. Moreover, it is apparent that the lowest forcing amplitudes are the most unstable, especially at the highest periods. This is, not coincidentally, the cases with the lowest fluid velocities. Because the drag coefficient is found by dividing a quantity by the velocity squared, it is not unnatural that the results may turn out undependable when the velocity is small.

Although they may not have much quantitative value, the extracted estimates of the added mass and drag coefficients demonstrate the difficulties of precisely predicting the forces on objects in moonpools using Morison's equation.

6. Uncertainties

As for any kind of experiment, there were several uncertainties related to the model tests and their validity. The most important issues are discussed in this section.

Scale effects

The geometrical scaling ratio in the experiments was approximately 1:40. As with most marine model testing a Froude scaling scheme is used, implying equality of the ratio of inertia and gravitational forces which again implies that surface waves can be scaled directly. Effects arising from viscosity (which require equality in Reynolds number) are on the other hand not directly scalable (Steen 2012).

Assuming surface waves are more important than viscous effects is probably reasonable in this case. However, the important vortex shedding phenomenon is partially a consequence of viscosity and it should be kept in mind that this effect might appear different in full scale.

Also, with regards to forces on the objects in the moonpool, the Reynolds number may have some importance although this is often more important for spherical objects than the rectangular shapes considered in the current experiments.

2 dimensions

Although a 2-dimensional section of a moonpool was studied in which it was assumed that the lengthwise flow characteristics (into the plane) was constant, it is important to keep in mind that in real life everything is always in three dimensions. Even in an experiment like this it is impossible to completely avoid 3-dimensional effects. One indication of this can be seen in the time series of the individual wave probe signals inside the moonpool at large motions as the example in Figure 62 reveals.

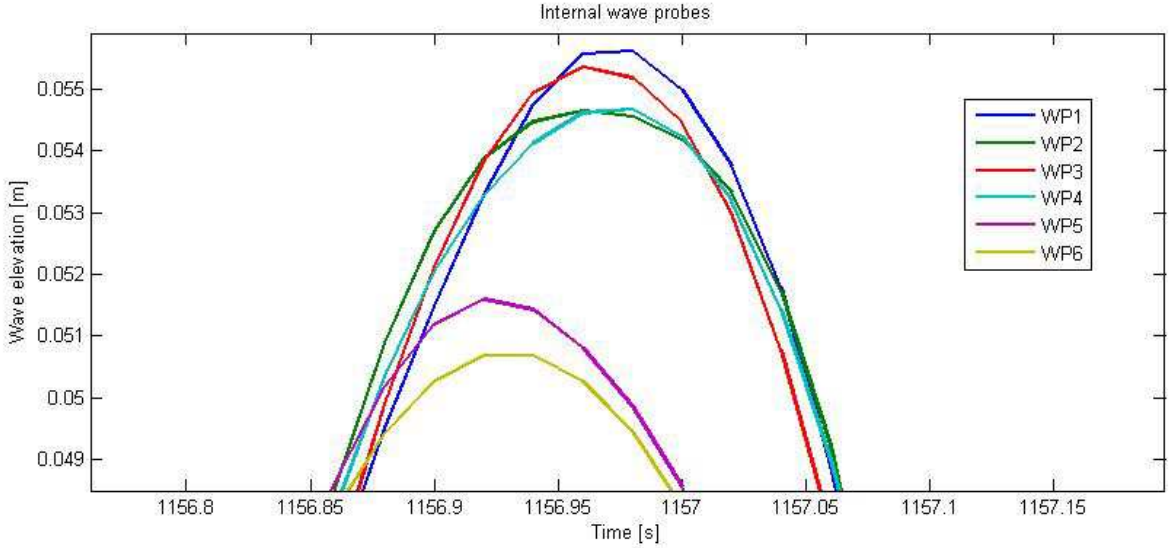

Figure 62 - Difference between middle and side in moonpool

For the case shown here there is a significant difference between the wave probes in the middle of the moonpool versus the wave probes at the sides (wave probes 5 and 6, see Figure 27). The case shown here is however one of the most extreme situations and for most instances the discrepancy was hardly noticeable.

While the wave elevation in most situations is practically uniform throughout the moonpool, there may be other smaller 3-dimensional fluid effects which are harder to identify. This could especially be the case for the vortices which are formed at the moonpool inlets. The PIV set-up used in these tests identifies the vortices in one section of the moonpool, but a more sophisticated set-up would be necessary in order to study any changes in the vortex formations along the moonpool. However, this lies outside the scope of the current experiments.

As will be shown later in section 7, the 2-dimensional set-up produces somewhat different results than a more realistic 3-dimensional set-up does. Because of this, the 2-dimensional set-up should mainly be used for studying trends.

Degrees of freedom

In these tests only heave motion of the model is considered. While this is by far the most critical motion for excitation of the water inside a moonpool, it is not hard to imagine that the flow field might be affected also by horizontal translatory motions and perhaps even more by rotational motions like roll or pitch. It is possible that one would see more horizontal fluid motions inside the moonpool if these degrees of freedom were included.

Harmonic motions

The experiments described in this thesis have been performed with regular harmonic motions of the model. An alternative approach is to use irregular motions described by the statistical properties of excitation spectra.

In reality, wave and vessel motions will always be irregular, which is a good reason for using the same approach also in model tests. However, doing this can sometimes make it harder to reveal the fundamental effects present in the tests which, in some ways, may get covered by a cloak of statistics. There are ways of extracting also the fundamental effects out of irregular tests, i.e. through methods based on Fourier transforms, but because the current tests mainly aimed to study fundamental effects and their trends (as opposed to get conditions as close to reality as possible), it was decided that regular motions would be the best choice. Especially the PIV tests would have been difficult to get any meaningful results from with irregular motions.

Still water

The wave elevation inside the moonpool (and outside) is, in these experiments, a consequence of the forced heave motion of the model only. There are no ambient incoming waves. In the real world on the other hand, incoming waves induce heave motions of the vessel, which again induce the moonpool wave elevation. If one assumes that the incoming waves causes the moonpool wave elevations only in this indirect manner, then it makes sense to study only the link between the heave and the moonpool wave. Not only does this make the results more generic, it also reduces the number of unknowns in the tests.

However, this assumption may not be completely true. It is likely that the inclusion of incoming waves could have affected the results to some extent.

Confined depth

The water depth in the experiments was around 1m. The maximum period of the radiated waves was 1.6s, and therefore, using the dispersion relation (Faltinsen 1990), the maximum wave length was roughly

$$\lambda = \frac{T^2}{2\pi}\tanh\left(\frac{2\pi}{\lambda}h\right)$$
$$\downarrow \qquad (64)$$
$$\lambda \approx 0.41m$$

This is well within the limits of what can be considered to be "deep water", i.e. the radiated surface waves should not be significantly affected by the confined water volume.

However, there may be other effects present beside the surface waves. Whenever the model was given the highest level of excitation (20mm), dirt on the bottom of the tank underneath the model was slowly pushed to the side, indicating a non-zero average flow which went down from the model to the bottom of the tank before it was separated to each side. This might have affected the results, especially for the higher amplitudes, but it is hard to say in which way and to what extent.

Wave reflections

A substantial effort was put into tuning the wave beaches to dampen out the radiated waves as efficiently as possible. The principally identical experiments done by Kristiansen et al. (Kristiansen et al. 2008) revealed how large impact fine tuning of the beaches had on the results.

The results from the validation case of the current experiments, where Kristiansen's set-up was recreated, showed good agreement. While this is a good indication of a successful tuning of the beaches, it is impossible to completely dampen out all radiated waves in an experiment like this.

Measurement uncertainties

With all kinds of measuring devices, there are limits to how accurately they can measure the desired quantity and also to the data acquisition frequency. The latter issue has not been a major concern in these experiments, as all important effects have cycles of more than 0.9 seconds. The sampling frequency was set to 50Hz (except for the PIV measurements which were set to 500Hz) which is assumed to be sufficient (Steen 2012).

With regards to accuracy all measurement devices were controlled at regular intervals in order to reveal deviations. Both the position and the force measurements were very stable throughout the tests. The wave probes were slightly more problematic and needed minor recalibration from time to time, e.g. at the start of a test session.

Uncertainties in PIV measurements

PIV equipment requires great care when setting up. It is important to adjust the laser beam meticulously in order to achieve a thin light sheet in the correct position. This was done by visual inspection, and therefore there are limits to how precisely the beam can be set up. The

camera also calls for careful adjustment of position and focus. It is assumed that both these things were done to a satisfactory level.

In Figure 36 it can be seen that there were some reflections from the laser on the tank walls. The resulting velocity vectors in these areas are probably somewhat affected by this. The presence of the wave probes also disturbed the PIV measurements to some extent.

The first PIV results were puzzling. Although the main flow phenomena appeared to be correct, there was a small yet significant "pulsating" of the vertical velocity. Figure 63 shows the vertical velocity at a specific point in the moonpool over a few seconds.

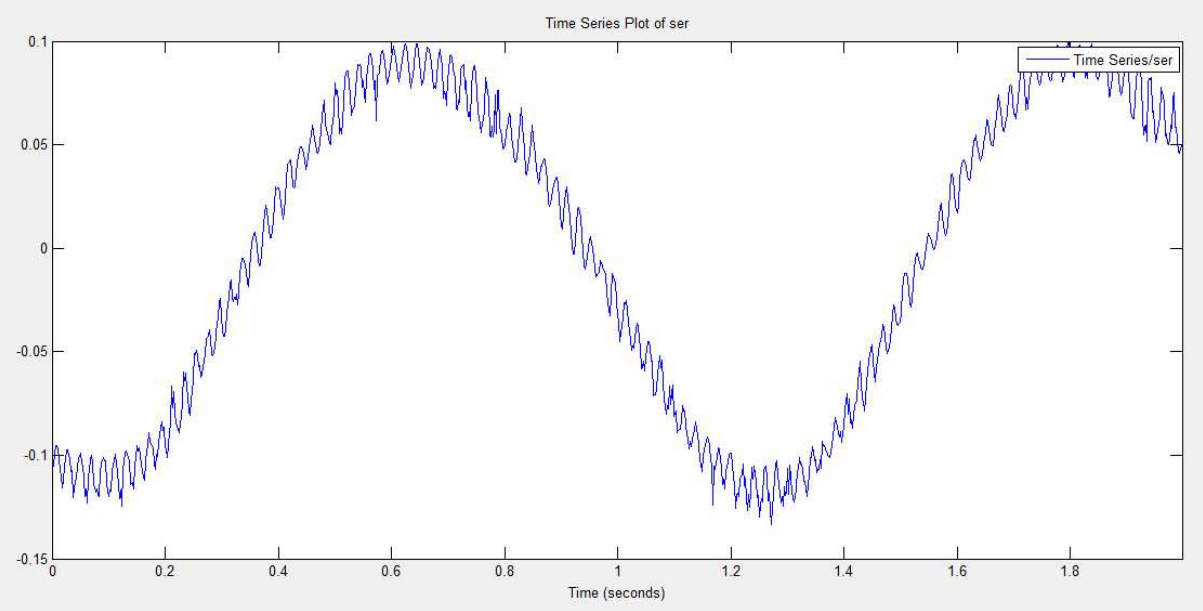

Figure 63 - PIV signal with noise

The signal comprises roughly of two harmonic motions; one corresponding to the excitation frequency and one with a frequency of around 48.5Hz. The latter one is clearly not physical, but it took a while to figure out the source of the noise. It turned out it was the cooling system of the laser which induced the vibrations through the wooden floor and probably made the camera "pitch" with this frequency. Figure 64 shows the energy spectrum derived from a time series produced by an accelerometer positioned on the floor.

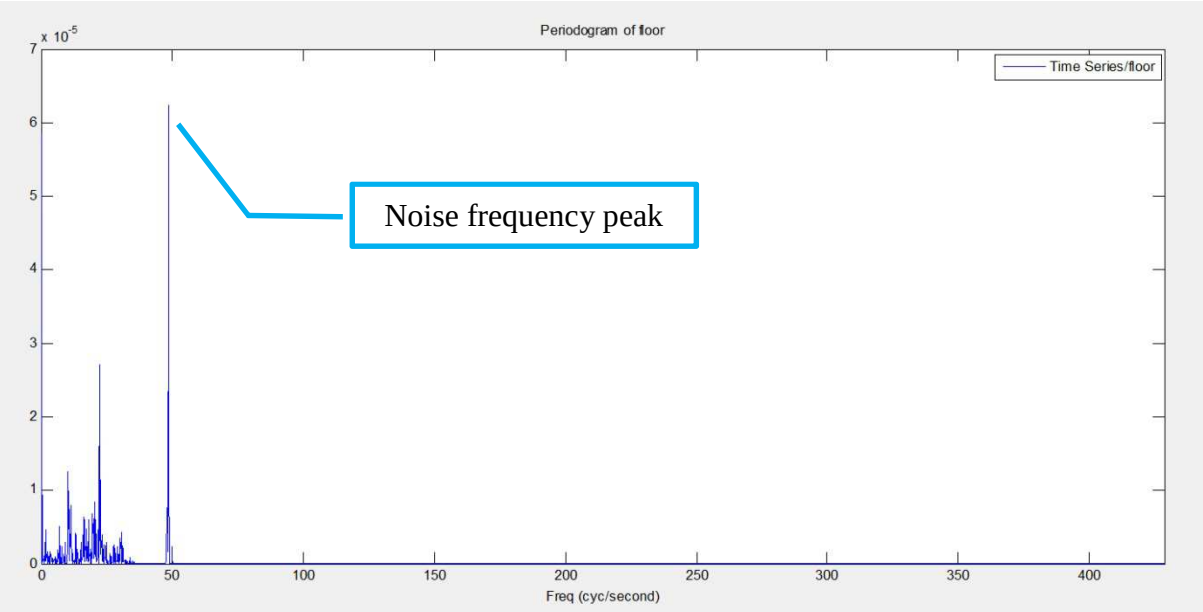

Figure 64 - Energy spectrum of floor vibrations

The peak corresponds to the noise frequency in the velocity signal. After the cooling pump was put on a foam mat, the vibrations disappeared and so did the noise in the PIV results.

Uncertainties in PIV analysis

Analysis of PIV pictures will always involve compromises. The size of the evaluation cells is a trade-off between stability and detail level. Careful selection of time-step is also vital in order to have the particles move sufficiently but not too much between each frame. The time step in these tests was set to 8ms which was necessary in order to get good results from the slow-moving regions of the flow. However, a consequence of this may be that the particles in the high speed regions, e.g. inside the vortices, may have somewhat higher displacements than ideal. This may have led to less accuracy in these regions.

All PIV results presented here are also time-averaged, i.e. the mean values of three frames are always used. Due to the high sampling rate in these tests (500Hz) this is assumed not to filter out any physical motions. The results are also, with some exceptions, phase-averaged over five cycles. This approach is good for identifying periodic flow phenomena but it is important to keep in mind that this scheme removes effects related to randomness such as turbulence.

For a quick visualization of what the phase-averaging cancels out, Figure 65 and Figure 66 shows a snapshot of the empty *Seven Viking*-moonpool in which the standard deviation of the horizontal and vertical velocities for the five phase-averaged cycles have been estimated respectively.

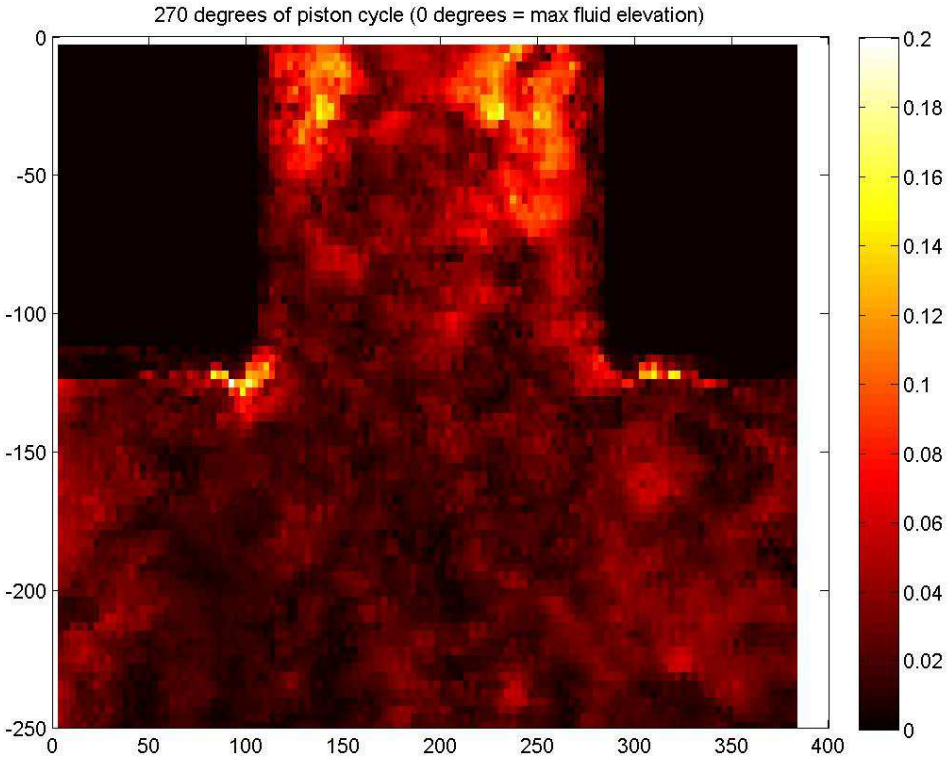

Figure 65 - Standard deviation of horizontal velocities over 5 cycles

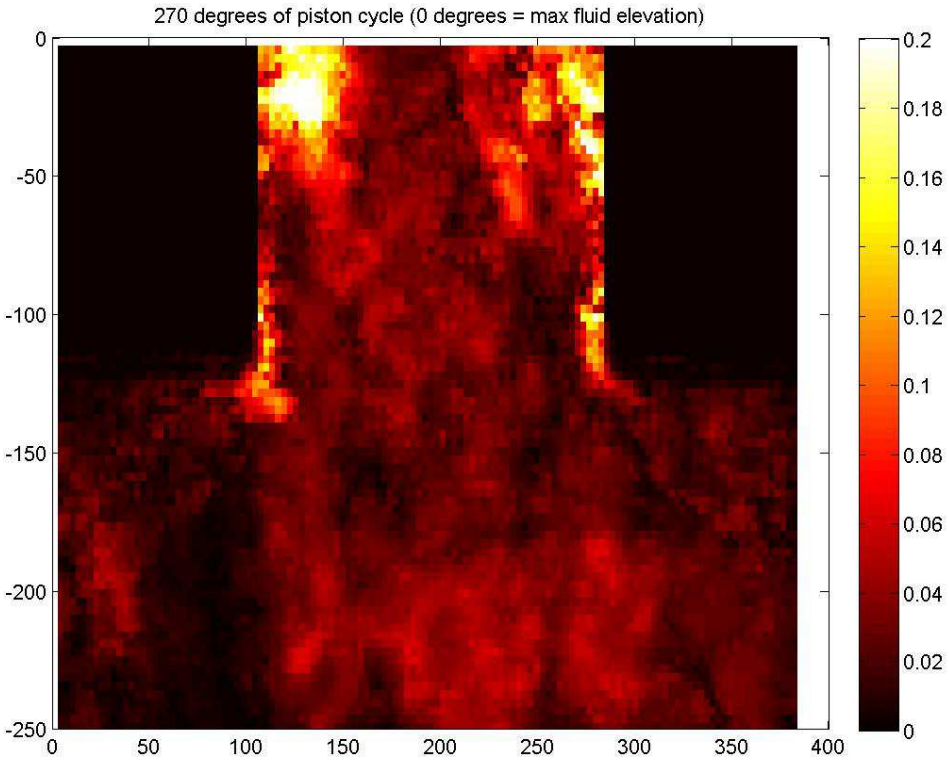

Figure 66 - Standard deviation of vertical velocities over 5 cycles

The standard deviations reveal significant velocity components which are cancelled out by phase-averaging. The regions which suffer most from this are the regions closest to the moonpool walls, which is not very surprising as these are “wake” regions in which the flow typically has a very random nature.

In Appendix A, PIV results for a cycle without phase-averaging for the empty *Seven Viking*-moonpool is included. These results are not very unlike the phase-averaged results, but they are somewhat less symmetric and slightly more chaotic.

7. Comparison with 3D model tests

In April 2013 Kjetil Berget carried out model tests on the moonpool of *Seven Viking* at MARINTEK on the request of Tor-Bjørn Idsøe Næss of *Subsea 7*. These tests involved a 3-dimensional moonpool with a scaling ratio of 1:25. The moonpool section was put into a generic ship hull and connected to an actuator capable of producing motions in all degrees of freedom, but only heave was applied in these tests.

These 3D-tests are assumed to quite accurately describe the fluid motions in the real full scale *Seven Viking*-moonpool. Because of this, quantitative results are not included in this thesis due to confidentiality issues.

While irregular motions were used for most of the tests (in which Fourier transforms were applied to extract the transfer functions), some test runs were also done with regular motions. For the empty moonpool, the wave elevation transfer functions can be seen in Figure 67.

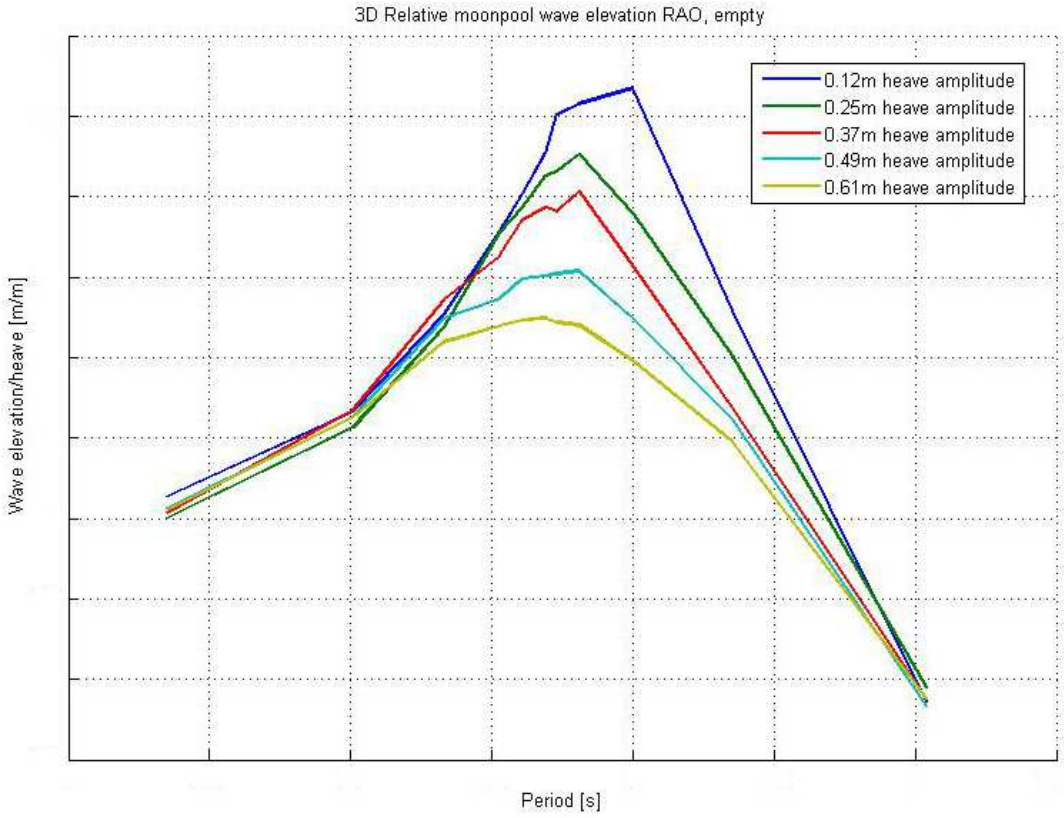

Figure 67 - 3D Moonpool wave transfer functions, Seven Viking empty

There are several differences compared to the results from the 2D tests as seen in Figure 46. The resonance period is lower in the 3D case. This is as expected, according to Molin's work as described in section 2.

Moreover, it seems the non-linear damping level is higher in the 3D case as well. Not only are all amplitudes lower than in the 2D case, the differences between the excitation levels are also more prominent. It is no surprise that the damping level is higher in 3D, where the flow is damped by inlets and perforated walls on four sides as opposed to only two sides in 2D. Also, in the 2D case the volumes behind the perforated walls were unrealistic small because of the

thick aluminium plates as discussed in section 3. In the 3D case, this issue was less important because of the lower scaling ratio.

An object corresponding to the large object in the 2D tests was also tested in the 3D experiments. The resulting wave transfer functions can be seen in Figure 68.

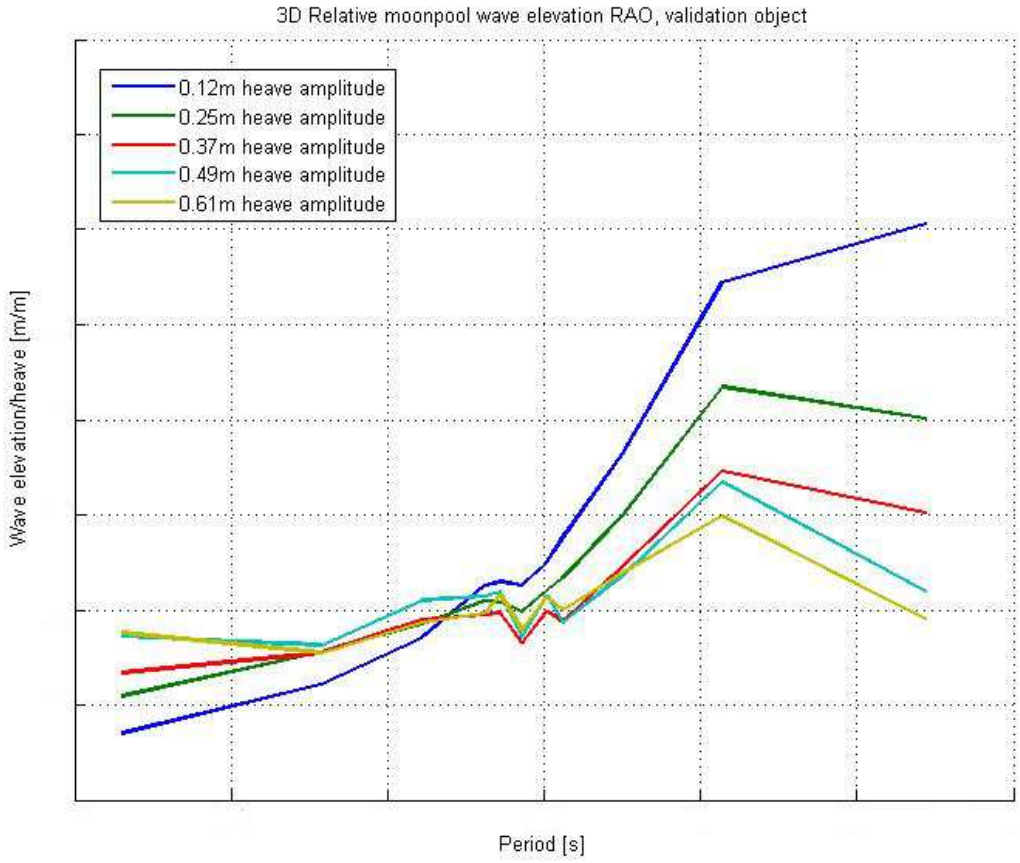

Figure 68 - 3D Moonpool wave transfer functions, Seven Viking large object

The same trends can be seen as for the 2D tests; the resonance period increases and the response amplitude decreases. However, both these effects are smaller in the 3D case compared to the 2D case. This is probably because the blockage factor is different even though the full scale dimensions are equal. In 2D, the blockage factor is:

$$r_{blockage,2D} = \frac{4m}{7.175m} \approx 0.56 \tag{65}$$

while in 3D it is:

$$r_{blockage,3D} = \frac{(4m)^2}{(7.175m)^2} \approx 0.31 \tag{66}$$

The differences between the 2D and the 3D tests indicate that the 2D experiments should mainly be used for studying trends as opposed to regarding their results directly relatable to reality.

8. Comparison of experimental results with simplified calculations

It was of great interest to investigate how a simplified numerical scheme could predict the results obtained from the model tests. In this section DNV's recommended practice for moonpool operations has been applied (DNV 2011) on the same conditions as in the current 2-dimensional model tests of *Seven Viking* with both objects. This methodology is outlined in section 2.

A heave excitation amplitude of 0.4m is used throughout the calculations.

The first step is to determine the resonance period of the moonpool. This is done using the formula (DNV 2011):

$$T_0 = \frac{2\pi}{g}\sqrt{\int_{z=-D}^{0}\frac{A(0)}{A(z)}dz + \frac{A(0)}{A(-D)}\kappa\sqrt{A(-D)}} \tag{67}$$

where T_0 is the resonance period, g is the gravitational constant, z is the vertical axis ranging from –D at the bottom of the moonpool to 0 at the free surface, A(z) is the varying cross sectional area of the moonpool, A(0) is the area at the surface and A(-D) is the area at the inlet. κ is a constant which DNV recommends to be set between 0.45 and 0.47. However, this is valid only for a 3-dimensional moonpool. Molin, who originally derived the result, proposed a value of 0.736 for a 2-dimensional case and this value is used here (Molin 2001).

To make the calculations more trivial, the rounded edges of the moonpool inlet has been assumed to be sharp squares instead. The resonance period of the empty moonpool then becomes:

$$T_{0,DNV} = 7.20s \tag{68}$$

which, compared to the model test results for the empty moonpool, is actually quite accurate. This formula is based on potential theory which has often been shown to be capable of determining the resonance period of moonpools (Heo et al. 2010).

The next step would be to determine the damping level. After this has been selected, a generic moonpool transfer function can be calculated. DNV provides example transfer functions of moonpool elevation divided by the incoming wave. These are however not directly relatable to the current experiments, because forced heave with no incoming waves have been used and transfer functions between the moonpool wave elevation and the model heave have been found instead. Therefore, throughout the rest of the calculations, the actual transfer function (for the empty moonpool) obtained in the current model tests, which can be seen in Figure 69, is used. Using the actual transfer function also eliminates the uncertainties related to selecting the correct damping level and hence makes it easier to investigate the validity of the force calculations isolated from the rest of the methodology and its uncertainties.

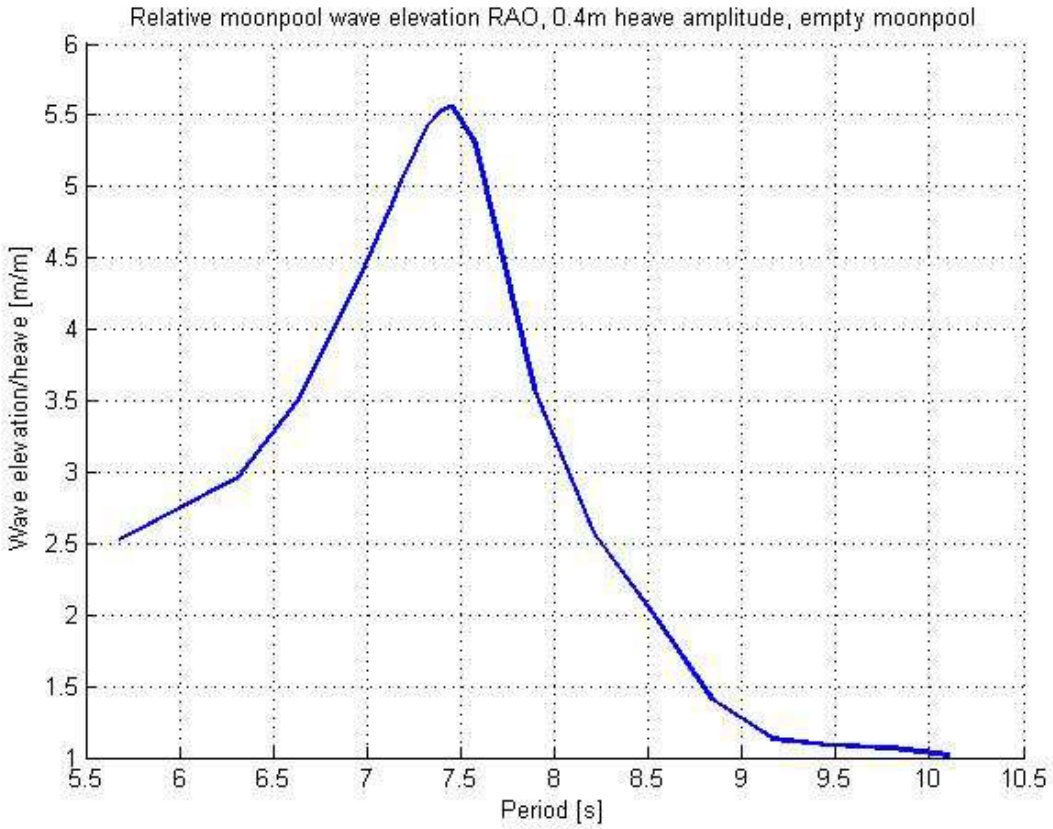

Figure 69 - Moonpool wave transfer function, Seven Viking empty

The force calculations are based on Morison's equation as described in section 2. First, drag and added mass coefficients must be determined for motion in an unconfined fluid domain. This is simple in this case, as the objects in question are squares. The coefficients, given by DNV (DNV 2010), are set to:

$$C_{D0} = 2.2$$
$$C_{A0} = 1.51 \tag{69}$$

To correct for the confined fluid domain inside the moonpool, DNV proposes correction formulas given by (DNV 2011):

$$\frac{C_A}{C_{A0}} = 1 + 1.9\left(\frac{A_b}{A}\right)^{9/4}$$
$$\frac{C_D}{C_{D0}} = \frac{1 - 0.5A_b / A}{(1 - A_b / A)^2} \tag{70}$$

where C_A and C_{A0} are the added mass coefficients for confined and unlimited fluid domain, C_D and C_{D0} are the corresponding drag coefficients, A_b is the projected area of the body and A is the cross-sectional area of the moonpool.

For the small square, with a blockage ratio of 0.42, the corrected coefficients then become:

$$C_{D,small} = 5.11$$
$$C_{A,small} = 1.91 \tag{71}$$

And for the large, with blockage of 0.56:

$$C_{D,large} = 8.04$$
$$C_{A,large} = 2.27 \tag{72}$$

The combined maximum sectional hydrodynamic forces are now found from Morison's equation given by:

$$F_{2D,\max} = \max\left(\rho b^2 (1 + C_A) a_z(t) + \frac{1}{2} \rho b C_D \left| w(t) \right| w(t) \right) \tag{73}$$

where ρ is the fluid density, b is the breadth and height of the object, a_z is the vertical fluid acceleration and w is the vertical fluid velocity. w and a_z are found from the moonpool RAO using the standard relations for harmonic motions:

$$w(t) = i \cdot \frac{2\pi}{T} \cdot \zeta(t) = i \cdot \frac{2\pi}{T} \cdot \zeta_S(t) \cdot RAO(T)$$
$$a_z(t) = -\left(\frac{2\pi}{T} \right)^2 \cdot \zeta(t) = -\left(\frac{2\pi}{T} \right)^2 \cdot \zeta_S(t) \cdot RAO(T) \tag{74}$$

where T is the period, ζ is the wave elevation in the moonpool, ζ_S is the heave motion of the vessel and RAO(T) is the RAO for each considered period.

The results are plotted as force transfer functions and compared to those found in the model tests and can be seen in Figure 70.

The plot clearly indicates how the simple method fails to predict not only the magnitude of the forces but also the trends. The main reason for this is probably because the method assumes that the flow field inside the moonpool is unaffected by the presence of the objects, but the RAO's from the model tests with empty moonpool, with the small object and with the large object show that this assumption is highly questionable as demonstrated in Figure 71. Not only is the overall wave elevation strongly reduced with objects inside the moonpool, the peak is also shifted to a higher period.

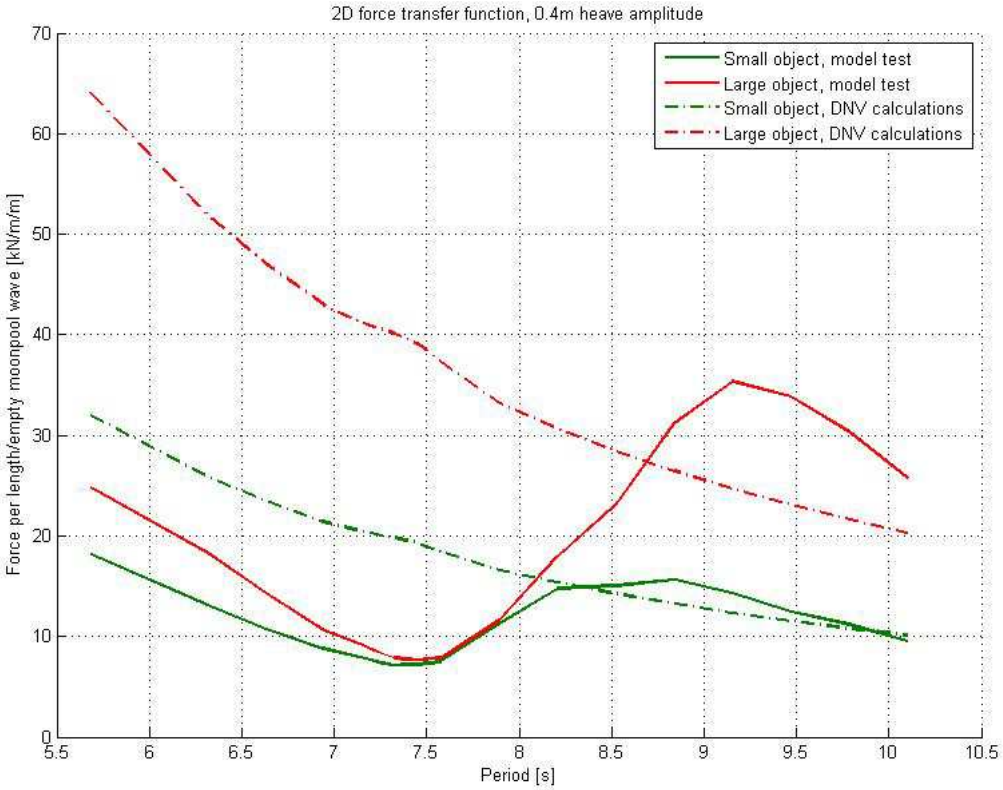

Figure 70 - Force transfer function comparison

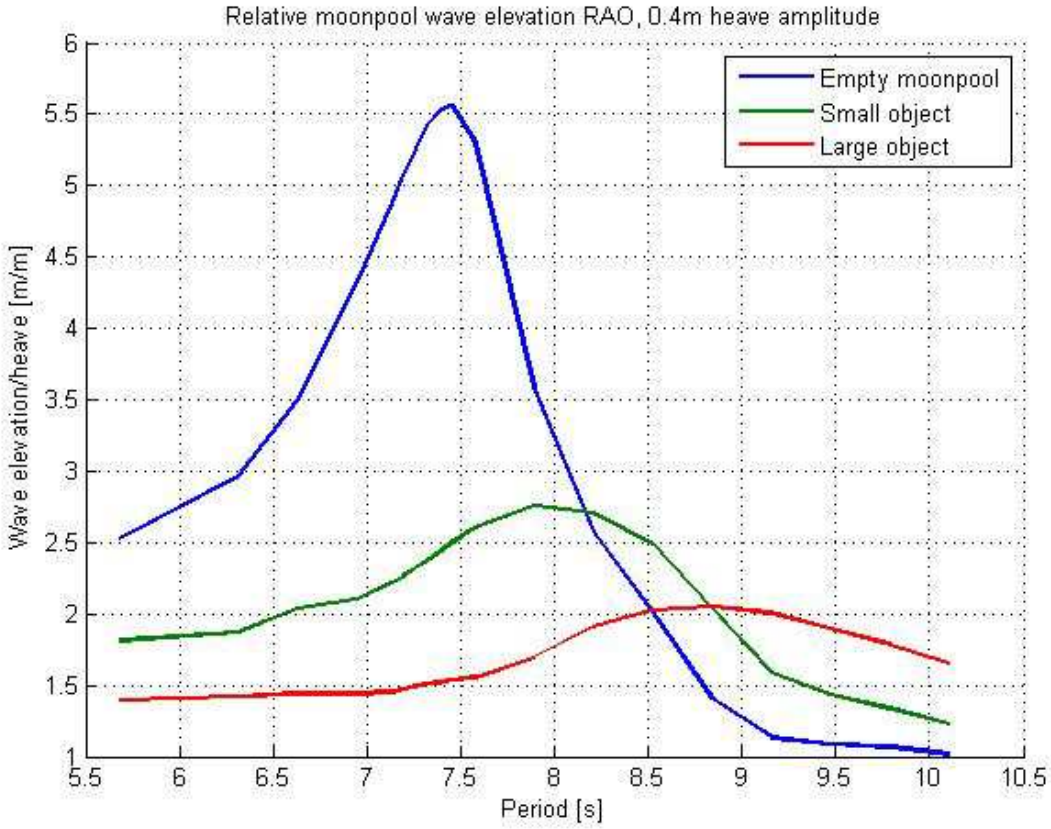

Figure 71 - Moonpool wave transfer functions, *Seven Viking*, empty, small and large

If instead the RAO's of the moonpool with an object inside is used as a starting point for the calculations, the scheme yields considerably better results as seen in Figure 72.

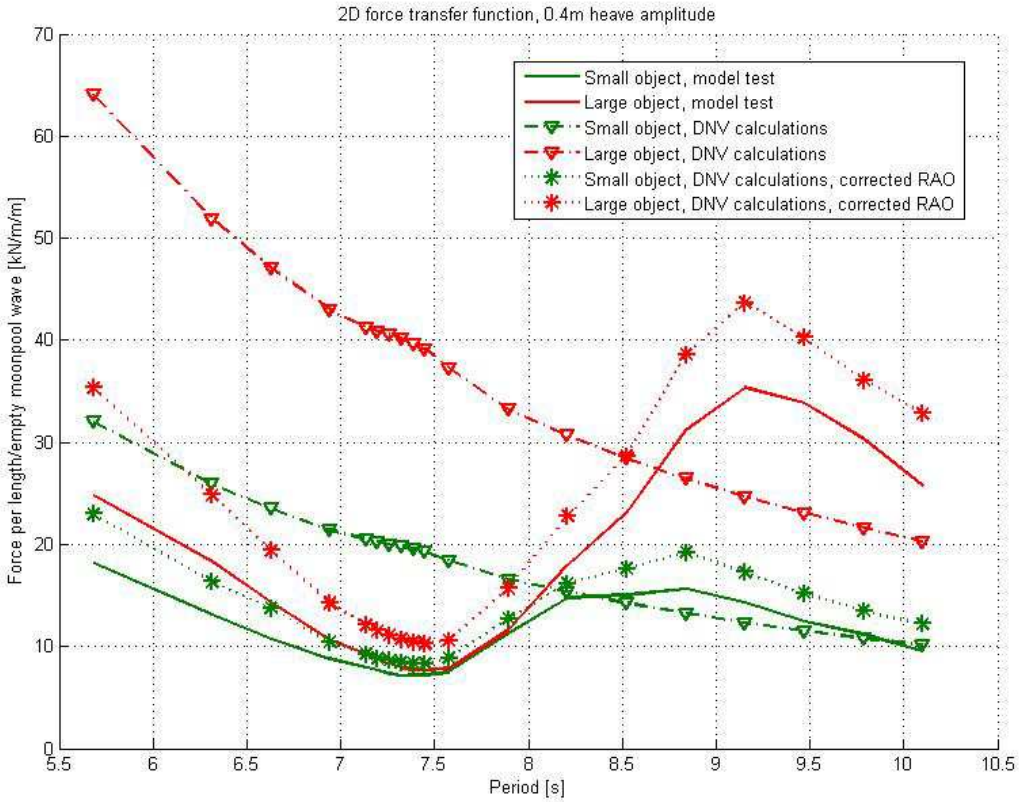

Figure 72 - Force transfer function comparison, expanded

Although the forces also in this case are overestimated, the discrepancies are acceptable, and equally important, the trends are captured very well. These results give some credibility to the formulas for correction of the drag and added mass coefficients.

One could almost be tempted to conclude that the forces on objects in moonpools can indeed be estimated using this scheme, provided that a transfer function for the wave elevation in the moonpool with the actual object is known. However, the problem lies in determining this transfer function, which is not a trivial task unless model tests (or perhaps cfd calculations) have been performed. And in such experiments the forces can easily be directly found anyway, which is also a more reliable method.

9. Conclusions

Due to the many simplifications, and especially because of the 2-dimensional set-up, the results from the current experiments may not be directly relatable to real moonpools in full scale. Not only is there a difference in response level, there is also a discrepancy in the resonance period. On the other hand, the model tests have revealed very interesting trends which are assumed to exist also in real conditions.

The most important findings are related to the tests with objects in the moonpool. It is remarkable how the fluid motion in the moonpool gets altered also for the smallest object which has a relatively modest blockage ratio. It is often assumed that such "small" objects do not alter the ambient flow to a significant degree. Although this could be reasonable for some applications, the current experiments strongly indicate that this assumption does not hold for the fluid motions in moonpools.

The dramatic change in the moonpool wave elevation transfer function when an object is introduced, is the main reason why the methodology for calculating the forces on the objects as outlined by DNV gives such poor results. On the other hand, the calculations based on the actual transfer functions with an object inside the moonpool gave much better results which would have been acceptable for analysis of moonpool operations. This gives some credibility to the method of correcting hydrodynamic coefficients based on the blockage ratio (assuming the fluid flow is also corrected), though it is hard to say whether equally good results would have been found for other conditions, moonpool geometries etc.

It seems the core of the problem of analysing moonpool operations lies in determining the correct wave elevation transfer functions, especially for moonpools with objects inside. Historically, a considerable effort has been put into developing methods and tools for determining the surface elevation in empty moonpools. Much progress has been made, but the reliable methods are still too complicated and time-consuming for practical use. Additionally, practically no effort has so far been put into finding the corresponding transfer functions with objects inside the moonpools, which, in the current experiments, have been found to be crucial for correct estimation of the forces on the objects.

Today, the only reliable method for predicting forces on objects in moonpools appears to be experimental testing. It would probably be very beneficial to carry out a comprehensive series of generic model tests involving a range of typical moonpool designs and several objects of various sizes and levels of perforation at different positions in the moonpool. By doing this it would perhaps be possible to extract trends for how the moonpool wave transfer functions changes for various types of objects, which could hopefully lead to the development of reliable empirical methods. Or, if no general trends can be found, it would be an incentive for putting more effort into developing numerical tools.

The use of PIV has been a great asset in the experiments. Although the most crucial measurements were obtained from conventional wave probes and force transducers, the ability to visualize the flow field was an immense help for understanding the causes as opposed to only observing the consequences. It is likely that PIV is a technique which will be more and more used in the future, and the complexity of the problems which it is applied to will increase. For research on moonpools the potential is huge. Especially when it comes to optimizing the design of a moonpool it would probably be very valuable to study in detail e.g. how the perforated walls should be designed to allow for the ideal amount of flow through them or which inlet configuration leads to the most vortex formation.

The current tests indicate that the *Seven Viking*-moonpool could have had a higher level of non-linear damping and therefore also less fluid motions simply by having a sharp-cornered inlet which would have resulted in stronger vortices being formed.

References

Aalbers AB (1984). The water motions in a moonpool. *Ocean Engineering,* vol. 11, pp. 557-579.

Adrian RJ, Westerweel J (2011). *Particle image velocimetry.* New York: Cambridge University Press.

Det Norske Veritas (2010). *DNV-RP-C205 Environmental conditions and environmental loads*. Det Norske Veritas.

Det Norske Veritas (2011). *DNV-RP-H103 Modelling and Analysis of Marine Operations*. Det Norske Veritas.

Faltinsen OM, Rognebakke OF, Timokha AN (2007). Two-dimensional resonant piston-like sloshing in a moonpool. *Journal of Fluid Mechanics* vol. 575, pp. 359-397.

Faltinsen OM (1990). *Sea loads on ships and offshore structures.* Cambridge: Cambridge University Press.

Ferziger JH, Peric M (2002). *Computational methods for fluid dynamics.* Third edition. Berlin Heidelberg: Springer.

Fukuda K (1977). Behaviour of water in vertical well with bottom opening of ship, and its effects on ship motion". *Journal of the Society of Naval Architects of Japan,* vol. 141.

Graham JMR (1980). The forces on sharp-edged cylinders in oscillatory flow at low Keulegan-Carpenter numbers. *Journal of Fluid Mechanics* vol. 97, pp. 331-346.

Heo J, Park J-C, Kim M-H, Koo W-C (2010). Numerical analysis of a floating body with two-dimensional moonpool including piston mode. *Proceedings of the ASME 2010 29th International Conference on Ocean, Offshore and Arctic Engineering OMAE2010*.

Kristiansen T, Faltinsen OM (2008). Application of a vortex tracking method to the piston-like behaviour in a semi-entrained vertical gap. *Applied Ocean Research* vol. 30, pp. 1-60.

Kristiansen T, Faltinsen OM (2011). Gap resonance analysed by a new domain-decomposition method combining potential and viscous flow. *Applied Ocean Research* vol. 34, pp. 198-208.

Madsen NF (1980). Prediction of water level motion and forces acting on a diving bell during launching through a moonpool. *Skibsteknisk laboratorium*.

Massey BS (1975). *Mechanics of Fluids*. Van Nostrand Reinhold Company.

Molin B (2001). On the piston and sloshing modes in moonpools. *Journal of Fluid Mechanics,* vol. 430, pp. 27-50.

Pettersen B (2007). *Marin teknikk 3: Hydrodynamikk*. Lecture Notes. Norwegian University of Science and Technology.

Sharma A, Eswaran V (2004). Effect of channel confinement on the two-dimensional laminar flow and heat transfer across a square cylinder. *Numerical heat transfer, part A: Applications: An international journal of Computation and Methodology*, 47:1, pp. 79-107.

Singha S, Sinhamahapatra KP (2010). Flow past a circular cylinder between parallel walls at low Reynolds numbers. *Ocean engineering*, vol. 37, pp. 757-769.

Steen S (2012). *Experimental methods in marine hydrodynamics.* Lecture notes. Norwegian University of Science and Technology.

Torres FGS, Alexandre TPA, Sales-Jr. JS (2008). Experimental and numerical analysis of the behaviour of a monocolumn with a moonpool. *Proceedings of the ASME 27th International Conference on Offshore Mechanics and Arctic Engineering OMAE2008.*

Visscher J (2011). *Application of particle image velocimetry on turbulent marine flows.* PhD Thesis. Norwegian University of Science and Technology.

White FM (2008). *Fluid Mechanics.* Sixth edition. New York: McGraw-Hill.

Zdravkovich MM (2003). *Flow around circular cylinders vol. 2: Applications.* New York: Oxford University Press.

Table of figures

Appendices

Appendix A: PIV results

PIV results

Included here are the PIV results for all configurations for a whole oscillation cycle.

All cases have an excitation amplitude of 15mm (corresponding to approximately 0.6m in full scale for the *Seven Viking*-model) and a period of 1.17s (approximately 7.4s in full scale for the *Seven Viking*-model).

Vector plots

The vector plots show snapshots of the flow at eight instances over a full cycle. The vectors are plotted over a colour-map which displays the velocity magnitudes.

Base case

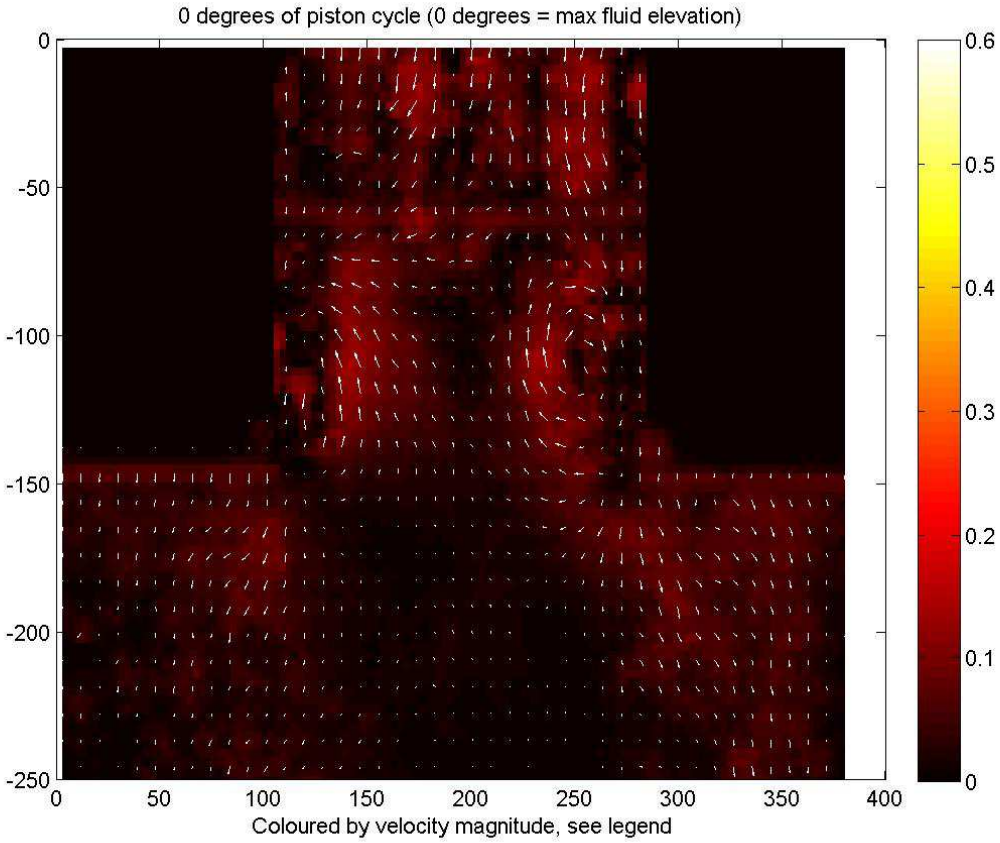
0 degrees of piston cycle (0 degrees = max fluid elevation)
0
-50
-100
-150
-200
-250
0
50
100
150
200
250
300
350
400
0.6
0.5
0.4
0.3
0.2
0.1
0
Coloured by velocity magnitude, see legend

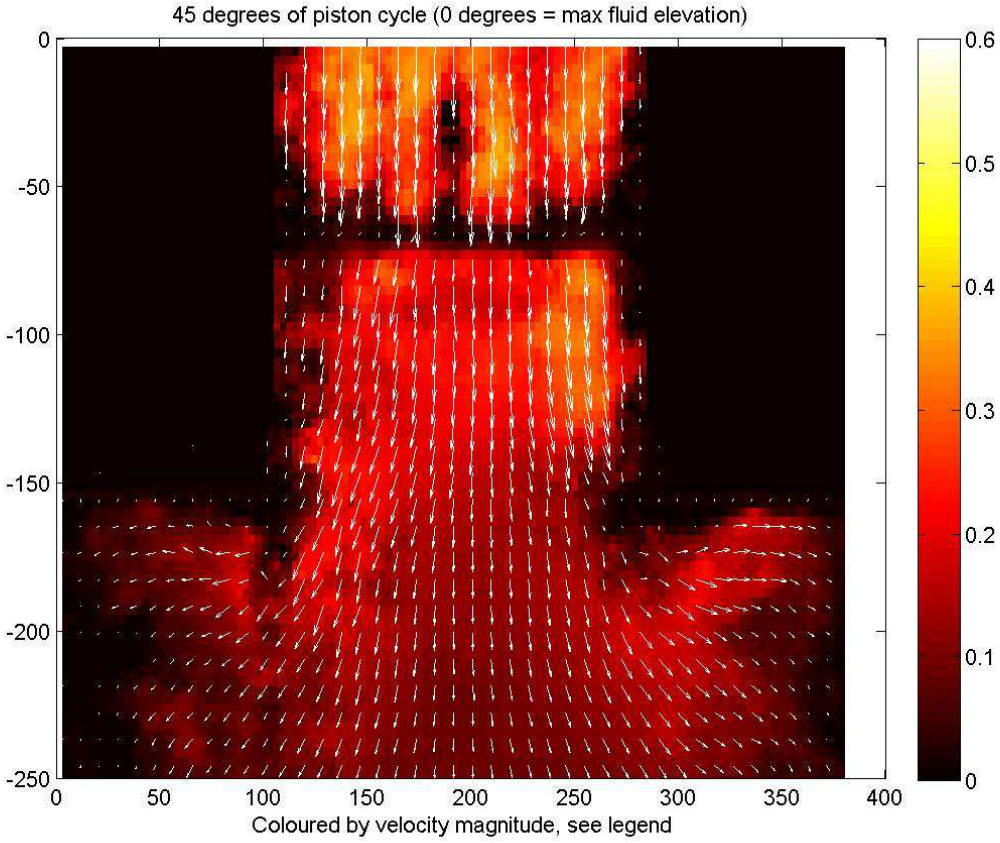
45 degrees of piston cycle (0 degrees = max fluid elevation)
0
-50
-100
-150
-200
-250
0
50
100
150
200
250
300
350
400
0.6
0.5
0.4
0.3
0.2
0.1
0
Coloured by velocity magnitude, see legend

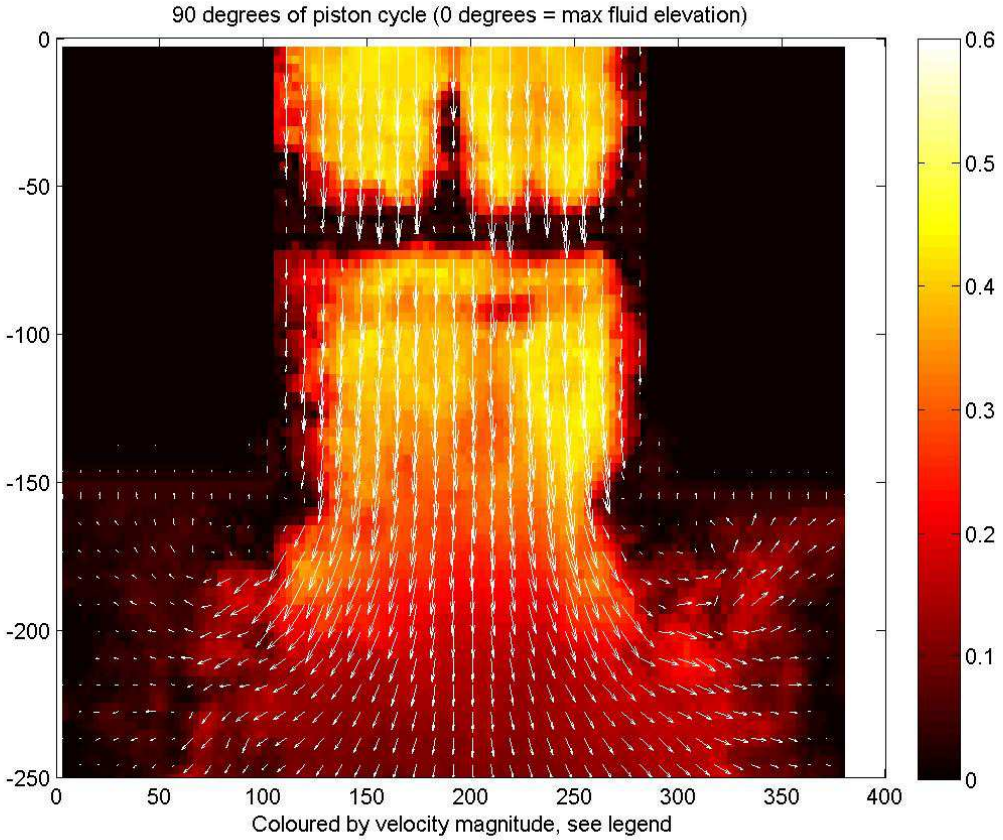
90 degrees of piston cycle (0 degrees = max fluid elevation)
0
-50
-100
-150
-200
-250
0
50
100
150
200
250
300
350
400
0.6
0.5
0.4
0.3
0.2
0.1
0
Coloured by velocity magnitude, see legend

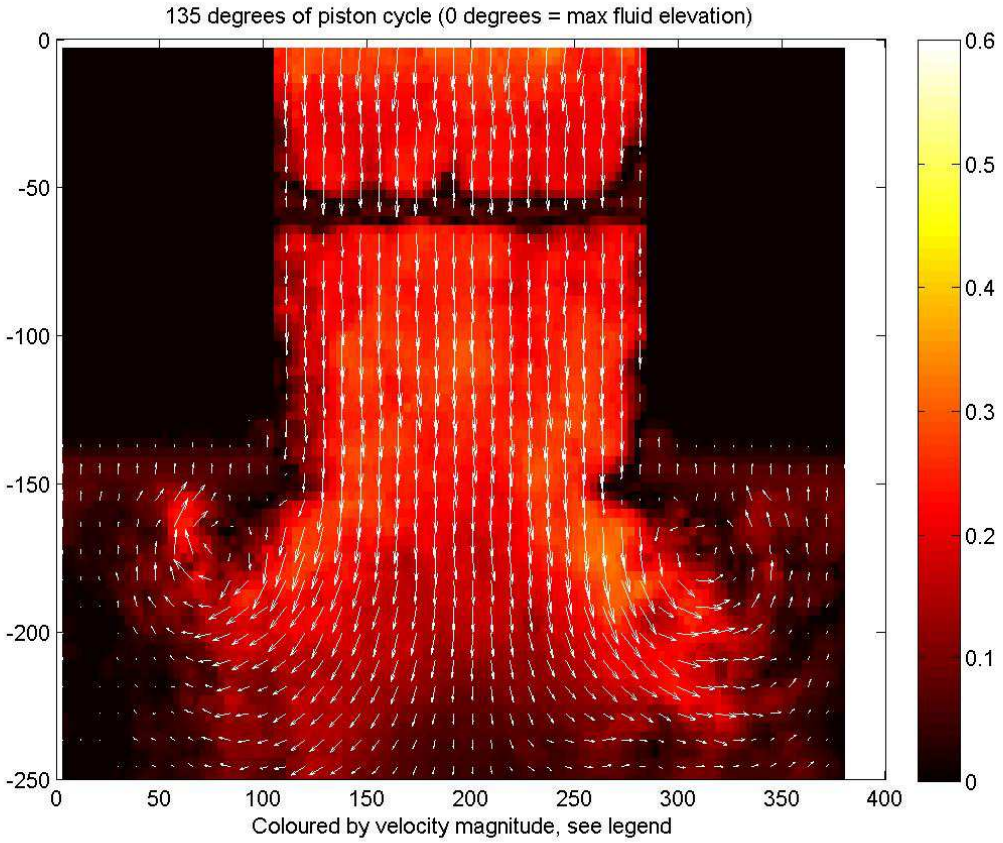
135 degrees of piston cycle (0 degrees = max fluid elevation)
0
-50
-100
-150
-200
-250
0
50
100
150
200
250
300
350
400
0.6
0.5
0.4
0.3
0.2
0.1
0
Coloured by velocity magnitude, see legend

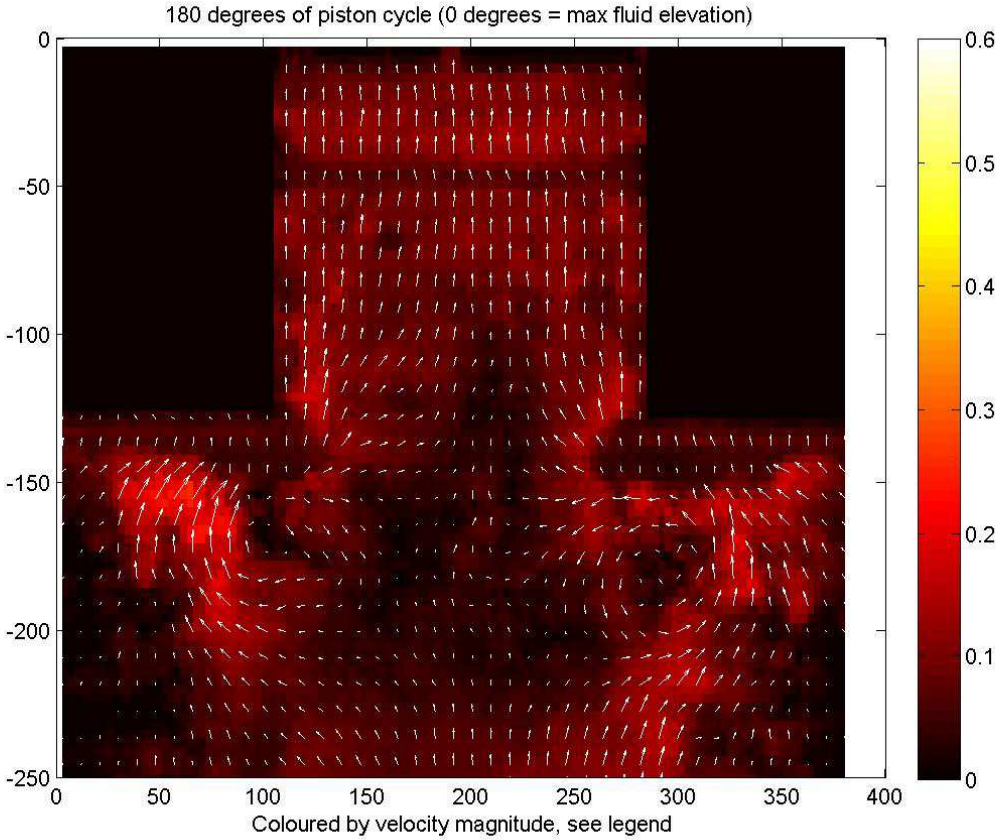
180 degrees of piston cycle (0 degrees = max fluid elevation)
0
-50
-100
-150
-200
-250
0
50
100
150
200
250
300
350
400
0.6
0.5
0.4
0.3
0.2
0.1
0
Coloured by velocity magnitude, see legend

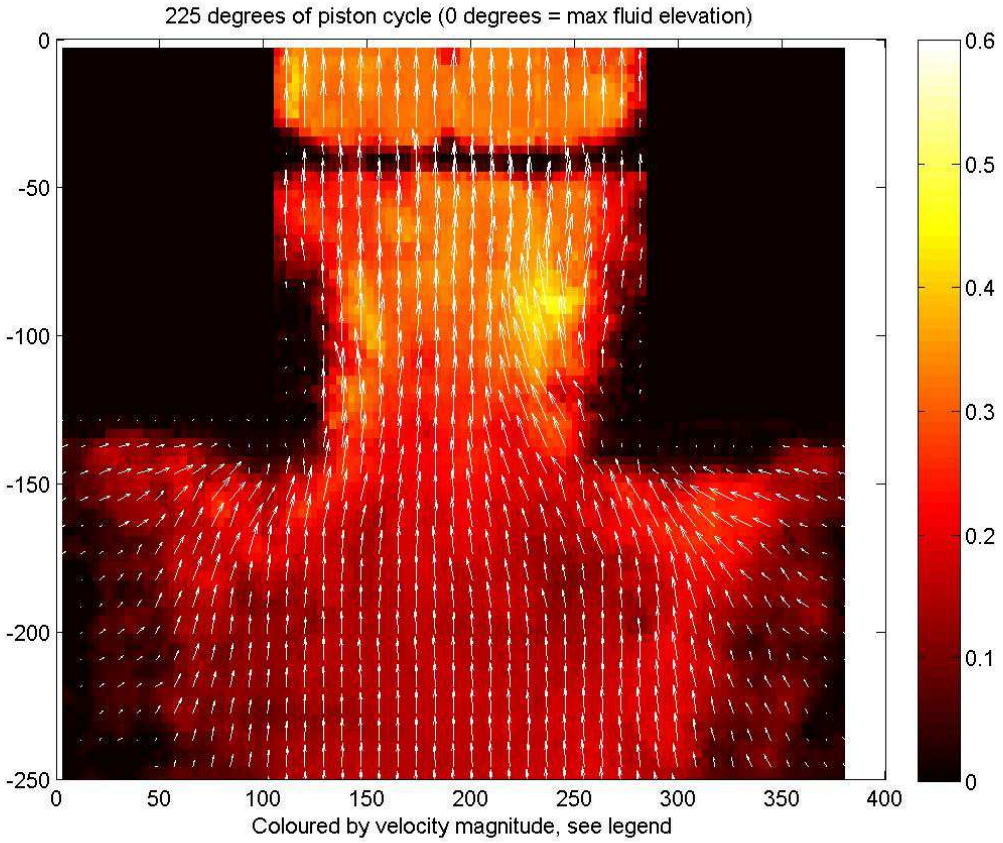
225 degrees of piston cycle (0 degrees = max fluid elevation)
0
-50
-100
-150
-200
-250
0
50
100
150
200
250
300
350
400
0.6
0.5
0.4
0.3
0.2
0.1
0
Coloured by velocity magnitude, see legend

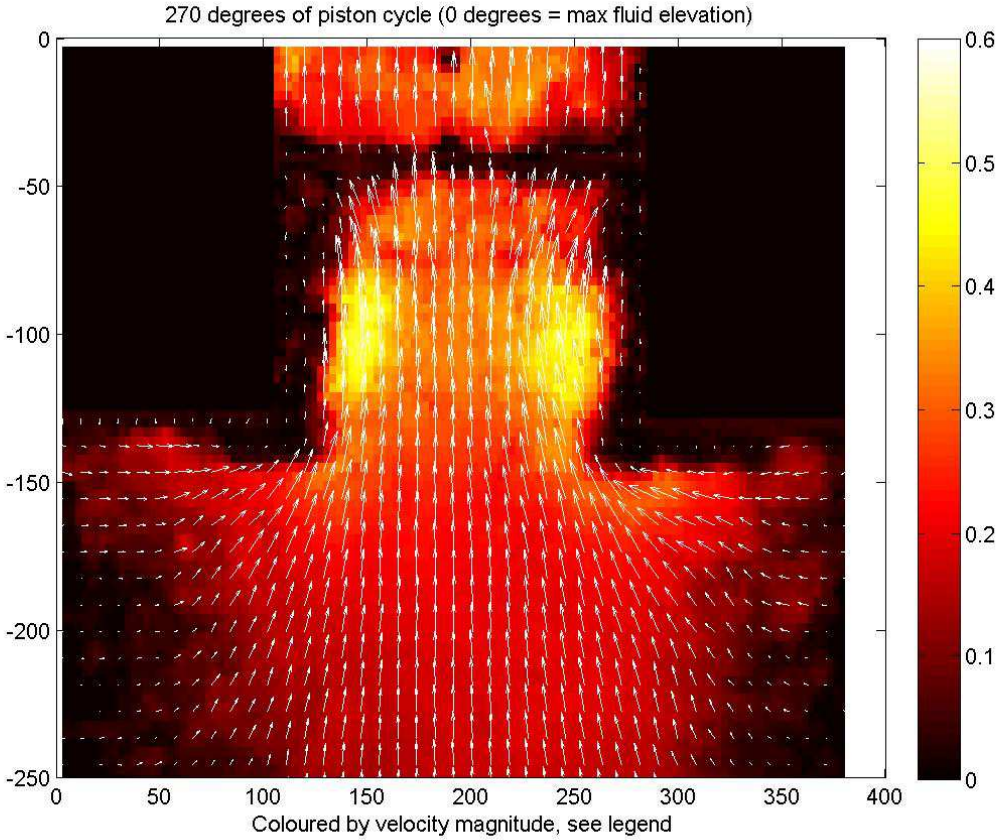
270 degrees of piston cycle (0 degrees = max fluid elevation)
0
-50
-100
-150
-200
-250
0
50
100
150
200
250
300
350
400
0.6
0.5
0.4
0.3
0.2
0.1
0
Coloured by velocity magnitude, see legend

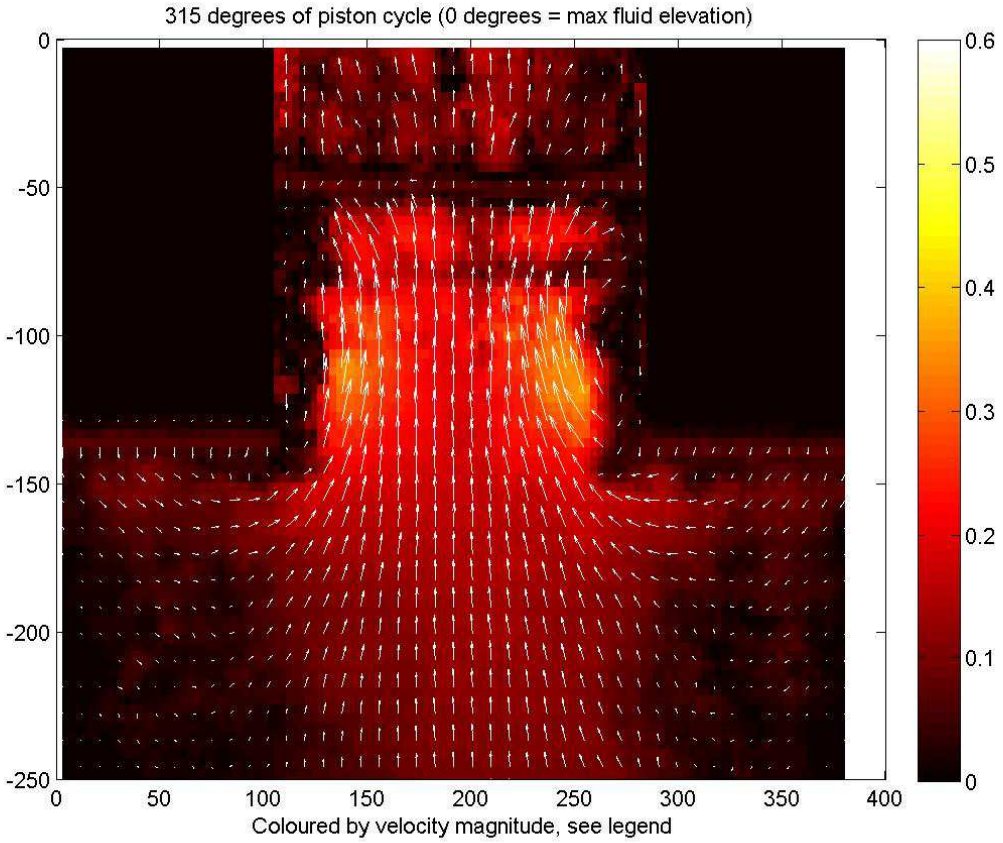
315 degrees of piston cycle (0 degrees = max fluid elevation)
0
-50
-100
-150
-200
-250
0
50
100
150
200
250
300
350
400
0.6
0.5
0.4
0.3
0.2
0.1
0
Coloured by velocity magnitude, see legend

Seven Viking, empty moonpool

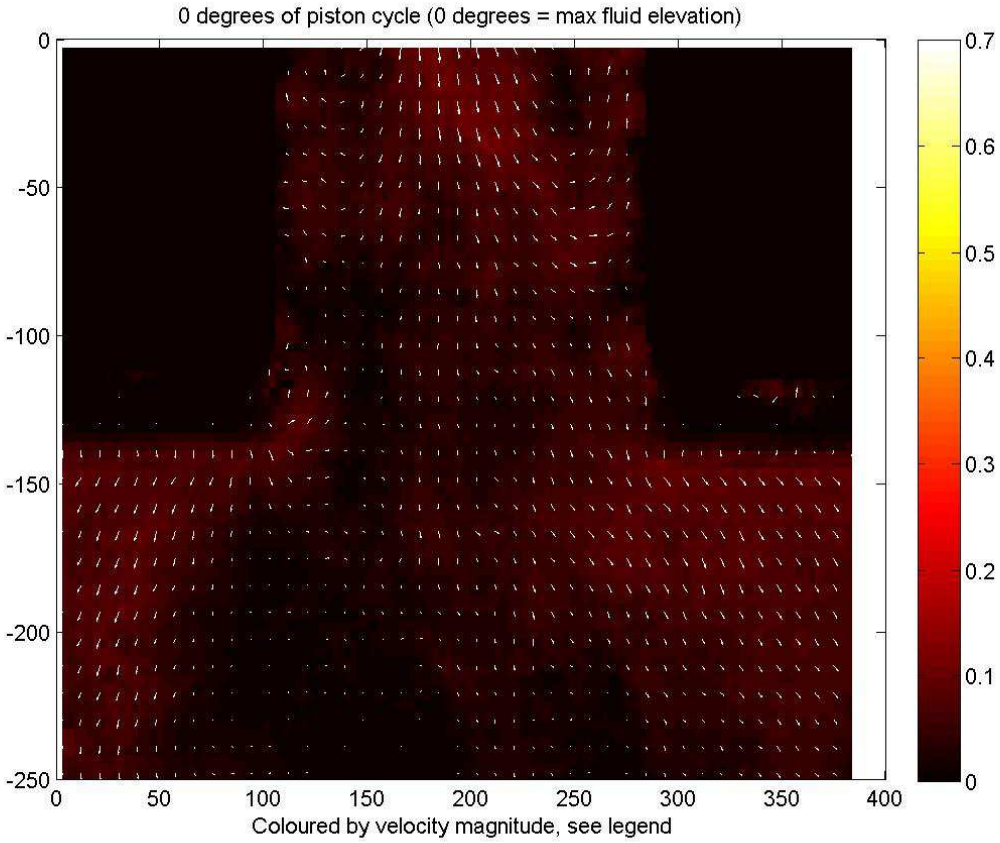

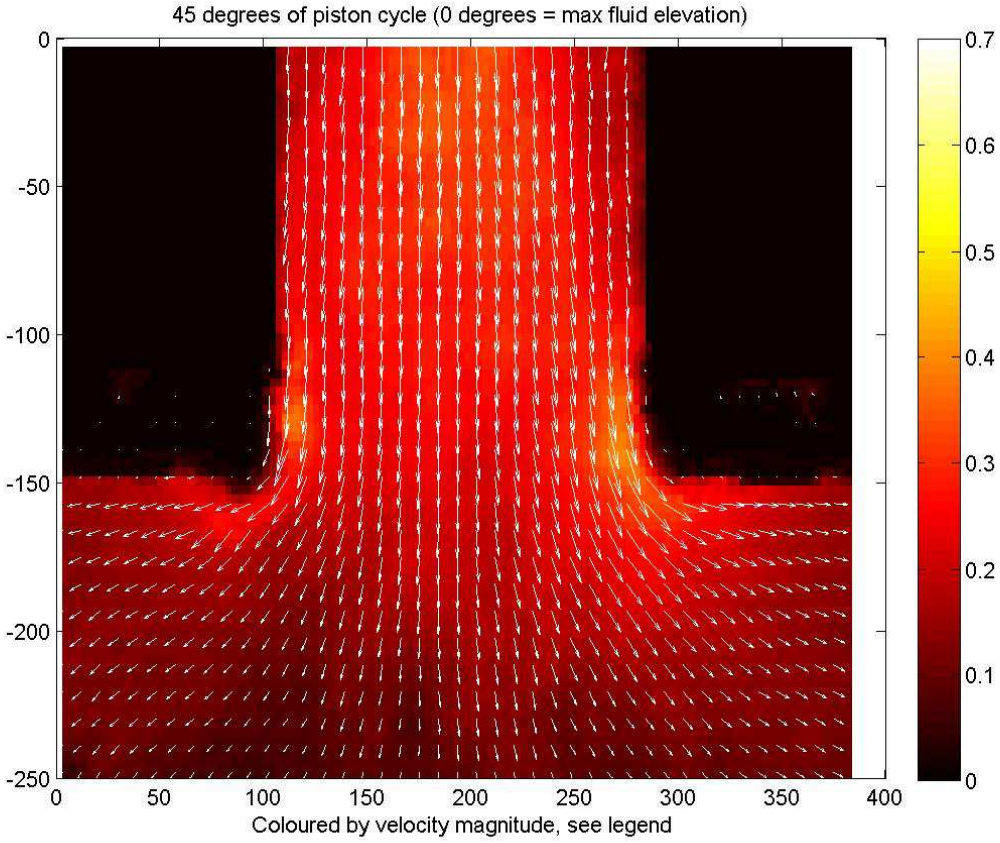

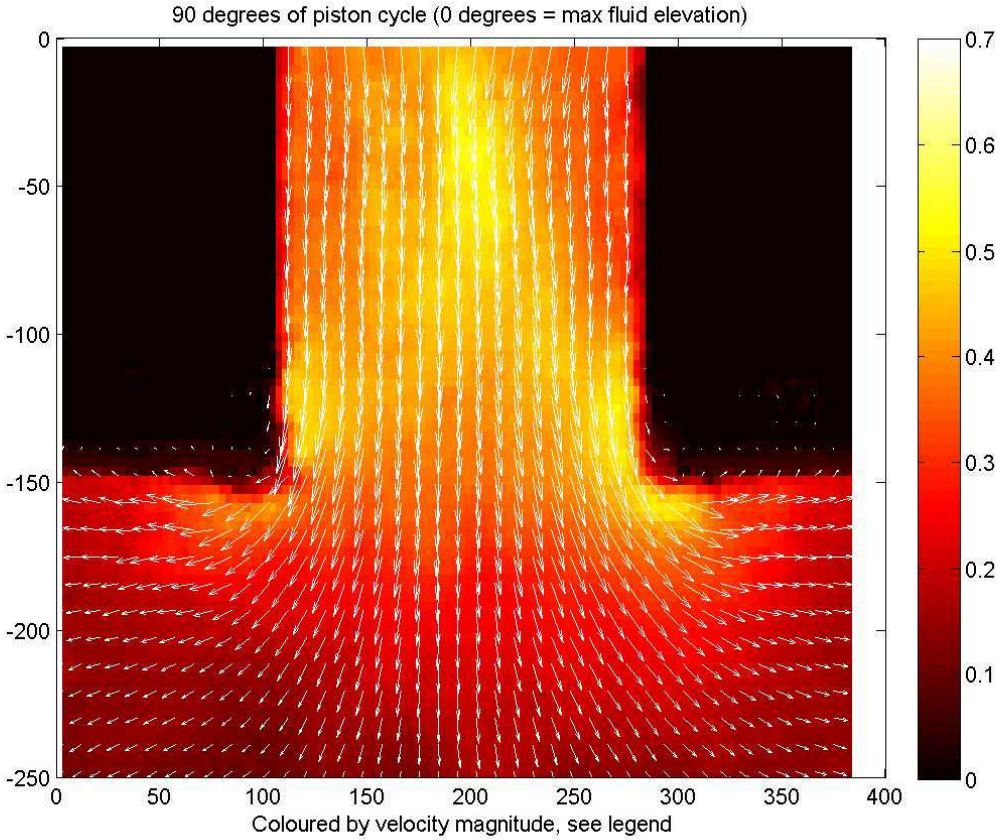
90 degrees of piston cycle (0 degrees = max fluid elevation)
0
-50
-100
-150
-200
-250
0
50
100
150
200
250
300
350
400
0.7
0.6
0.5
0.4
0.3
0.2
0.1
0
Coloured by velocity magnitude, see legend

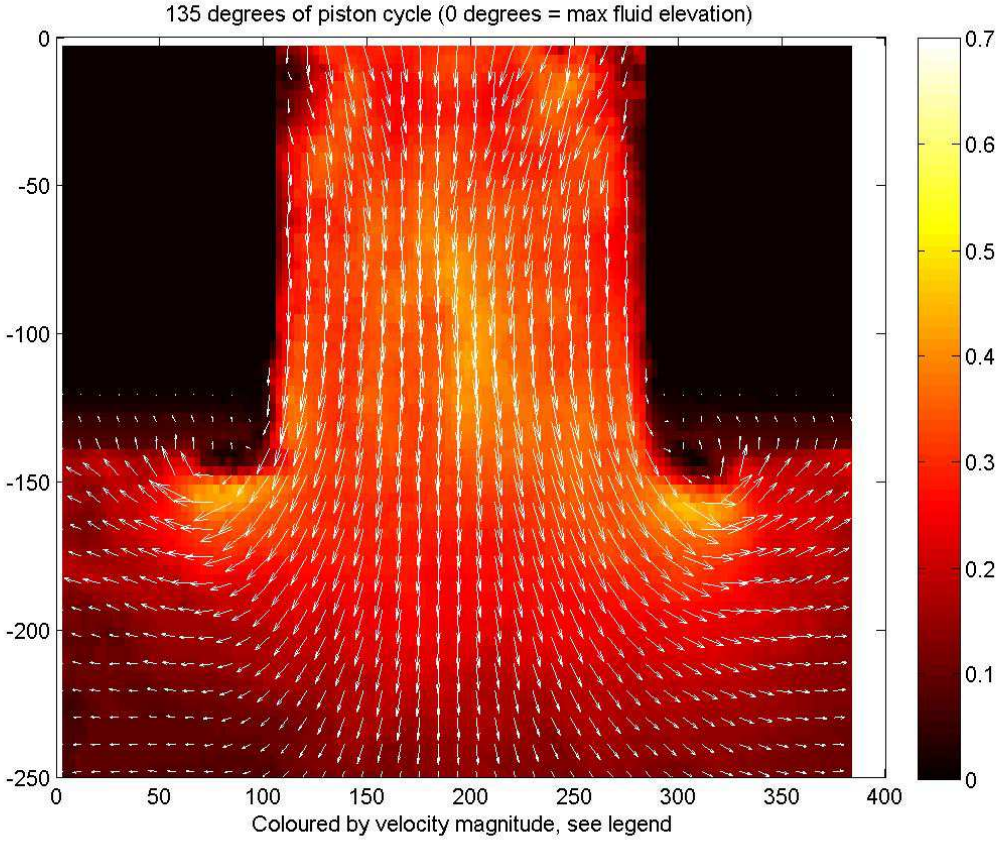
135 degrees of piston cycle (0 degrees = max fluid elevation)
0
-50
-100
-150
-200
-250
0
50
100
150
200
250
300
350
400
0.7
0.6
0.5
0.4
0.3
0.2
0.1
0
Coloured by velocity magnitude, see legend

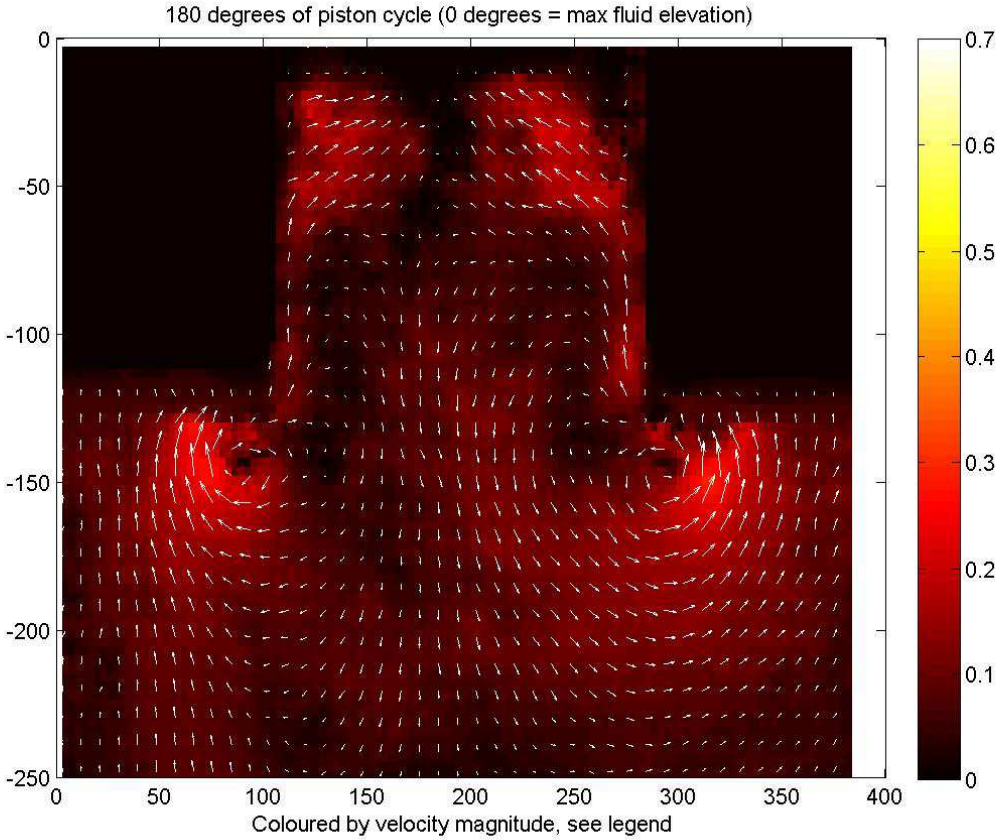
180 degrees of piston cycle (0 degrees = max fluid elevation)
0
-50
-100
-150
-200
-250
0
50
100
150
200
250
300
350
400
0.7
0.6
0.5
0.4
0.3
0.2
0.1
0
Coloured by velocity magnitude, see legend

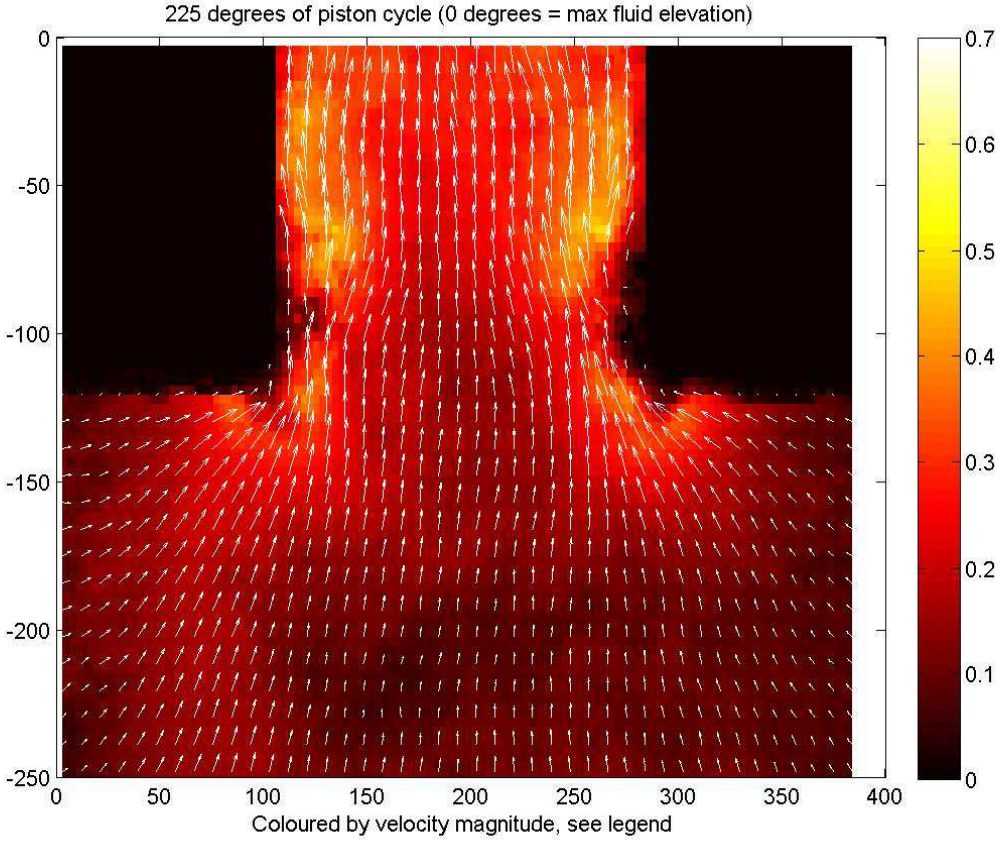
225 degrees of piston cycle (0 degrees = max fluid elevation)
0
-50
-100
-150
-200
-250
0
50
100
150
200
250
300
350
400
0.7
0.6
0.5
0.4
0.3
0.2
0.1
0
Coloured by velocity magnitude, see legend

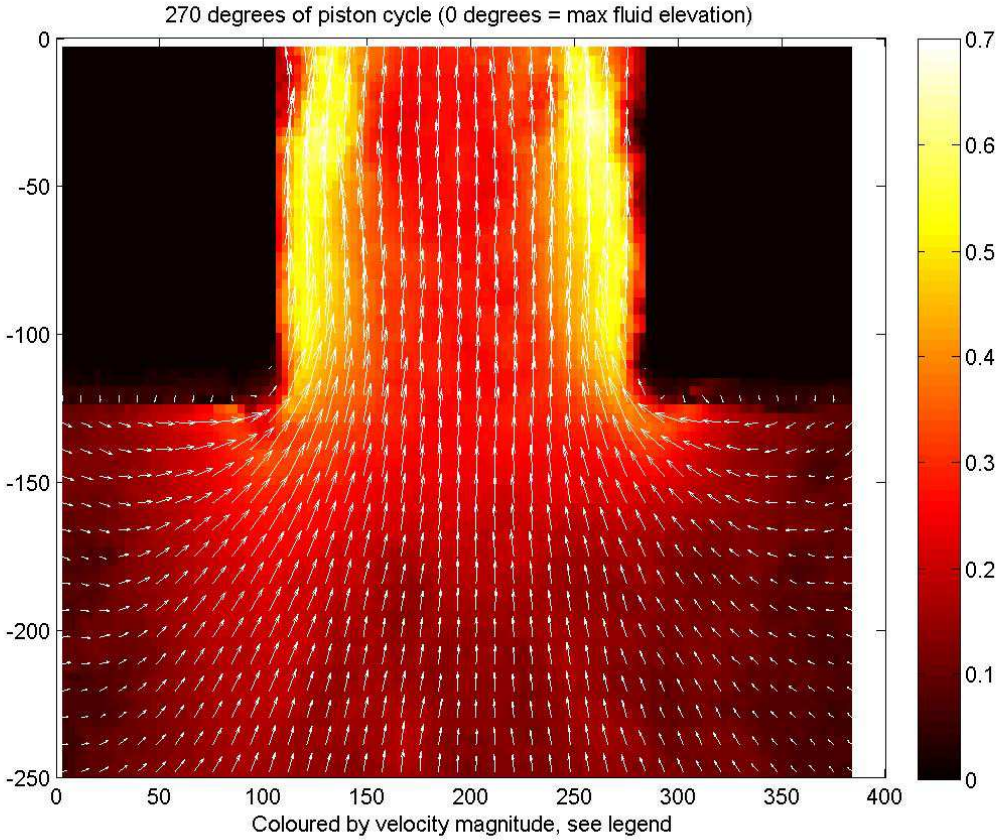
270 degrees of piston cycle (0 degrees = max fluid elevation)
0
-50
-100
-150
-200
-250
0
50
100
150
200
250
300
350
400
0.7
0.6
0.5
0.4
0.3
0.2
0.1
0
Coloured by velocity magnitude, see legend

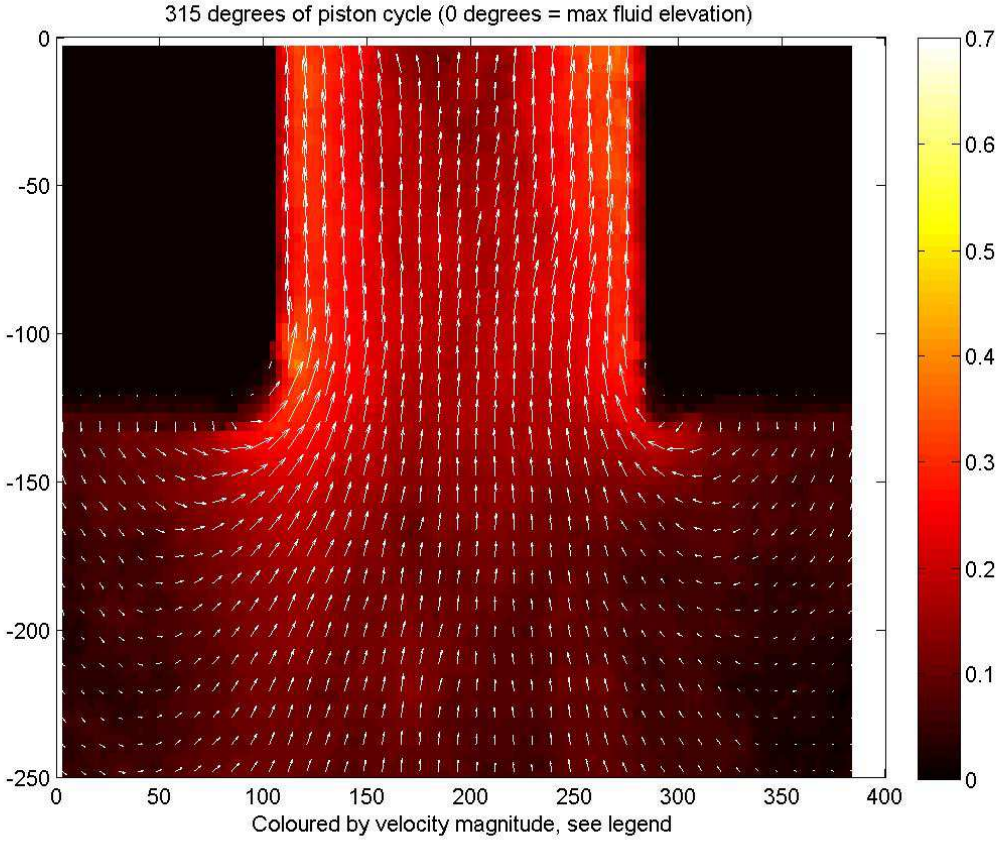
315 degrees of piston cycle (0 degrees = max fluid elevation)
0
-50
-100
-150
-200
-250
0
50
100
150
200
250
300
350
400
0.7
0.6
0.5
0.4
0.3
0.2
0.1
0
Coloured by velocity magnitude, see legend

Seven Viking, small object

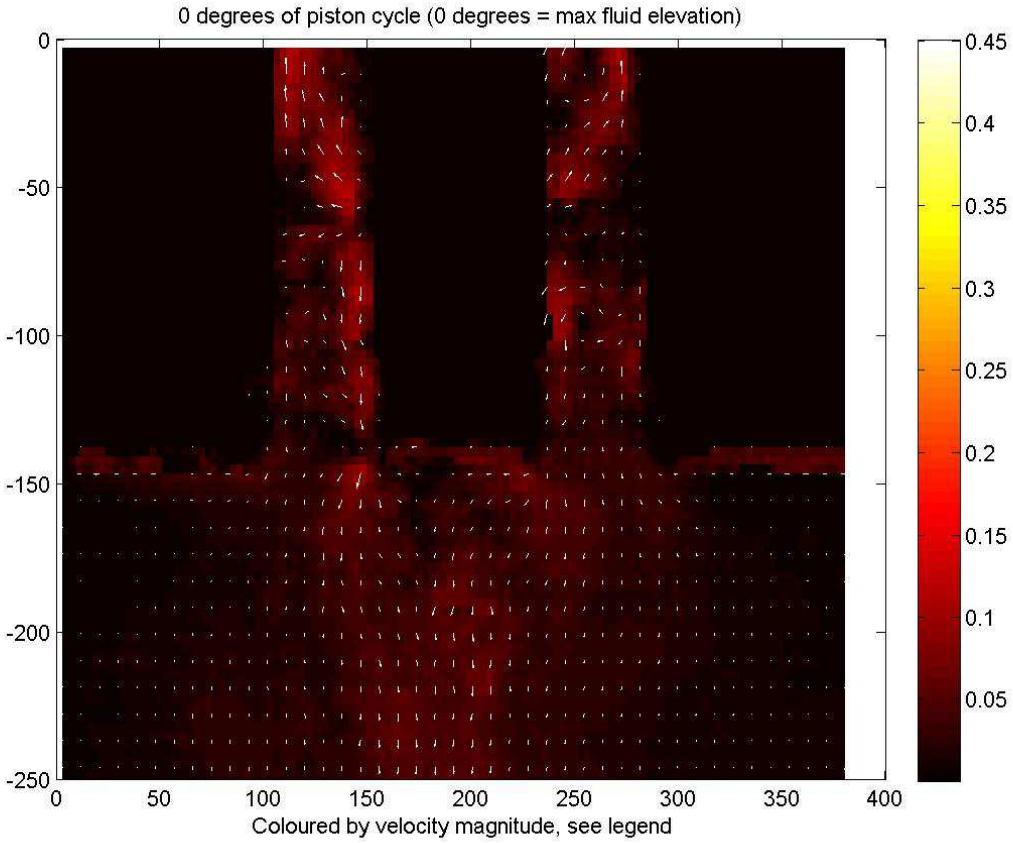

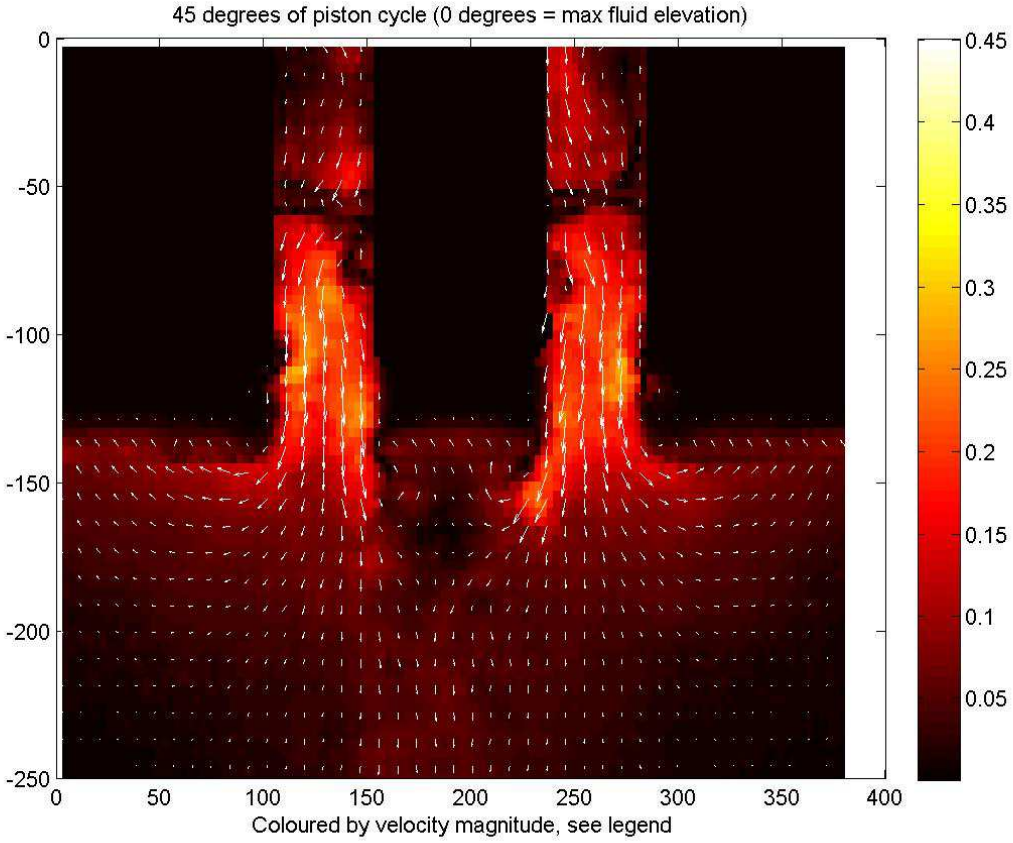

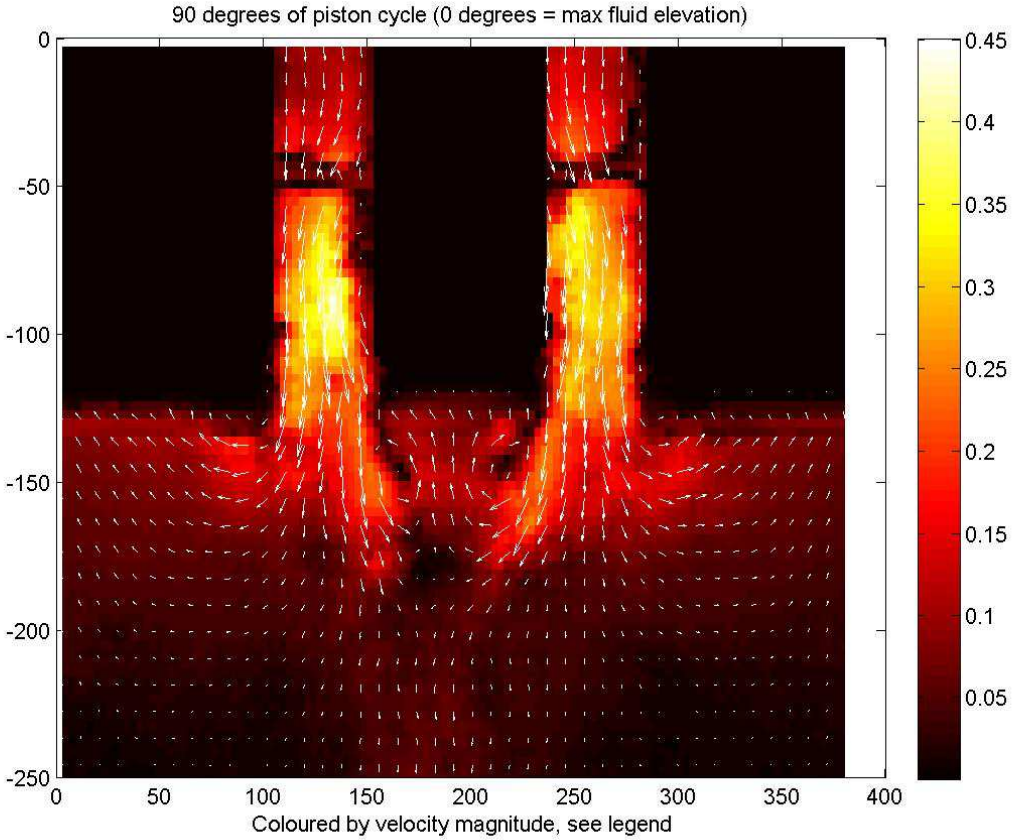
90 degrees of piston cycle (0 degrees = max fluid elevation)
0
-50
-100
-150
-200
-250
0
50
100
150
200
250
300
350
400
0.45
0.4
0.35
0.3
0.25
0.2
0.15
0.1
0.05
Coloured by velocity magnitude, see legend

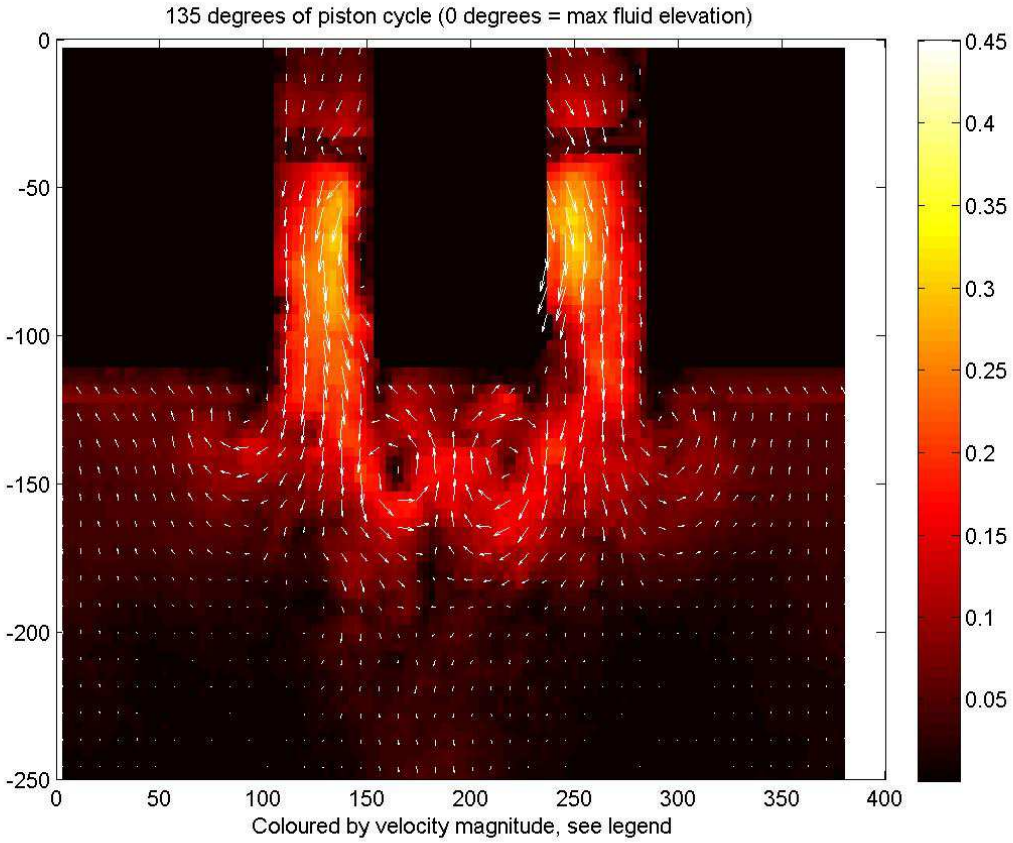
135 degrees of piston cycle (0 degrees = max fluid elevation)
0
-50
-100
-150
-200
-250
0
50
100
150
200
250
300
350
400
0.45
0.4
0.35
0.3
0.25
0.2
0.15
0.1
0.05
Coloured by velocity magnitude, see legend

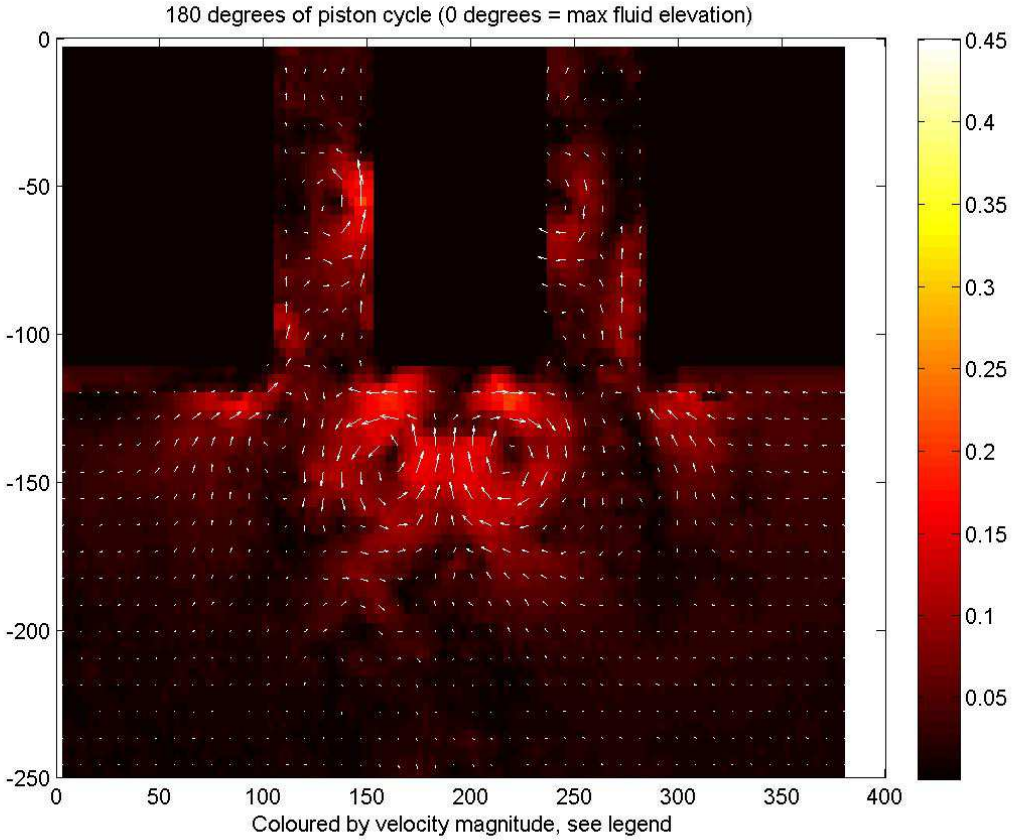
180 degrees of piston cycle (0 degrees = max fluid elevation)
0
-50
-100
-150
-200
-250
0
50
100
150
200
250
300
350
400
0.45
0.4
0.35
0.3
0.25
0.2
0.15
0.1
0.05
Coloured by velocity magnitude, see legend

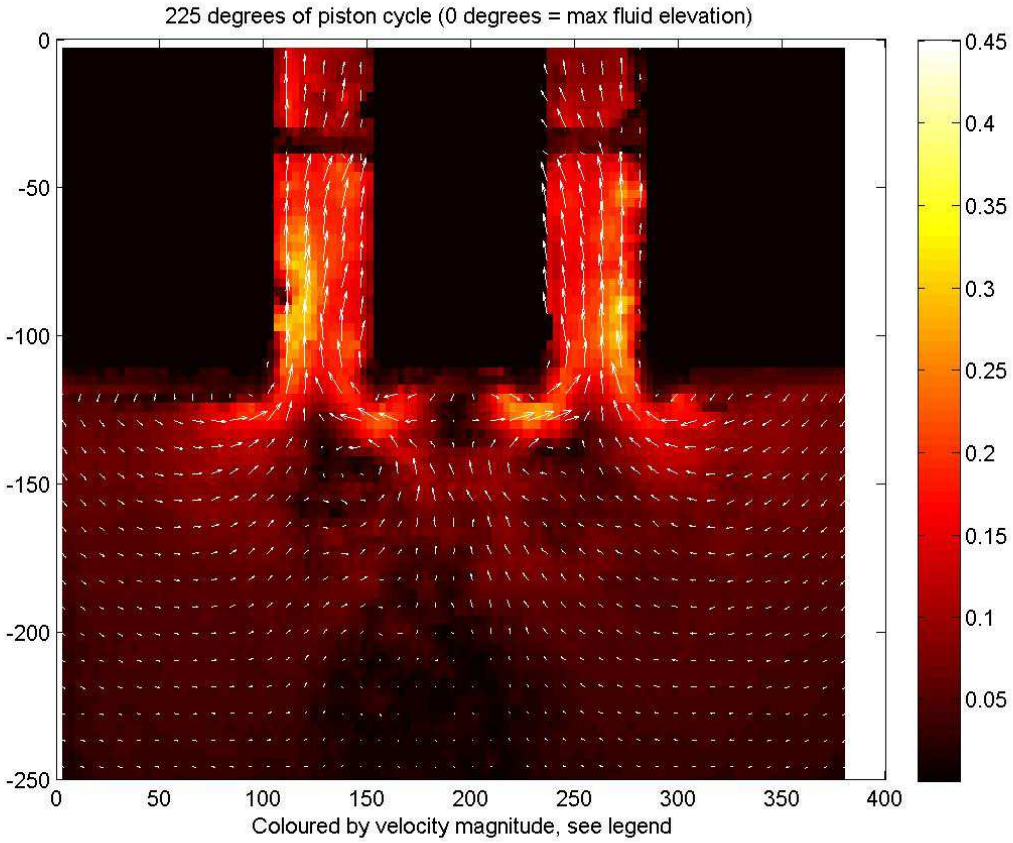
225 degrees of piston cycle (0 degrees = max fluid elevation)
0
-50
-100
-150
-200
-250
0
50
100
150
200
250
300
350
400
0.45
0.4
0.35
0.3
0.25
0.2
0.15
0.1
0.05
Coloured by velocity magnitude, see legend

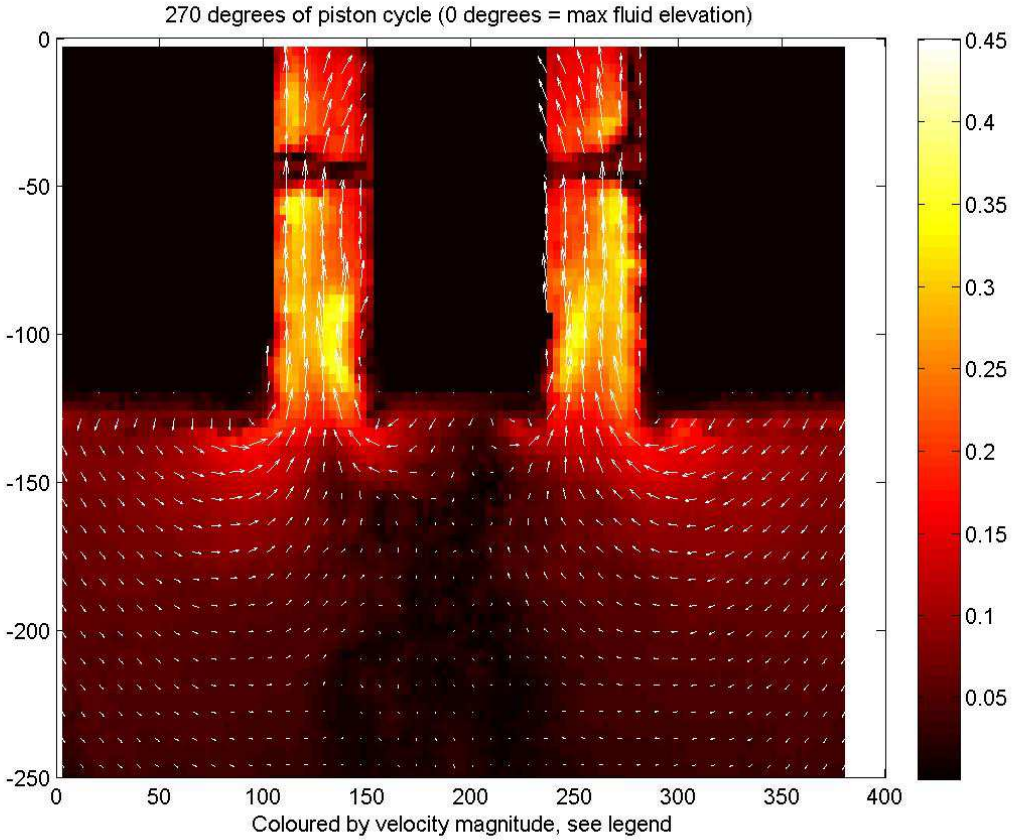
270 degrees of piston cycle (0 degrees = max fluid elevation)
0
-50
-100
-150
-200
-250
0
50
100
150
200
250
300
350
400
0.45
0.4
0.35
0.3
0.25
0.2
0.15
0.1
0.05
Coloured by velocity magnitude, see legend

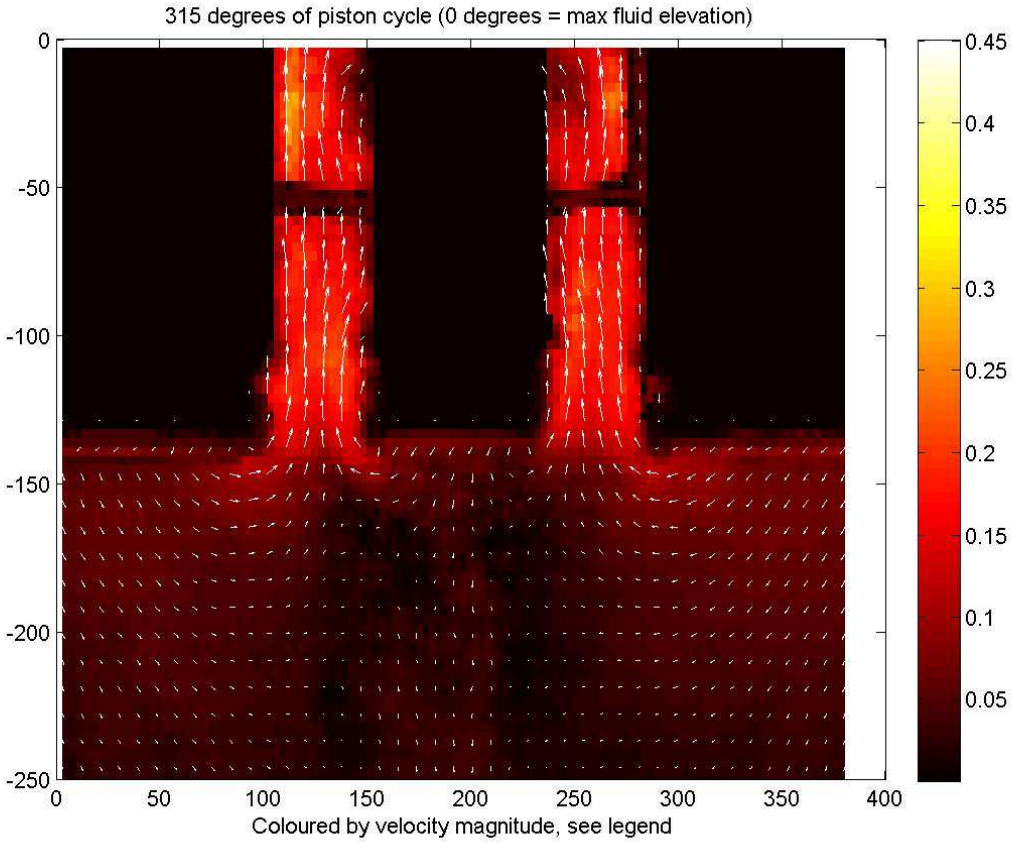
315 degrees of piston cycle (0 degrees = max fluid elevation)
0
-50
-100
-150
-200
-250
0
50
100
150
200
250
300
350
400
0.45
0.4
0.35
0.3
0.25
0.2
0.15
0.1
0.05
Coloured by velocity magnitude, see legend

Seven Viking, large object

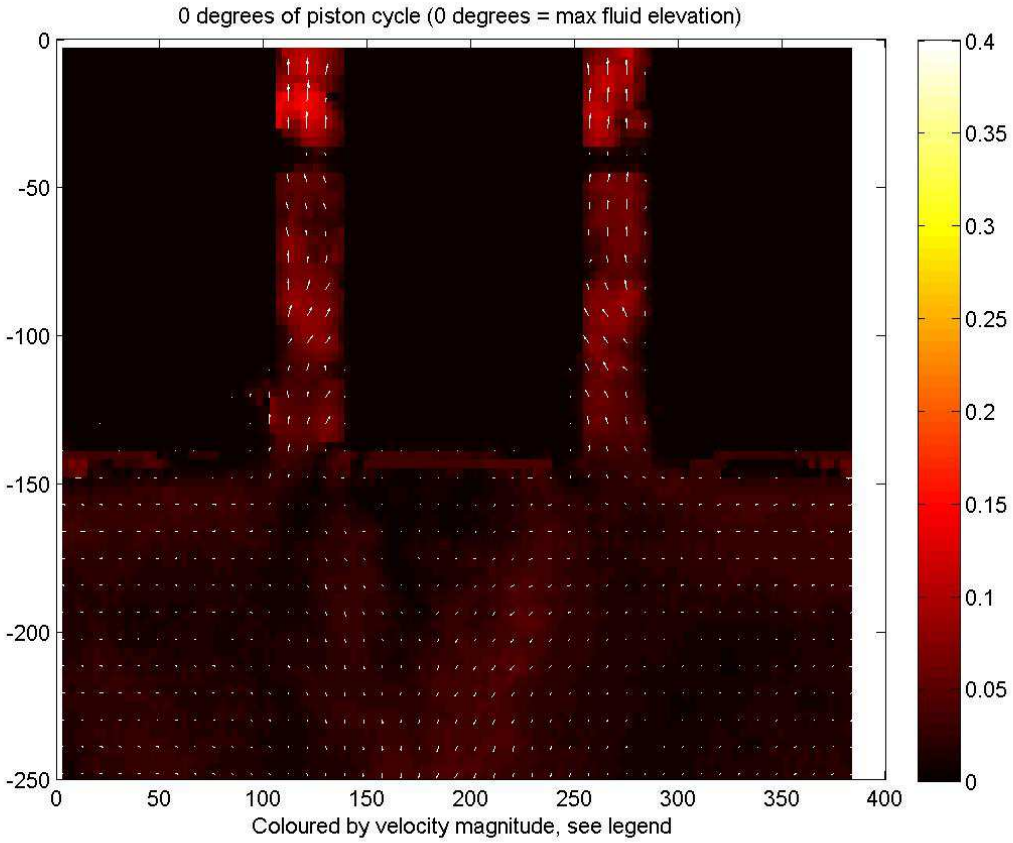

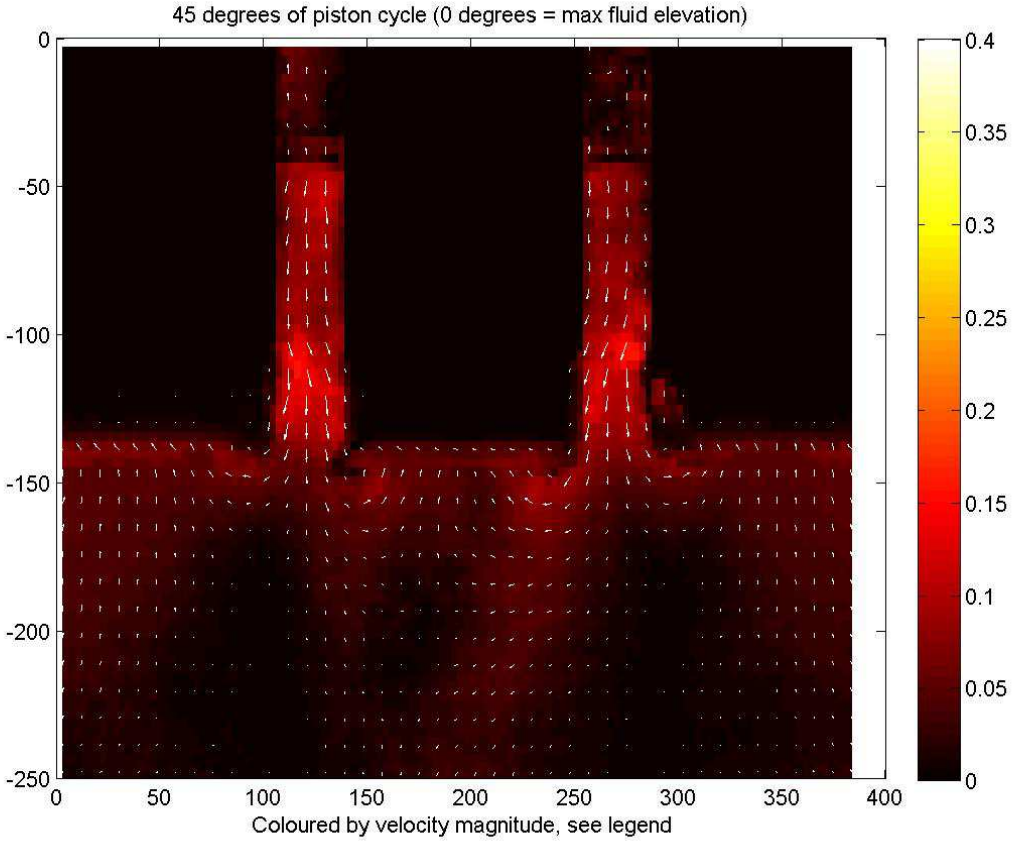

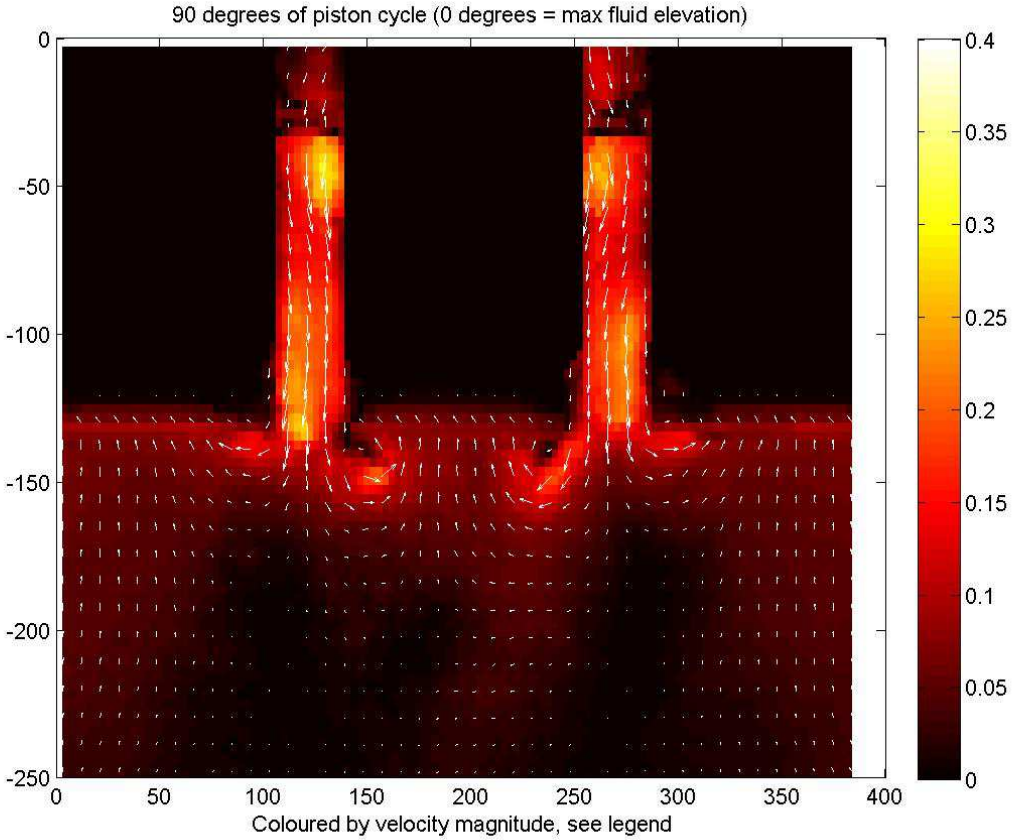
90 degrees of piston cycle (0 degrees = max fluid elevation)
0
-50
-100
-150
-200
-250
0
50
100
150
200
250
300
350
400
0.4
0.35
0.3
0.25
0.2
0.15
0.1
0.05
0
Coloured by velocity magnitude, see legend

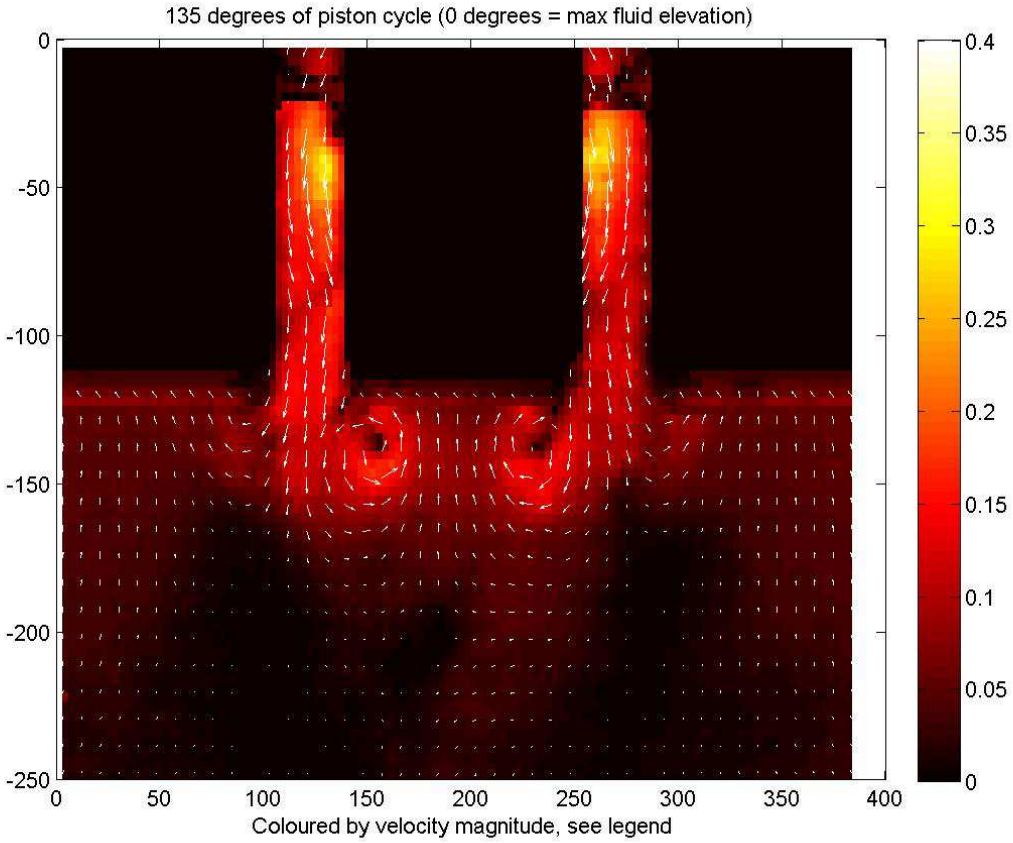
135 degrees of piston cycle (0 degrees = max fluid elevation)
0
-50
-100
-150
-200
-250
0
50
100
150
200
250
300
350
400
0.4
0.35
0.3
0.25
0.2
0.15
0.1
0.05
0
Coloured by velocity magnitude, see legend

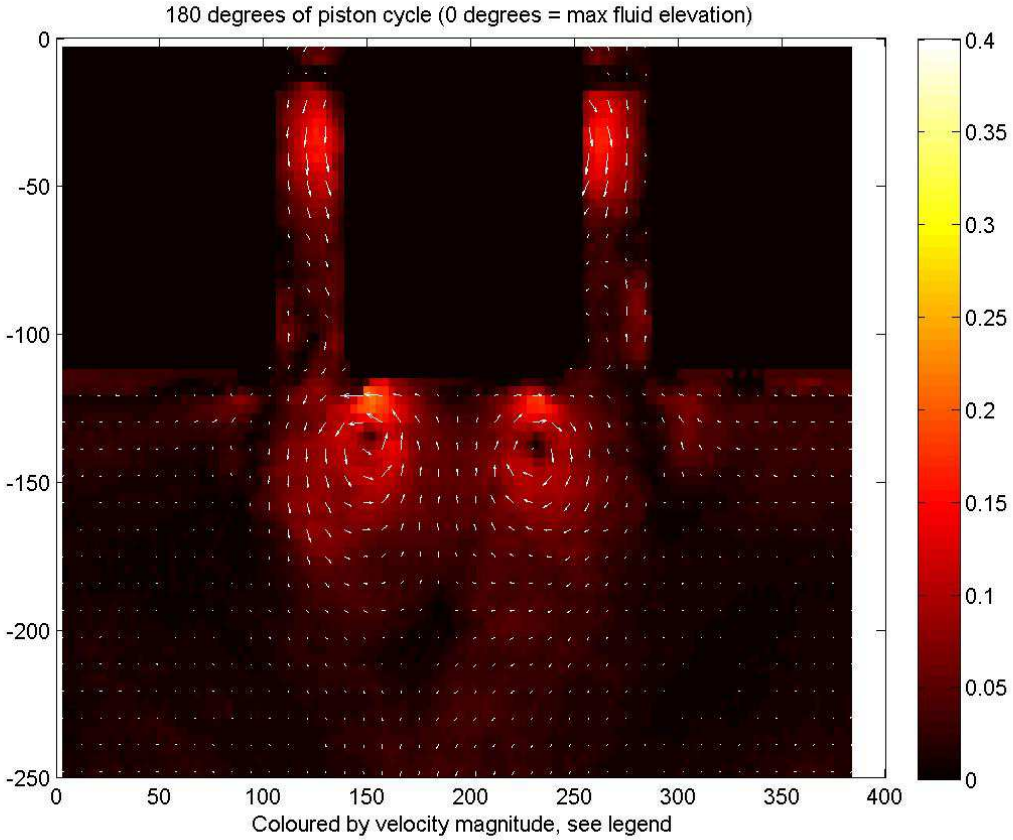
180 degrees of piston cycle (0 degrees = max fluid elevation)
0
-50
-100
-150
-200
-250
0
50
100
150
200
250
300
350
400
0.4
0.35
0.3
0.25
0.2
0.15
0.1
0.05
0
Coloured by velocity magnitude, see legend

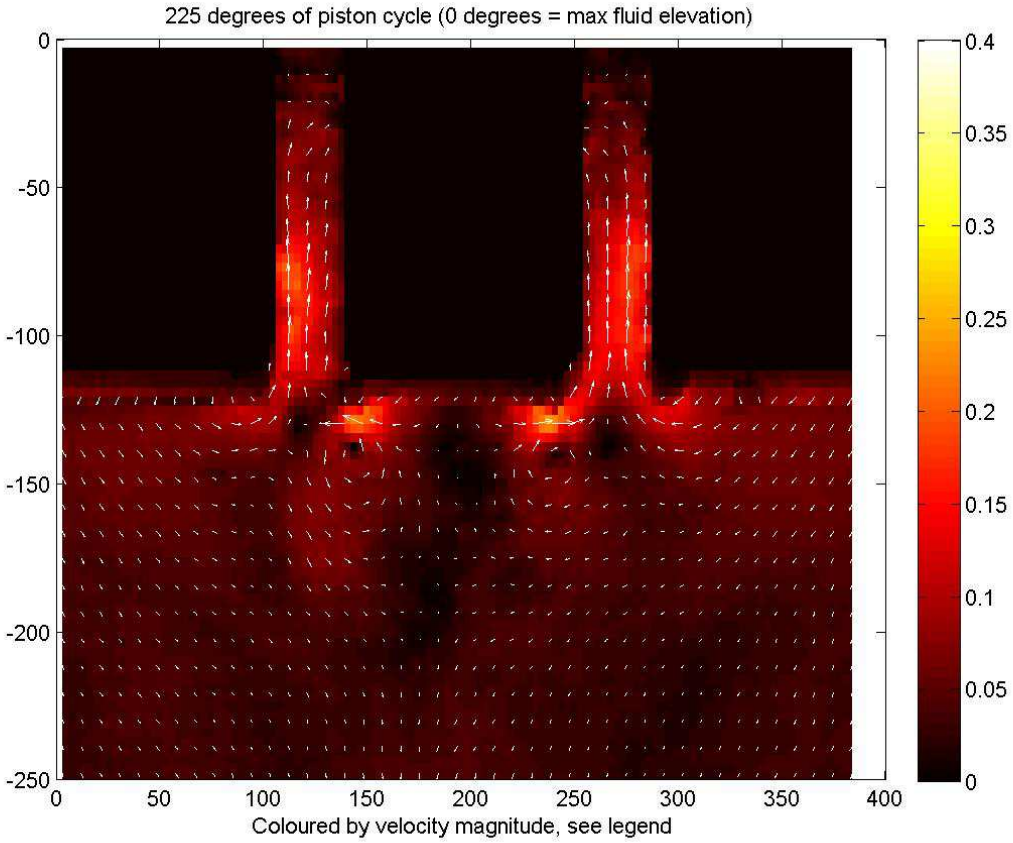
225 degrees of piston cycle (0 degrees = max fluid elevation)
0
-50
-100
-150
-200
-250
0
50
100
150
200
250
300
350
400
0.4
0.35
0.3
0.25
0.2
0.15
0.1
0.05
0
Coloured by velocity magnitude, see legend

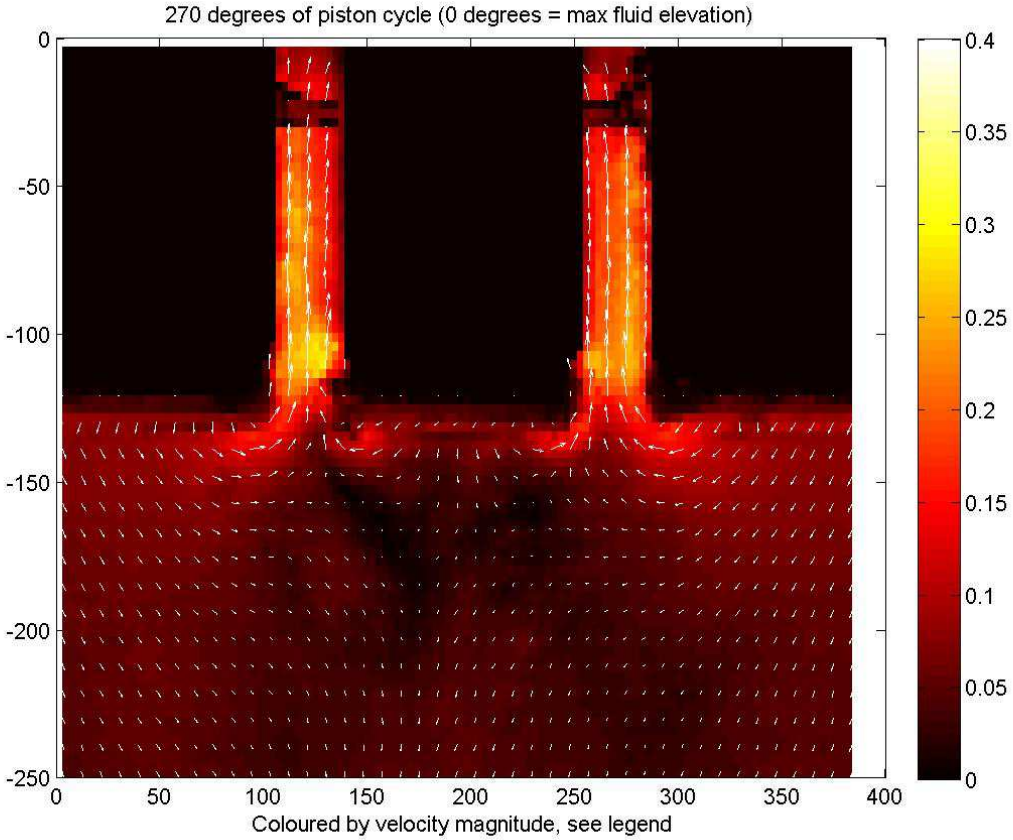
270 degrees of piston cycle (0 degrees = max fluid elevation)
0
-50
-100
-150
-200
-250
0
50
100
150
200
250
300
350
400
0.4
0.35
0.3
0.25
0.2
0.15
0.1
0.05
0
Coloured by velocity magnitude, see legend

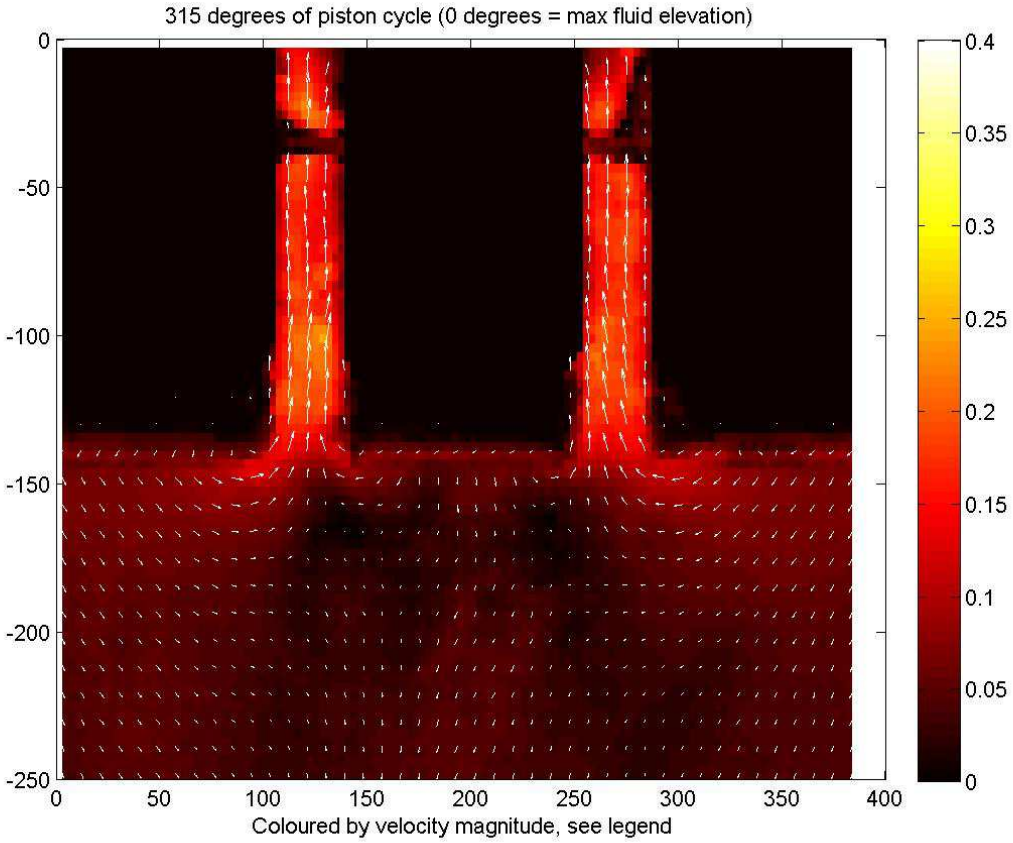
315 degrees of piston cycle (0 degrees = max fluid elevation)
0
-50
-100
-150
-200
-250
0
50
100
150
200
250
300
350
400
0.4
0.35
0.3
0.25
0.2
0.15
0.1
0.05
0
Coloured by velocity magnitude, see legend

Velocity profiles at moonpool inlet

The plots show snapshots of the velocity profiles at the moonpool inlet over one cycle.

Base case

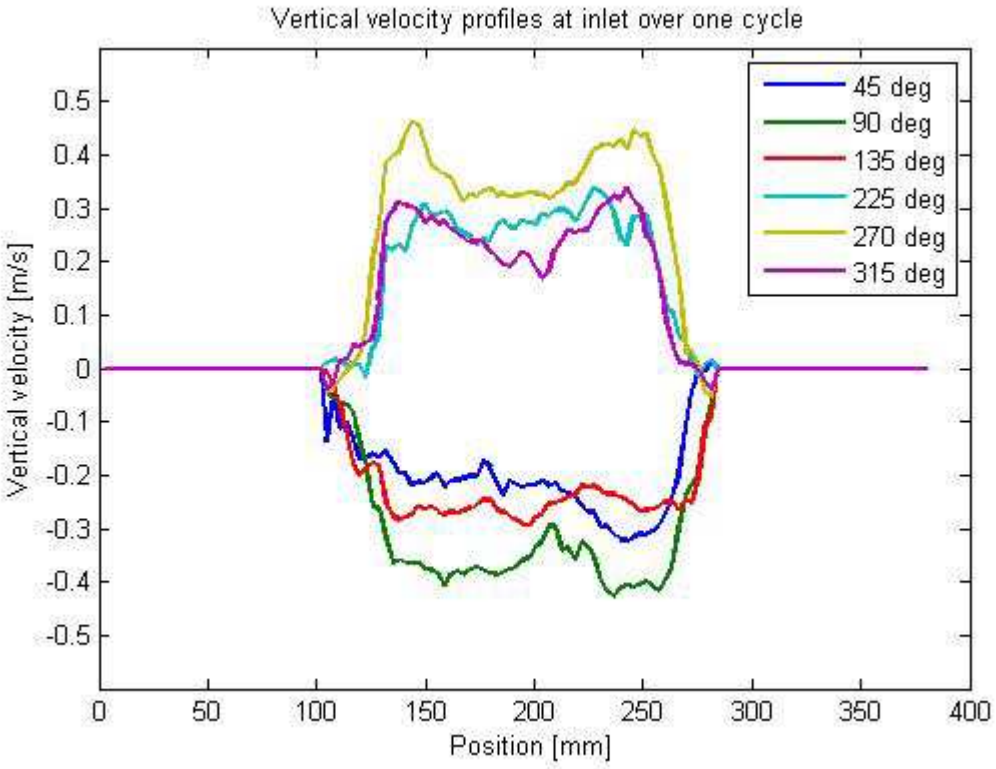

Seven Viking, empty

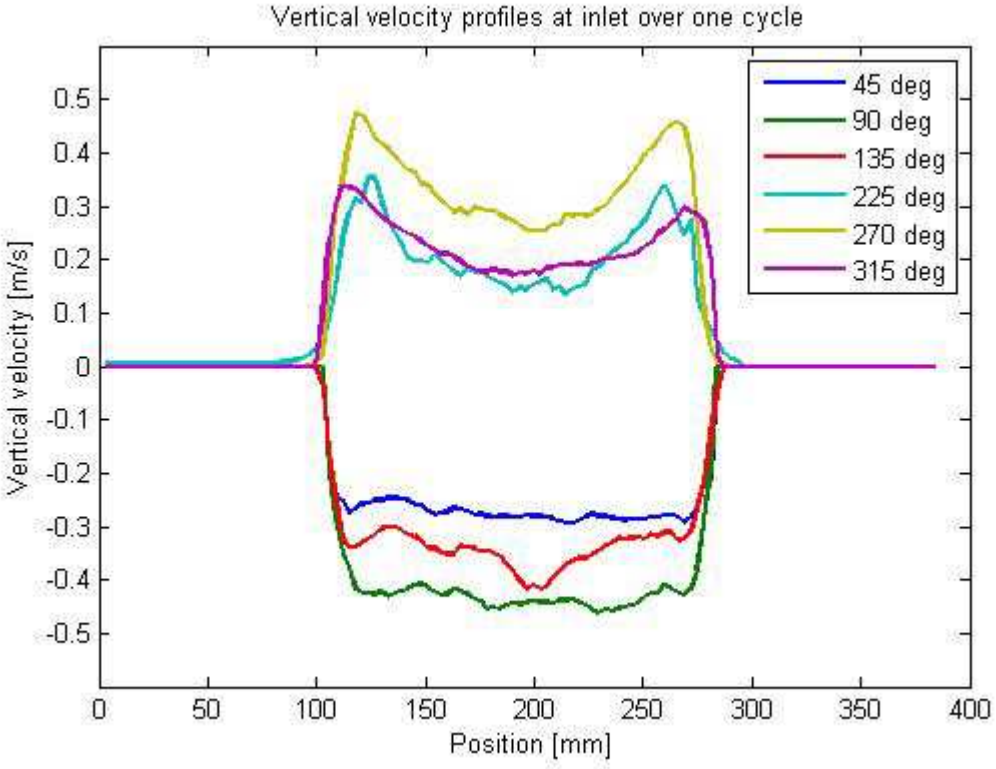

Seven Viking, small object

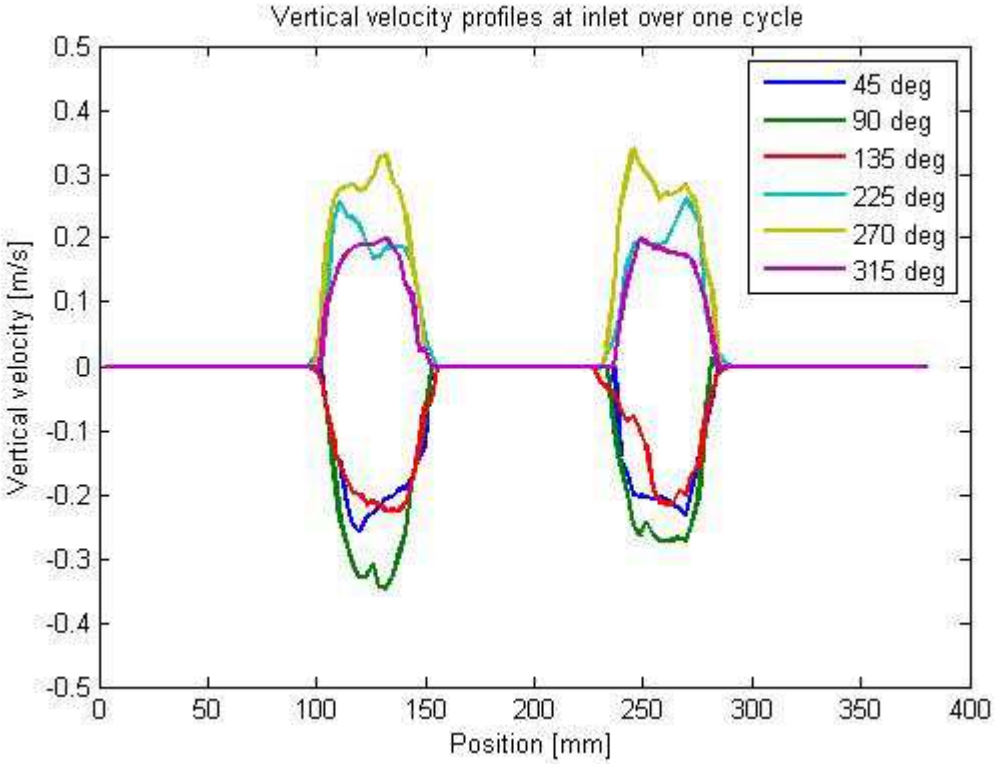

Seven Viking, large object

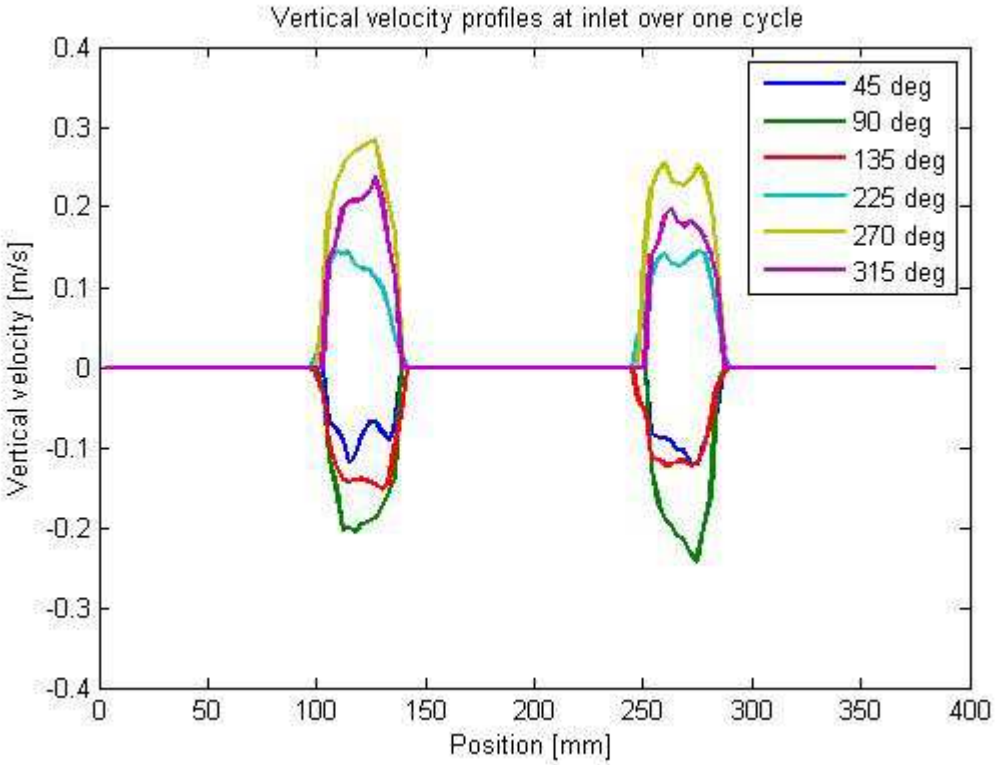

Vector plots, Seven Viking empty, without phase-averaging

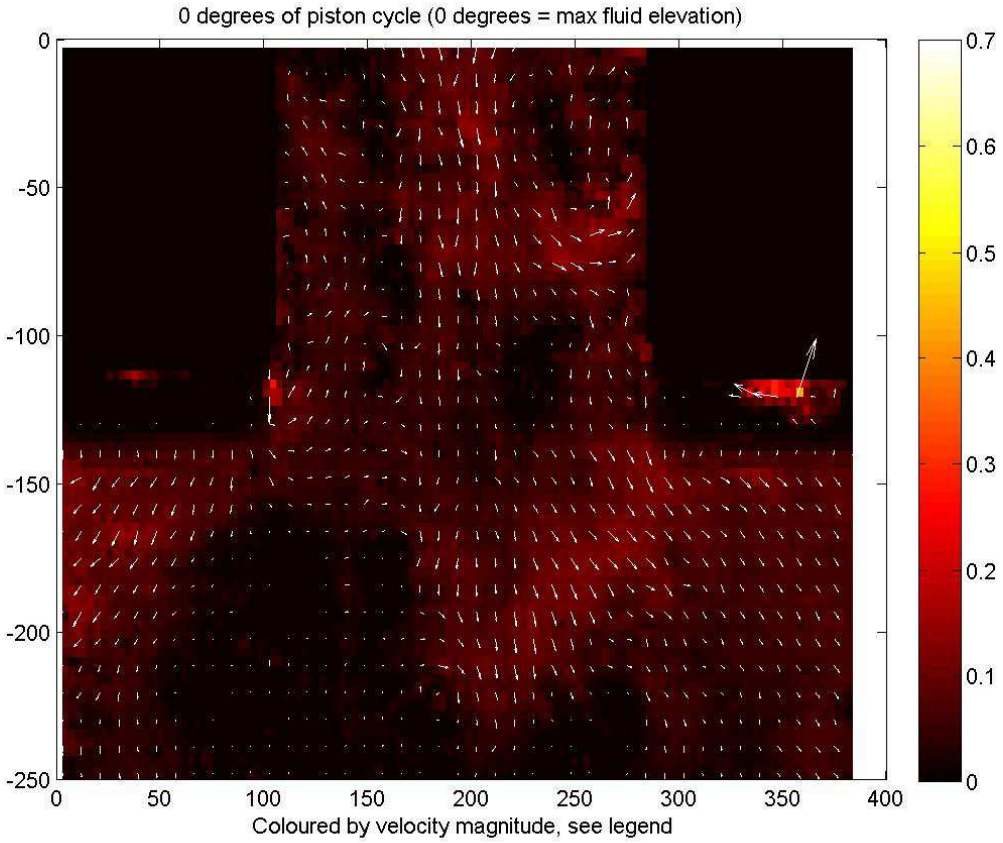

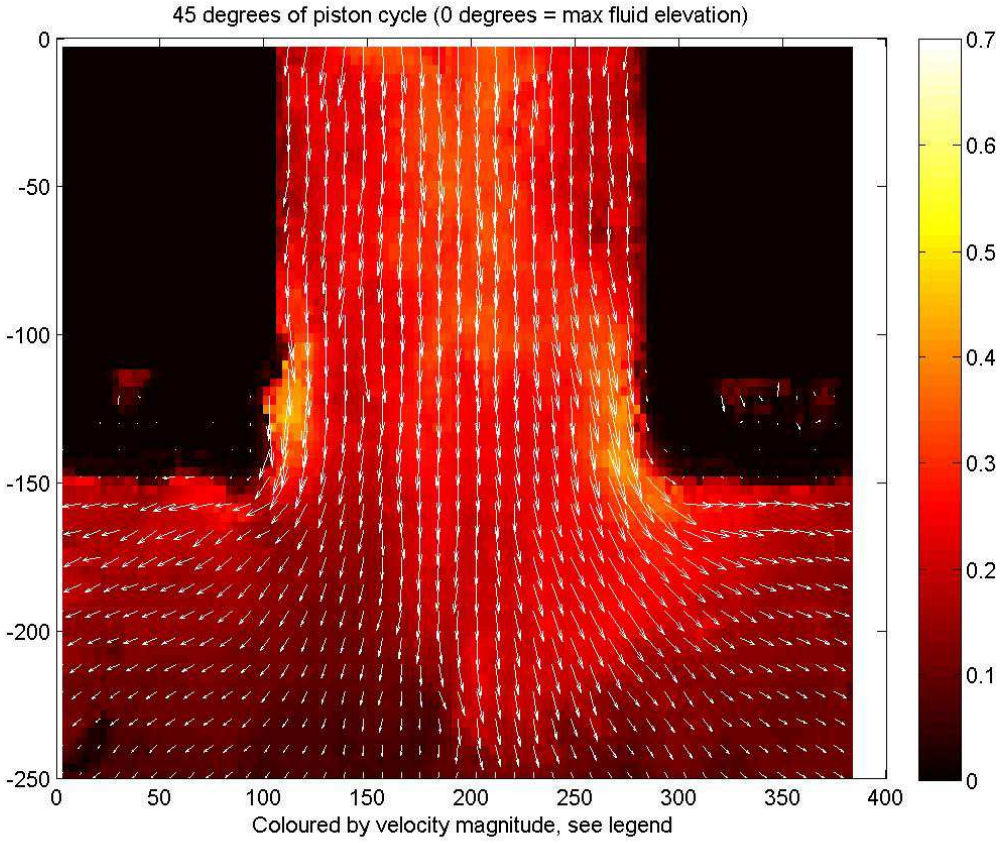

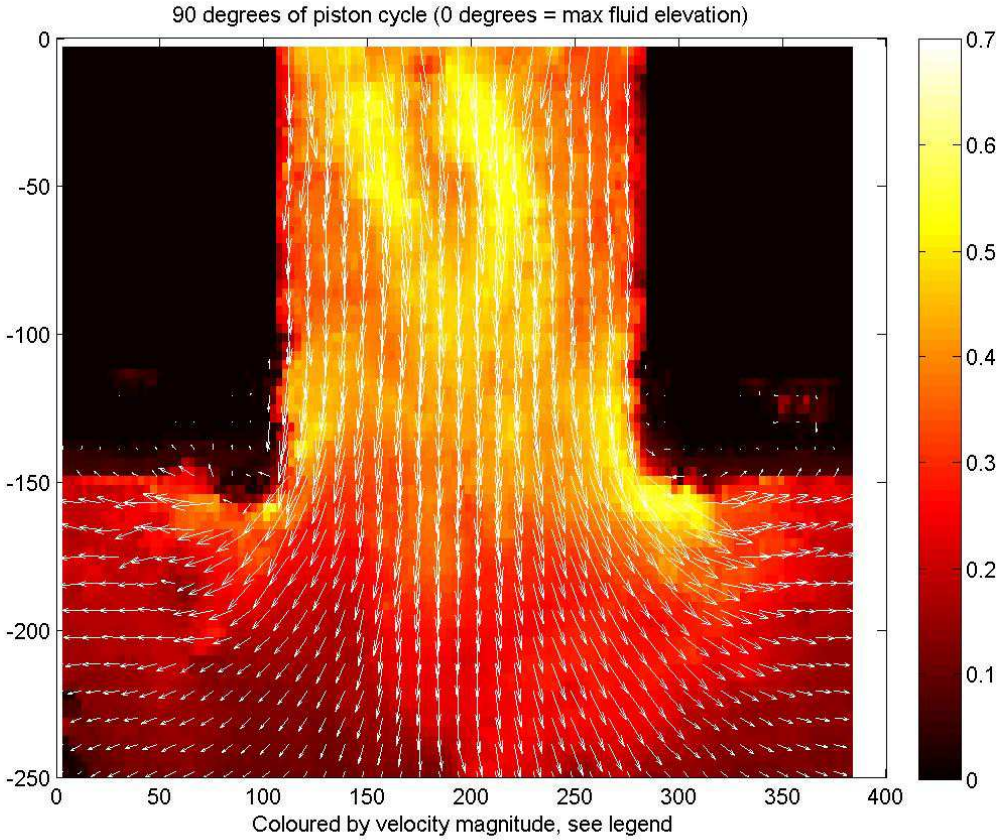
90 degrees of piston cycle (0 degrees = max fluid elevation)
0
-50
-100
-150
-200
-250
0
50
100
150
200
250
300
350
400
0.7
0.6
0.5
0.4
0.3
0.2
0.1
0
Coloured by velocity magnitude, see legend

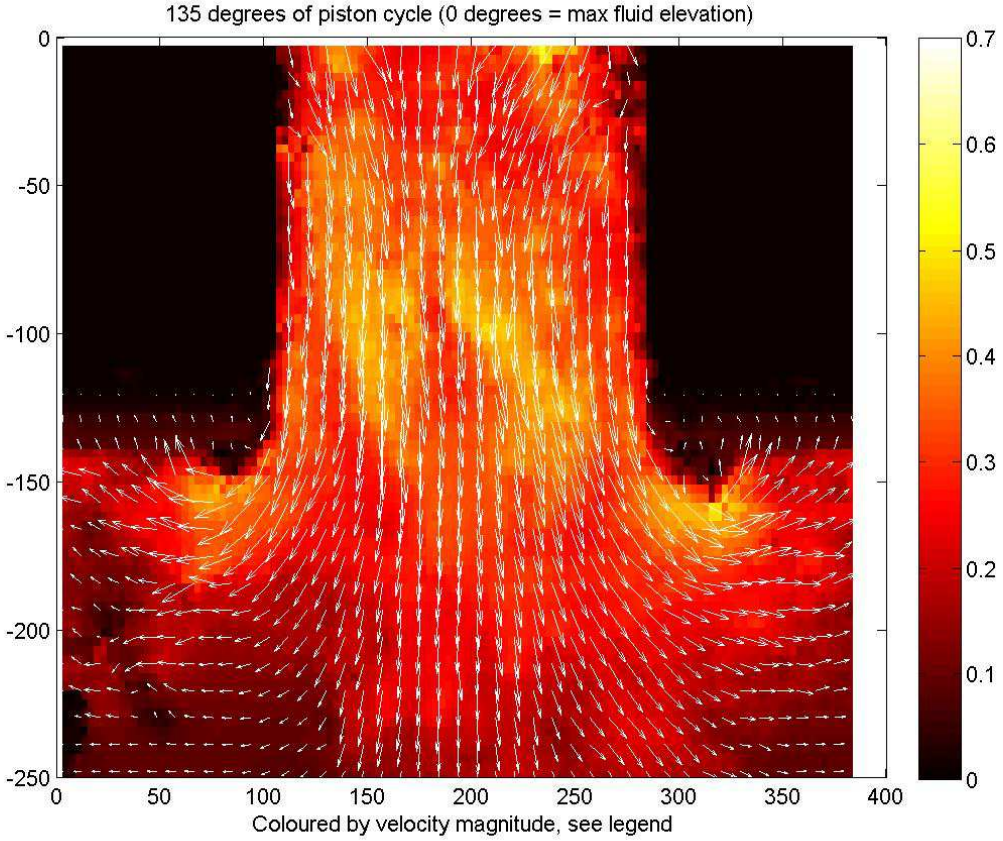
135 degrees of piston cycle (0 degrees = max fluid elevation)
0
-50
-100
-150
-200
-250
0
50
100
150
200
250
300
350
400
0.7
0.6
0.5
0.4
0.3
0.2
0.1
0
Coloured by velocity magnitude, see legend

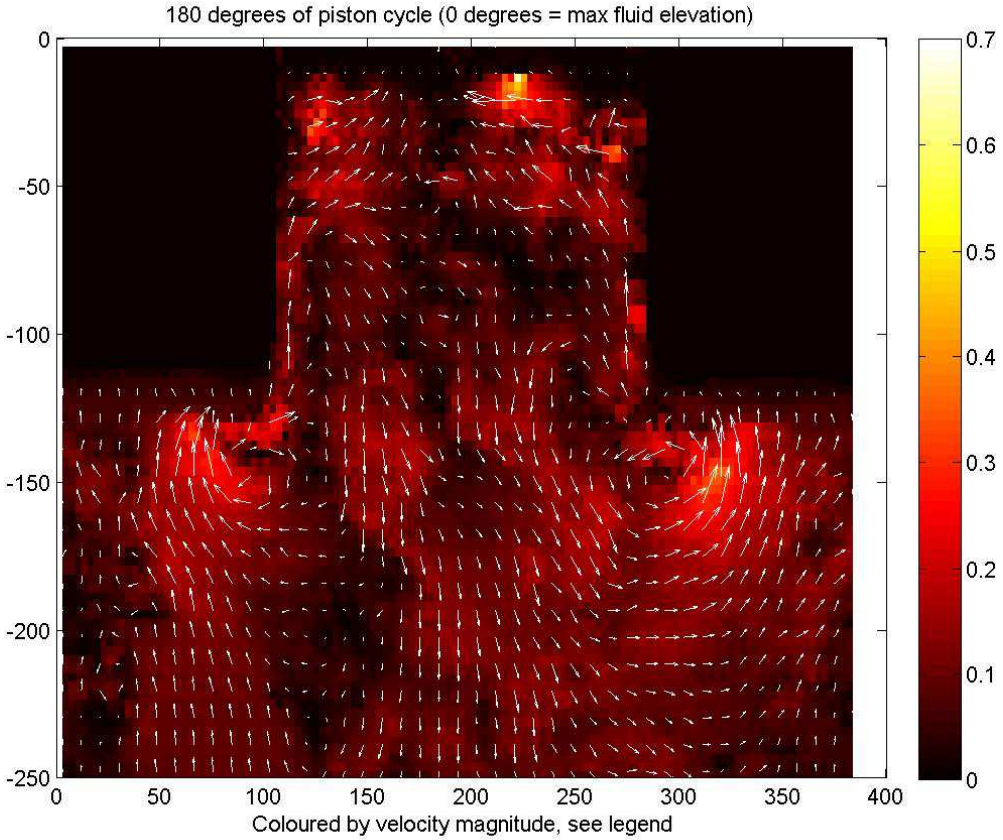
180 degrees of piston cycle (0 degrees = max fluid elevation)
0
-50
-100
-150
-200
-250
0
50
100
150
200
250
300
350
400
0.7
0.6
0.5
0.4
0.3
0.2
0.1
0
Coloured by velocity magnitude, see legend

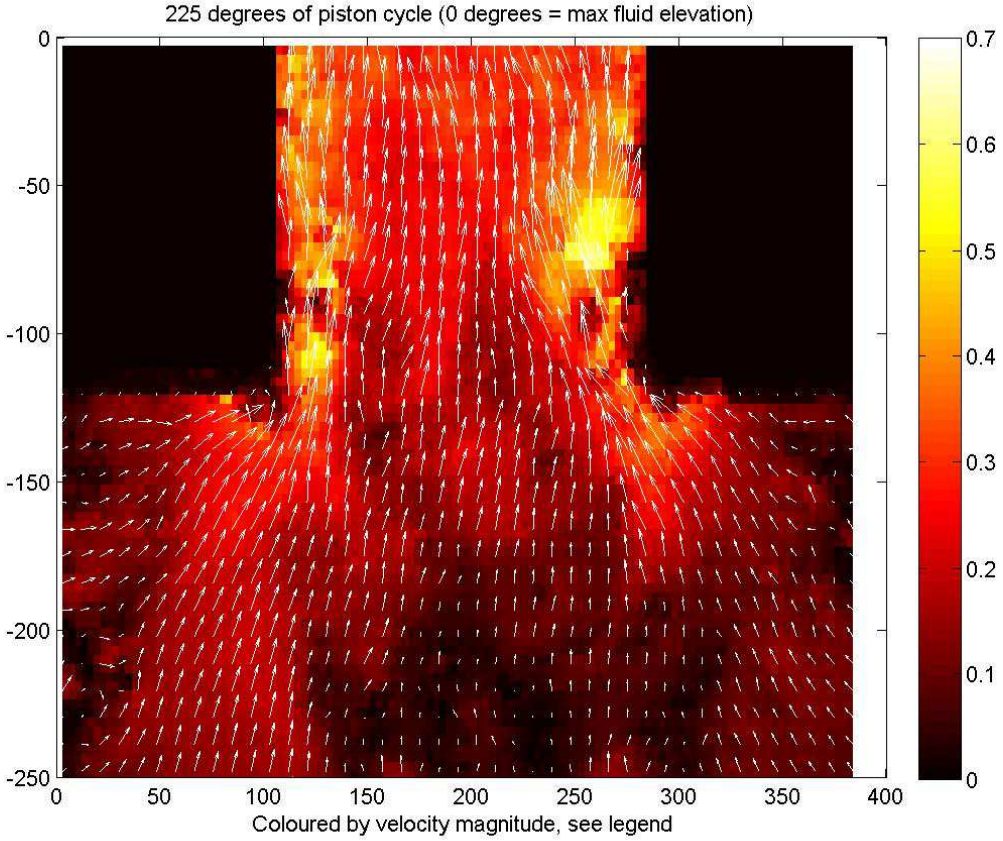
225 degrees of piston cycle (0 degrees = max fluid elevation)
0
-50
-100
-150
-200
-250
0
50
100
150
200
250
300
350
400
0.7
0.6
0.5
0.4
0.3
0.2
0.1
0
Coloured by velocity magnitude, see legend

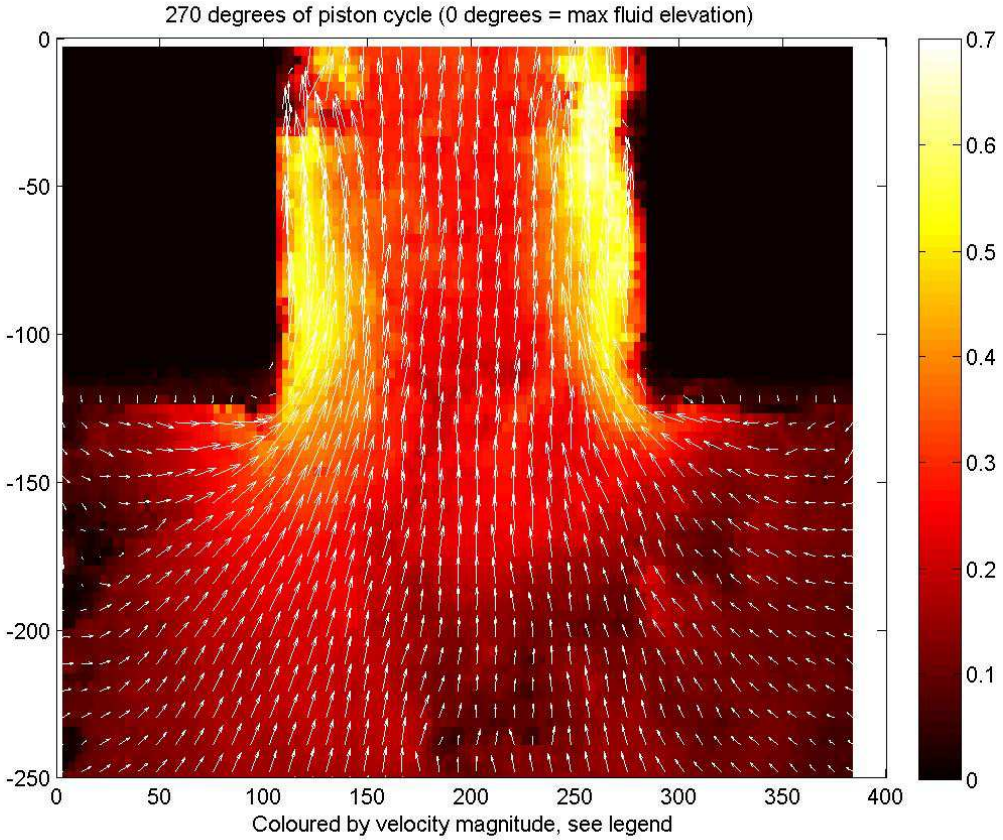
270 degrees of piston cycle (0 degrees = max fluid elevation)
0
-50
-100
-150
-200
-250
0
50
100
150
200
250
300
350
400
0.7
0.6
0.5
0.4
0.3
0.2
0.1
0
Coloured by velocity magnitude, see legend

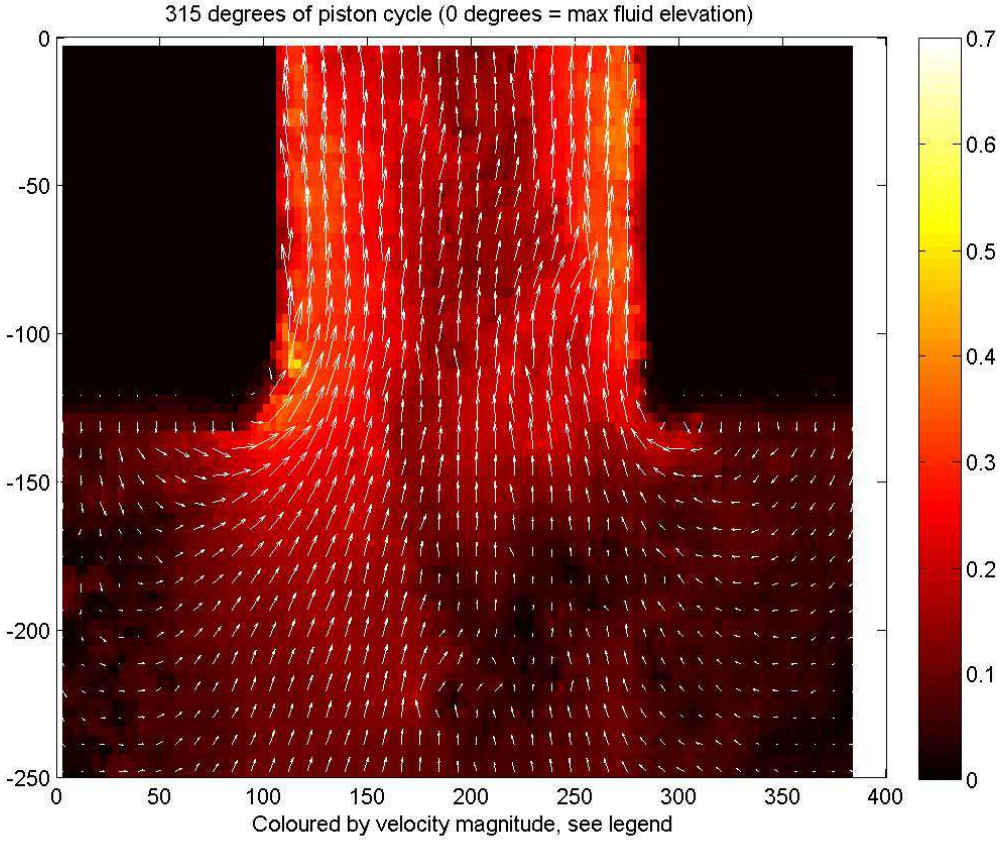
315 degrees of piston cycle (0 degrees = max fluid elevation)
0
-50
-100
-150
-200
-250
0
50
100
150
200
250
300
350
400
0.7
0.6
0.5
0.4
0.3
0.2
0.1
0
Coloured by velocity magnitude, see legend

Appendix B: *Seven Viking* information flyer

Seven Viking

7

Type:
IMR, Survey & Light Construction

Classification:
DnV 1A1 with the following class notations: SF, E0, DYNPOS-AUTR, CLEAN DESIGN, NAUT-AW, COMF-V(3), DEICE, ICE-C, HELDK-SH(CAA-N), WS, LFL*

The *Seven Viking* is a state-of-the-art vessel, with the innovative X-BOW® it is designed to meet the high demands of Inspection Maintenance and Repair (IMR), Survey and Light Construction in some of the harshest environments. The versatility of the vessel allows for Scale Treatment and Light Diving Support services.

- Length 106.5m x breadth moulded 24.5m
- Service Speed: 16.0 knots
- Accommodation: 90 persons
- AHC Offshore crane: 135 Te @13m
- 2 x Workclass ROVs
- 1 x Observation class ROV

Seven Viking

November 2012

General Information

Classification	DnV 1A1 with the following class notations: SF, E0, DYNPOS-AUTR, CLEAN DESIGN, NAUT-AW, COMF-V(3), DEICE, ICE-C, HELDK-SH(CAA-N), WS, LFL*
Built	Norway 2012
Flag State Authority	Norway

Dimensions

Length Overall	106.5m
Breadth moulded	24.5m
Draught (operational)	6.5m
Draught (max)	8.0m
Freeboard at operational draught	5.0m
Freeboard at max draught	3.5m

Main Data

Service Speed	16.0 knots
Accommodation	90 persons (64 single cabins, 13 semi-single cabins)
Personnel elevator	
Mid Ship Helideck for SuperPuma and Sikorsky S-92, Ø26.1m	

Power generation and propulsion

Generators	2 x 4,320 kW main diesel 2 x 1,824 kW main diesel 1 x 250 kW emergency generator
Propulsion	3 x 3 MW contra rotating azimuth
Thruster	1 x 1.4 MW retractable compass 1 x 1.4 MW combi retractable 1 x 1.7 MW tunnel SCR (NOx Catalyst) on exhaust

Tank Capacities (100%)

Fuel MDO	2,100m^3
Fresh water (potable)	1,300m^3
Fresh Water	200m^3
MEG / Brine	600m^3
Special Products, LFL	450m^3

Working Deck

Deck strength	10t/m^2
Deck area	approx 830m^2

Weld-free seafastening

Twist locks are integrated in part of the working deck for quicker mobilisation/demobilisation of standard containers.

Cranes

Main Crane

AHC Offshore crane	135t @13m
Maximum reach	30m
Wire length	2,000m
AHC whip line	10t @ 31m
Whip line wire length	1000m
Operational limit	5.0m Hs Man riding

Auxiliary Cranes

Telescopic crane for provision	1 x 15 Te
Telescopic cranes in MHS hangar	2 x 3 Te
Telescopic crane on pallet	1 x 3 Te
Telescopic crane in ROV hangar	1 x 1 Te

Module Handling System

MHS fully integrated in hangar with cursor system for controlled launch and recovery of modules to 2,000msw in conditions up to 5m Hs.

Capacity to handle modules up to 70 Te and 10m height Skidding system with storage capacity of up to 8 skidding pallets, including 4 indoor storage positions.

Winches: 1 x 70 Te, 1 x 20 Te, 3 x 5 Te.

Integrated AHC winch with dedicated HPU for 12 lines hydraulic downline.

ROV

All ROV systems in enclosed ROV hangar
2 x Workingclass ROVs (Schilling HD), rated to 3,000 msw, launched over side by A-frames. AHC Umbilical winch, 2,500m umbilical

1 x Observation ROV (SubAtlantic Mohican), rated to 2,000 msw, launched by A-frame. AHC Umbilical winch, 1,800m umbilical.

Operational limit 5.0m Hs for all systems

Scale Treatment

Scale treatment pumping spread and special product tanks integrated in vessel
Pumping capacity 30-2,800 l/min @ 0-345 bar
Pre heating to 90 deg
Mixing units for small volumes of additives.

Operation control

Joint operation control room for Shift Supervisor, MHS control, ROV control, Scale Treatment control, third party control and survey with direct view to MHS.

www.subsea7.com

subsea 7

Appendix C: Formal thesis description

NTNU
Norwegian University of Science and Technology
Department of Marine Technology

MASTER THESIS IN MARINE HYDRODYNAMICS

SPRING 2013

FOR

Stud.techn. Leiv Aspelund

EXPERIMENTAL STUDY OF THE HYDRODYNAMIC FORCES ACTING ON OBJECTS IN A MOONPOOL.
(Eksperimentell undersøkelse av hydrodynamiske krefter på objekter i en moonpool.)

The fluid motions in a moonpool have proven hard to predict. Additionally, very little research on the vertical hydrodynamic forces acting on objects in a moonpool has been done in the past. Simplified methods for calculating the forces exist, but the validity of the assumptions made for these methods are uncertain.

By doing experimental testing on a 2-dimensional model, the candidate will attempt to study the trends of the fluid motions in a moonpool; with and without objects. The hydrodynamic forces acting on objects in the moonpool will be studied and compared to the corresponding forces found using the aforementioned simplified methods. PIV (particle image velocimetry) will be used in order to visualize the flow fields in the moonpool, the point of which is to see the connections between the basic flow phenomena (such as the vortex shedding at the inlets of the moonpool) and the resulting moonpool wave elevation or the forces on the objects.

In the thesis the candidate shall present his personal contribution to the resolution of the problem within the scope of the thesis work. Theories and conclusions should be based on mathematical derivation and logic reasoning identifying the various steps in the deduction. The original contribution of the candidate and material taken from other sources shall be clearly defined. Work from other sources shall be properly referenced. The candidate should utilize the existing possibilities for obtaining relevant literature.
The thesis should be organized in a rational manner to give a clear exposition of results, assessments and conclusions. The text should be brief and to the point, with a clear language.

The thesis shall contain the following elements: A text defining the scope, preface, list of contents, summary, main body of thesis, conclusions with recommendations for further work, list of symbols and acronyms, references and appendices. All figures, tables and equations shall be numerated.
It is supposed that Department of Marine Technology, NTNU, can use the results freely in its research work by referring to the student's thesis.
The thesis shall be submitted June 10, 2013, in two copies.

Bjørnar Pettersen
Professor/supervisor